ATMOSPHERIC-IONOSPHERIC DISTURBANCES IN THE MLT REGION DURING CONVECTIVE CLIMATE: AN INTEGRATED APPROACH

Babu Ram Tiwari

Doctorate Thesis of the Graduate Course in Space Geophysics, supervised by Drs. Esfhan Alam Kherani, Eurico Rodrigues de Paula, and José Humberto Andrade Sobral, approved in November 05, 2015.

URL of the original document:
<http://urlib.net/8JMKD3MGP3W34P/3KK4Q3S>

INPE

São José dos Campos

2015

ATMOSPHERIC-IONOSPHERIC DISTURBANCES IN THE MLT REGION DURING CONVECTIVE CLIMATE: AN INTEGRATED APPROACH

Babu Ram Tiwari

Doctorate Thesis of the Graduate Course in Space Geophysics, supervised by Drs. Esfhan Alam Kherani, Eurico Rodrigues de Paula, and José Humberto Andrade Sobral, approved in November 05, 2015.

URL of the original document:
<http://urlib.net/8JMKD3MGP3W34P/3KK4Q3S>

INPE

São José dos Campos

2015

Aluno (a): **Babu Ram Tiwari**

Título: "ATMOSPHERIC-IONOSPHERIC DISTURBANCES IN THE MLT REGION DURING CONVECTIVE CLIMATE: AN INTEGRATED APPROACH"

Aprovado (a) pela Banca Examinadora em cumprimento ao requisito exigido para obtenção do Título de **Doutor(a)** em

Geofísica Espacial/Ciências do Ambiente Solar-Terrestre

Dra.   Maria Virgínia Alves

Presidente / INPE / SJCampos - SP

Dr.   Esfhan Alam Kherani

Orientador(a) / INPE / SJCampos - SP

Dr.   Eurico Rodrigues de Paula

Orientador(a) / INPE / SJCampos - SP

Dr.   José Humberto Andrade Sobral

Orientador(a) / INPE / SJCampos - SP
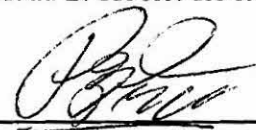
Dr.   Delano Gobbi

Membro da Banca / INPE / SJCampos - SP

Dr.   Daiki Koga

Membro da Banca / INPE / São José dos Campos - SP

Dr.   Nanan Balan

Convidado(a) / Univer. Of Sheffield / Reino Unido - UK

Dr.   Paulo Alexandre Bronzato Nogueira

Convidado(a) / IFSP../ Campos do Jordão - SP

Este trabalho foi aprovado por:

( ) maioria simples

(X) unanimidade

São José dos Campos, 05 de Novembro de 2015

This thesis is dedicated to the memory of my father, Tika Ram Tiwari

ACKNOWLEDGEMENTS

ABSTRACT

The Mesosphere-Lower-Thermosphere (MLT) region of the atmosphere in the 70-140 km altitude hosts varieties of atmospheric-ionospheric disturbances, owing to its coupling with the lower atmosphere through the acoustic-gravity waves (AGWs). These waves are launched during the tropospheric convection involving convective instability (CI) which is a key process during the convective climate in determining the meteorological and weather conditions. The objective of my thesis is to develop an integrated theoretical framework that includes cause and effects from troposphere to MLT region. This objective will be pursued by addressing three topics: (1) Troposphere convection dynamics, (2) Generation and propagation of AGWs arising from the convection, and (3) Subsequent atmospheric-ionospheric disturbances (AIDs) in the MLT region. In the first step, I propose to develop a new simulation model for the tropospheric convection that includes the diabatic and adiabatic dynamics desired during weak and strong environmental lapse rates. In the second step, the AGWs model developed by Kherani et al. (2012) will be integrated with the first step. In the third step, an ionospheric model will be developed and integrated with the first two steps. With this integrated model, I propose to study the following aspects: (i) CI associated lapse rate variation in the troposphere, (ii) simulation of OH airglow ripples and descending sodium (Na) density quasi-periodic (QP) disturbances in the MLT region, (iii) simulation of QP disturbances in the lower and upper E region, (iv) QP disturbances in the electrojet. All these aspects will be examined for the tropical/equator-low-latitude atmosphere-ionosphere and the simulation results will be compared with the observations from previous studies.

DISTÚRBIOS ATMOSFÉRICOS-IONOSFÉRICOS NA REGIÃO MLT DURANTE A OCORRÊNCIA DE FENÔMENOS CLIMÁTICOS CONVECTIVOS: UMA ABORDAGEM INTEGRADA

RESUMO

O intervalo do perfil vertical da atmosfera entre 70 e 140 km de altitude, que compreende a região da mesosfera e baixa termosfera (MLT, na sigla em Inglês), abriga uma variedade de distúrbios ionosféricos e atmosféricos provocados pelo acoplamento dessa região com a baixa atmosfera que se dà através de ondas de gravidade acústicas. Essas ondas são geradas em decorrência de convecções troposféricas associadas às instabilidades convectivas que são consideradas na determinação das condições meteorológicas e climáticas. O objetivo desta tese é desenvolver um arcabouço teórico integrado que inclui causa e efeitos da troposfera para a região MLT. Este objetivo será perseguido ao abordarmos três tópicos: (1) a dinâmica das convecções troposféricas, (2) geração e propagação de ondas de gravidades acústicas em decorrência da convecção, e (3) distúrbios atmosféricos-ionosféricos subsequentes (AIDs, na sigla em Inglês) presentes na região MLT. Como primeiro passo, propomos desenvolver um novo modelo de simulação para convecção troposférica que inclui as dinâmicas diabáticas e adiabáticas relativas às taxas de lapso ambiental fracas e fortes. A seguir, integramos o modelo de ondas de gravidade acústica desenvolvido por Kherani et al. (2012) é integrado ao primeiro passo. Posteriormente, adicionamos um modelo ionosférico aos dois primeiros. Com esse modelo acoplado, propomos estudar os seguintes aspectos: (i) associação entre instabilidades convectivas e taxas de lapso ambiental, (ii) simulação de ondulações na emissão de aeroluminescência da hidroxila e distúrbios quase-periódicos na densidade do sódio, (iii) simulação de distúrbios quase-periódicos na base e no topo da camada E, (iv) distúrbios quase-periódicos no eletrojato. Todos esses aspectos serão examinados para o sistema atmosfera-ionosfera das regiões tropical, equatorial e de baixas latitudes, de modo que os resultados das simulações serão comparados com observações reportadas na literatura.

LIST OF FIGURES

LIST OF TABLES

LIST OF ABBREVIATIONS

AGWs	–	Acoustic Gravity Waves
AID	–	Atmospheric-Ionospheric Disturbance
AIDs	–	Atmospheric-Ionospheric Disturbances
CEJ	–	Counter Electrojet
CI	–	Convective Instability
CII	–	Collisional Interchange Instability
EEJ	–	Equatorial Electrojet
FAI	–	Field Aligned Irregularity
FTCS	–	Forward-Time Central-Space
EUV	–	Extreme ultraviolet
GW	–	Gravity Wave
HTI	–	Height-time-intensity
HWM	–	Horizontal Wind Model
IGWs	–	Inertial Gravity Waves
L.H.S	–	Left Hand Side
LIDAR	–	Light Detection And Ranging
LT	–	Local Time
MLT	–	Mesosphere Lower Thermosphere
MSIS	–	Mass Spectrometer and Incoherent Scatter Radar
MSTIDs	–	Medium Scale Traveling Ionospheric Disturbances
NIR	–	Near Infrared
PDE	–	Partial Differential Equation
QP	–	Quasi-periodic
RADAR	–	RAdio Detection And Ranging
R.H.S	–	Right Hand Side
SNR	–	Signal-to-noise ratio
SOR	–	Successive Over-relaxation
SSTIDs	–	Small Scale Traveling Ionospheric Disturbances
TIDs	–	Traveling Ionospheric Disturbances
UT	–	Universal Time
UV	–	Ultraviolet
VHF	–	Very High Frequency

CONTENTS

1 INTRODUCTION

The Earth's atmosphere is a natural laboratory that allows the study of a huge number of physical, chemical and dynamical processes. Many interesting investigations have been carried out by several theoretical and observational studies related to various regions of the Earth's atmosphere for the last few decades. Extensive experimentations have been performed in the troposphere, the lowest part of the Earth's atmosphere. The stratosphere, immediate layer above the troposphere, has also drawn significant attention for studying most important species, e.g., ozone and also for chemical and dynamical processes. The development of the rocket and satellite technologies for the last few decades has facilitated upper atmospheric studies. The Mesosphere-Lower-Thermosphere (MLT) region lying between 70-140 km altitude and is the least explored region of the Earth's atmosphere. This region is very important for attaining notions of gravity wave, planetary wave and tidal phenomena in the atmosphere, which govern the atmospheric-ionospheric dynamics. These waves are mostly generated from the lower atmosphere and propagate to the upper atmosphere. During propagation, these waves carry energy and momentum and finally they deposit this energy in the MLT region (FRITTS; ALEXANDER, 2003). Thus the dynamical condition of the MLT region is strongly controlled and modified by these wave features. The mesopause region, which separates mesosphere and thermosphere, is very important for controlling the wave dynamics. The mesopause layer acts as a filter for allowing or not-allowing several kinds of waves which are created in the lower atmosphere and pass through mesopause to the thermosphere and ionosphere. Therefore, MLT region plays a vital role in middle and upper atmospheric coupling processes.

The atmosphere surrounding the Earth is the gaseous layer that is retained by the Earth's gravity. The atmospheric density decreases with increasing altitude from the Earth surface. The atmosphere exhibits vertical distribution of temperature, pressure, density, and composition. The pressure and density of the atmosphere decrease exponentially with increasing altitude. Based on the temperature distribution, there are four different regions of the atmosphere. They are troposphere, stratosphere, mesosphere, and thermosphere. The boundaries separating these atmospheric regions, called pauses. These correspond to major turning points in the temperature profile (BRASSEUR; SOLOMON, 2005). Figure 1.1 shows the classification of different regions of the Earth's atmosphere on the basis of temperature.

The temperature varies considerably from the ground up to about 100 km altitude,
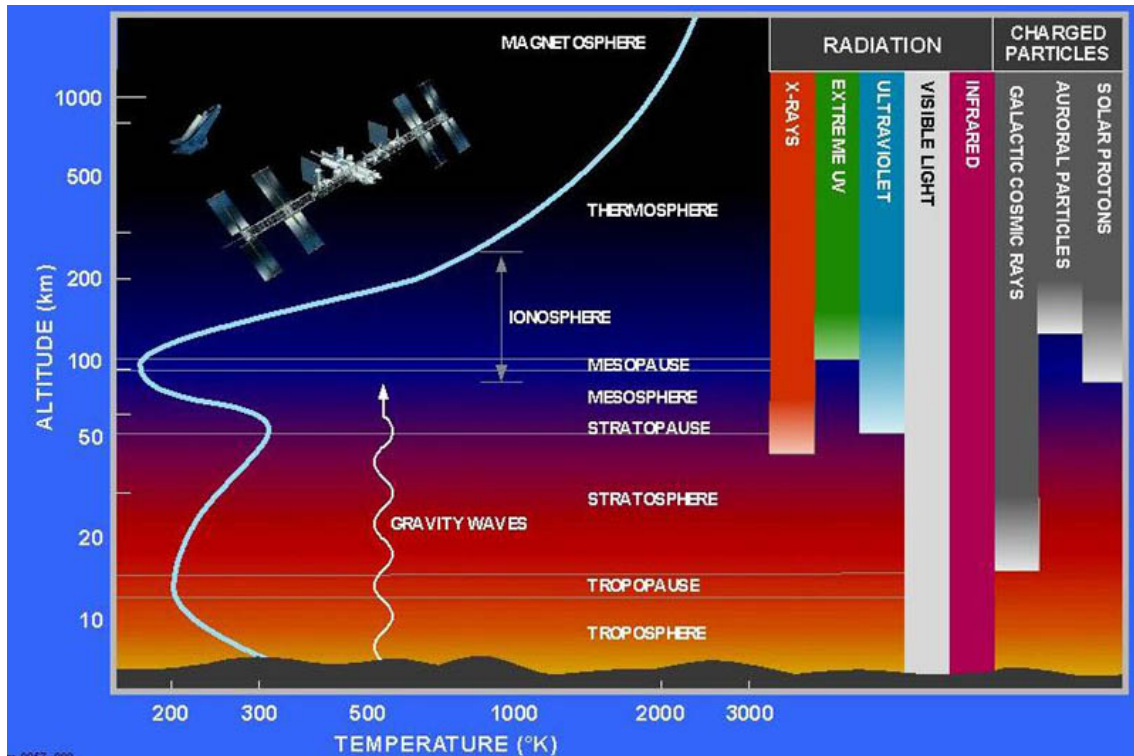
Figure 1.1 - Vertical temperature profile of the Earth's atmosphere describing different regions and the solar radiations being absorbed at different altitudes.
Source:http://www.theozonehole.com/atmosphere.htm

with a strong seasonal variation. The troposphere is the lowest part of the atmosphere and extends from surface to a height of $\sim 10 - 15$ km. The temperature generally decreases with the height in the troposphere. The decrease in temperature with height is termed as 'lapse rate'. For dry air, the lapse rate is called dry adiabatic lapse rate, $\Gamma = g/c_p$. Dry adiabatic lapse rate value is approximately 9.8 K/km. The lapse rate is considerably different for moist air due to the heat content of water vapor. The troposphere contains 99% of water vapor in the atmosphere which plays a significant contribution in regulating air temperature. The major heat source in the troposphere is the absorption of solar energy and the thermal radiation from the planet's surface. The atmosphere within this part naturally becomes unstable due to the negative lapse rate (i.e., $\gamma_e = \frac{1}{T}\frac{dT}{dy}$) (RISHBETH; GARRIOTT, 1969). The environmental lapse rate in the troposphere is 6-7 K/km. The tropopause is the boundary between the upper troposphere and the stratosphere which is a turning point in the temperature profile from negative to positive lapse rate. Tropospheric convection significantly modifies the structure and dynamics of the other atmospheric regions. The vertically propagating atmospheric wave amplitude increases as the background density decreases.

2

Stratosphere is the second lower layer of the Earth's atmosphere, and it extends up to 50 km from the tropopause. It holds the ozone that absorbs harmful ultraviolet (UV) radiation and prevents it from reaching the Earth's surface. In this region, the temperature rises with increasing altitude. This rise in temperature is caused by the absorption of UV radiation from the Sun by the ozone layer and water vapor. This region is so called stratosphere because of the positive lapse rate, the atmosphere is stably stratified. Various types of waves, for examples, atmospheric gravity waves and tides carry energy from the troposphere upward into the stratosphere and transport energy from this region up to the mesosphere. The waves and tides influence the flows of air and can cause regional heating in the stratosphere. The stratospheric layer is bounded at the top by the stratopause where the temperature stops increasing and reverts back to a negative lapse rate (MOHANAKUMAR, 2008).

The mesosphere is a layer that extends from 50 to ∼ 100 km and is characterized by decrease in temperature with increasing altitude. The atmospheric gravity waves, planetary waves and tides carry energy and transfer momentum from the troposphere and deposited into the mesosphere. The dynamical processes of waves and their upward transport of momentum influence the mesospheric temperature. A temperature inversion layer is formed in the mesosphere where the temperature lapse rate reverses its sign from positive to negative. Atmospheric gravity wave, tidal activity and chemical heating are responsible for mesospheric inversion layers (WHITEWAY; CARSWELL, 1995). The region of inversion layer of enhanced temperature can be caused through the breaking of gravity waves associated with the regions of convective or shear instabilities (MERIWETHER; GARDNER, 2000).

The region is considered to be the coldest of Earth atmosphere reaching a minimum of 180 K at 80 km altitude. The peculiar thermal effects of this region is that the summer mesopause is much cooler than its winter counterpart, though it is continuously bathed in sunlight. This is due to the existence of a high-altitude summer-to-winter meridional circulation, which flows from the summer to the winter polar region. Atmospheric gravity waves play the most important role in dynamical processes of the atmosphere.

Thermosphere is a region of high temperature and very low density. The thermosphere includes the ionosphere and extends out to several hundred kilometers. The temperature increase is due to the absorption of intense solar radiation by atomic oxygen and nitrogen, which is the major heating mechanism in the thermosphere. Extreme ultraviolet (EUV) and X-ray photons break electrons away from gas parti-

cles in the thermosphere, producing electrically-charged ions of atoms and molecules (mainly N_2^+, O_2^+ and O^+ in lower thermosphere). Winds and overall circulation in the thermosphere are driven largely by the atmospheric tides and gravity waves. The neutral thermosphere overlaps in altitude with the ionosphere which extends from ~ 85 km to ~ 1000 km (KELLEY, 1989; SCHUNK; NAGY, 2000). Beyond the thermosphere, the region is called exosphere, where interplanetary space starts.

1.1 Convective Instability (CI)

The convection in the troposphere of the terrestrial atmosphere is a natural phenomenon, that determines the meteorological conditions such as convective storms, thunderstorms, small and large-scale circulations etc. The convection arises owing to the convective instability (CI) in the presence of destabilizing temperature environmental temperature gradient or lapse rate that competes with the stabilizing adiabatic temperature gradient (SPIEGEL; VERONIS, 1960; OGURA; PHILLIPS, 1962; NORMAND et al., 1977; MARKOWSKI, 2007). Under such temperature profile, the cooler (or more dense) fluid parcel is supported by the heated (or less dense) fluid parcel against the gravity, leading to an unstable equilibrium or CI.

Theoretical works concerning the tropospheric CI are in abundance and most of them are based on the Oberbeck-Boussinesq (OB) approach. The four most important assumptions under OB approach are the following ones (NORMAND et al., 1977; MAHRT, 1986):
(1) The shallow atmosphere condition for the ambient hydrostatic atmosphere which means that the density scale height is approximately equal to the pressure scale height,
(2) Isothermal incompressible flow (i.e., time restrictions on the perturbation such that the buoyancy velocity remains slower than the acoustic velocity),
(3) Adiabatic compressible flow (i.e., rapid compression and expansion),
(4) A linearization of $\frac{1}{\rho}$ where ρ is the total density, consists of hydrostatic equilibrium density and the linearly (with temperature) expanding density.
These assumptions simplify the instability treatment and a linear Brunt-Vaisala frequency (or growth rate) expression for the Oberbeck-Boussinesq-Convective-Instability (OBCI) is obtained in the following form (NORMAND et al., 1977):

$$\omega_{bB} = \sqrt{g(\gamma_{ad} + \gamma_e)}$$

where $\gamma_{ad} = \frac{g}{c_p T}$ and $\gamma_e = \frac{1}{T}\frac{dT}{dy}$ are the adiabatic lapse rate [1] and environmental lapse

_____

[1] The adiabatic lapse rate is the rate of temperature decrease with altitude for a parcel of air

rate [2], respectively. T is the ambient temperature, g is the gravitational acceleration, c_p is specific heat at constant pressure, and y is the altitude. The CI is excited when $\omega_{bB}^2 < 0$ i.e., when $\gamma_{ad} < |\gamma_e|$.

1.2 Acoustic Gravity Waves (AGWs)

Under the action of buoyancy and pressure forces, the atmosphere sustains the normal modes known as the Acoustic-Gravity waves (AGWs). These modes are due to the equilibrium of buoyancy-compressional force against the restoring inertial force. Without the buoyancy force, these waves become the high-frequency acoustic waves. On the other hand, without compression, these waves become low-frequency gravity waves (LANDAU; LIFCHITZ, 1987). The AGWs are in abundance in the atmosphere owing to the wide range of natural sources that may excite them abundantly and the wide spectral range they occupy in the atmosphere (YEH; LIU, 1974; FRITTS; ALEXANDER, 2003). They also propagate in a wide height range from the troposphere to the thermosphere and from high-latitude to equatorial and low latitudes (HINES, 1960; RICHMOND, 1978).

The major sources of AGWs are: the motion of the ground during an earthquake, man-made explosions, weather or climate dynamics, and ionospheric disturbances at high latitude.

Table 1.1 shows a classification based on period and wavelength. The small scale waves come from the troposphere; the medium-scale waves may be from troposphere or ionosphere; and the large-scale events from the high-latitude ionosphere.

Table 1.1 - A Classification Scheme for AGWs

Nomenclature	Horizontal trace velocity ($\mathrm{m}s^{-1}$)	Period (min)	Wavelength
Large-scale	$\sim$250-1000	> 70	> 1000 km
Medium-scale	90 to $\sim$250	$\sim$ 15-70	Several hundred kilometers
Small-scale	> 300	$\sim$ 2-5	-

Source: Adapted from Hunsucker and Hargreaves (2003)

Kherani et al. (2012) have derived the wave equation of the AGWs using the Navier-Stokes equations namely the momentum, continuity and energy equations in the

---

rising under adiabatic condition.

[2] The environmental lapse rate is the actual rate at which the ambient atmospheric temperature decreases with height.

atmosphere.

$$\frac{\partial \vec{W}}{\partial t} + \vec{W} \cdot \nabla \vec{W} = -\frac{1}{\rho} \nabla p + \vec{g} + \frac{1}{\rho} \left(\mu \nabla^2 \vec{W} + \left(\xi + \frac{\mu}{3} \right) \nabla \left(\nabla \cdot \vec{W} \right) \right);$$ (1.1)

$$\frac{\partial \rho}{\partial t} + \nabla \cdot \left(\rho \vec{W} \right) = 0;$$ (1.2)

$$\frac{\partial p}{\partial t} + \left(\vec{W} \cdot \nabla \right) p + \gamma p \nabla \cdot \vec{W} = 0,$$ (1.3)

where $\vec{W}$ is the perturbation wind, $p = \frac{R\rho T}{M_m}$ is the pressure, (ρ, T) are the atmospheric mass density and temperature, while μ and ξ are the dynamic first and second viscosities and R and M_m are the perfect gas constant and molar mass, respectively. Taking time derivative of momentum equation for the wind $\vec{W}$, and again substituting time derivatives of the density (ρ), wind $(\vec{W})$ and pressure (p) from the Navier-Stokes equations, the wave equation for the wind $\vec{W}$ of AGWs is obtained in the following form:

$$\frac{\partial^2 \vec{W}}{\partial t^2} = \frac{1}{\rho} \nabla \left(\gamma p \nabla \cdot \vec{W} \right) - \frac{\nabla p}{\rho^2} \nabla \cdot \left(\rho \vec{W} \right) + \frac{1}{\rho} \nabla \left(\vec{W} \cdot \nabla \right) p$$
$$+ \frac{\partial}{\partial t} \left(\nu \nabla^2 \vec{W} + \left(\xi' + \frac{\nu}{3} \right) \nabla \left(\nabla \cdot \vec{W} \right) \right) - \frac{\partial}{\partial t} \left(\vec{W} \cdot \nabla \vec{W} \right)$$ (1.4)

Here, $\nu = \mu/\rho$ and $\xi' = \xi/\rho$ are the first and second kinematic viscosities. Kherani et al. (2012) have also derived the dispersion relation of AGWs using the first four terms in the wave Equation 1.4, that is, for the non-dissipative AGWs:

$$\frac{\partial^2 \vec{W}}{\partial t^2} = \frac{\gamma p}{\rho} \nabla \left(\nabla \cdot \vec{W} \right) + (\gamma - 1) \frac{\nabla p}{\rho} \nabla \cdot \vec{W} - \frac{\nabla p}{\rho} \left(\vec{W} \cdot \nabla \right) \log \rho + \frac{1}{\rho} \nabla \left(\vec{W} \cdot \nabla \right) p$$ (1.5)

Assuming a form of plane wave solution i.e., $(W_x, W_z) = (W_x^o, W_y^o) exp(ik_x x + ik_y y - i\omega t) + y/2H$, the dispersion relation for the AGWs is given by the following relation:

$$\omega^4 - \omega^2 c_s^2 \left(k^2 + \frac{1}{4H^2} \right) + (\gamma - 1) g^2 k_x^2 = 0$$ (1.6)

where

- ω is the angular frequency of the wave,
- k_x is the horizontal wave number $(=2\pi/\lambda_x)$,
- k_y is the vertical wave number,

- γ is the ratio of specific heats (constant pressure/constant volume),

- c_s is the speed of sound $(=\gamma p/\rho)$,

- H is the vertical scale height of the atmosphere $(=RT/g)$, and

- g is the acceleration due to gravity.

This equation states the relation between the frequency and the wavelength (or wave number) in the vertical and the horizontal directions for an AGWs (HUNSUCKER; HARGREAVES, 2003). Two significant frequencies are the acoustic cut-off frequency and the buoyancy or Brunt-Vaisala frequency, defined as follows:

$$\omega_a = \gamma g/(2c_s), \omega_b = (\gamma - 1)^{1/2} g/c_s \tag{1.7}$$

With these definitions, the dispersion relation may be written as follows:

$$k_y^2 = \left(1 - \frac{\omega_a^2}{\omega^2}\right) \frac{\omega^2}{c_s^2} - k_x^2 \left(1 - \frac{\omega_b^2}{\omega^2}\right)$$

It is evident that to have $k_y^2 > 0$ i.e. for the vertical propagation, wave should have frequency $\omega < \omega_b$ or $\omega > \omega_a$. In these frequencies regime, the AGWs become pure gravity and acoustic waves respectively. The dispersion relation for the pure gravity wave can be obtained under limit $\omega < \omega_b < k_x c_s$ as follows:

$$k_y^2 = -k_x^2 \left(1 - \frac{\omega_b^2}{\omega^2}\right)$$

The phase and group velocities are, respectively, given by following expressions:

$$\frac{\omega}{k} = \frac{k_x}{k^2}\omega_b \quad ; \quad \frac{\partial \omega}{\partial k} = -\frac{k_x}{k^2}\omega_b; \quad k^2 = k_x^2 + k_y^2$$

which states that the group propagation is opposite to the phase propagation.

In a gravity wave, the energy flows at right angles to the direction of phase propagation. Figure 1.2 illustrates the relations amongst particle displacement, phase propagation, and group propagation in a gravity wave. It is noted that if the source is below, the energy flows upward but the phase propagation is downward. Moreover, the amplitude of the air displacement increases with altitude so that the energy flux may be constant.
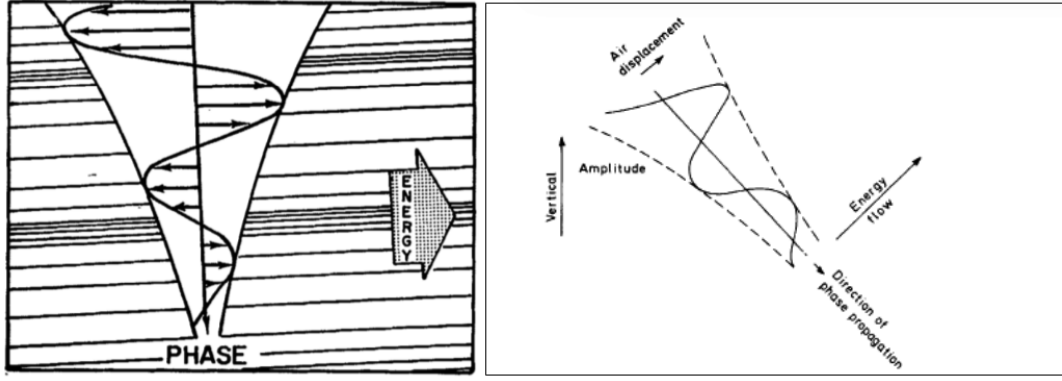
Figure 1.2 - The downward propagation of phase and upward propagation of energy of AGWs.

Source: Adapted from Hines (1960) and Hargreaves (1992)

Due to the combination of the longitudinal displacement of an acoustic wave with the transverse displacement of a gravity wave, in general the particle motion is elliptical in AGWs. There are alternative compressions and rarefactions at successive zero-displacement points in Figure 1.2. At extremely low frequency, the air motion and the group velocity would be horizontal, the phase propagation vertical, and the compression and rarefaction zero.

1.2.1 Ducting and Instability of AGWs

Hines (1960) has proposed a theory for the AGWs propagation from troposphere up to MLT region, as well as the neutral atmosphere-ionosphere coupling. Theoretical studies have shown that the vertical propagation of the AGWs may happen from thermal and density ducts in the stratosphere, mesosphere and thermosphere (HICKEY et al., 1998; PIANI et al., 2000; ZHANG; YI, 2002; YU; HICKEY, 2007; KHERANI et al., 2011).

In this Section, we intend to give details of the ducting theory as well as the instability of AGWs as follows:

The vertical component of Equation 1.5 can be written as follows:

$$\frac{d^2 \vec{W}_y}{dt^2} = \frac{\gamma p}{\rho} \frac{\partial}{\partial y}(\nabla \cdot \vec{W}) + (\gamma - 1)\zeta \nabla \cdot \vec{W} + \zeta \frac{\partial \vec{W}_y}{\partial y} - \omega_b^2 \vec{W}_y$$

where

$$\omega_b^2 = \zeta \frac{d \log \rho}{dy} - \frac{1}{\rho}\frac{d^2 p}{dy^2}; \zeta = \frac{1}{\rho}\frac{dp}{dy}$$

8

Here ω_b expression is written in a general form which reduces to the form given in Equation 1.7 if $\zeta = -g$. The ducting and instability occur when $\omega_b^2 < 0$, i.e., instead of oscillating in time, wave amplitude grows with time. It is the last term in the ω_b^2, which may contribute negatively to ω_b^2. This term may be written as follows:

$$-\frac{1}{\rho}\frac{d}{dy}\left[p\left(\frac{1}{h_\rho}+\frac{1}{h_t}\right)\right] = -\frac{1}{\rho}\left(\frac{1}{h_\rho}+\frac{1}{h_t}\right)\frac{dp}{dy} - \frac{p}{\rho}\frac{d}{dy}\left(\frac{1}{h_\rho}+\frac{1}{h_t}\right)$$

where (h_ρ, h_t) are the density and temperature scale heights in the atmosphere. The first term of above expression leads to the instability such as convective instability in the altitude region where (h_t) is negative. On the other hand, the second term leads to the ducting in the altitude region where

$$\frac{d}{dy}\left(\frac{1}{h_\rho}+\frac{1}{h_t}\right) > 0$$

In the MLT region around mesopause, where temperature scale height changes from negative to positive, $\frac{d}{dy}\left(\frac{1}{h_t}\right) > 0$, thus leading to the ducting. This ducting is called the thermal ducting. In the altitude region near turbopause [3] (110 km) where transition from homosphere to heterosphere takes place, the density scale height changes from less negative to more negative i.e., $\frac{d}{dy}\left(\frac{1}{h_\rho}\right) > 0$, thus leading to the ducting. This ducting is called the density ducting.

1.3 Atmospheric Disturbances (Airglow emissions)

The Earth's upper atmosphere is a very low dense medium whose constituents are basically atomic oxygen, nitrogen along with hydrogen and helium gases. There are also less dominant constituents, e.g., Nitric Oxide (NO), Carbon dioxide (CO_2), Carbon monoxide (CO), Nitrous oxide (N_2O), Water vapor (H_2O), Ozone (O_3) etc. and metastable atoms and molecules are important for photochemistry, energetics and emissions of the upper atmosphere. The incident UV solar radiation on the atmospheric gases present there, causes them to be ionized and excited. When the excited molecules de-excite, radiations come out from them, which is known as Airglow. Airglow persists in both day and night. It is a very weak emission by chemical interactions of air molecules and atoms. It is known that there are several airglow emission layers in the upper mesosphere and lower thermosphere (MLT) region (CHAMBERLAIN, 1961). Airglow is a useful tool to probe the upper atmospheric dynamics. It is due to emissions from excited states formed by various processes in

---

[3]The transition zone, located at a height of around 110 km between the homosphere and heterosphere, is called turbopause.

the upper atmosphere, such as the recombination of ions, which are photoionized by the Sun during the day, luminescence caused by cosmic rays striking the upper atmosphere, and chemiluminescence caused mainly by oxygen and nitrogen reacting with hydroxyl ions. Some air molecules and atoms become excited by ultraviolet sunlight during the day, and de-excited to a lower-energy state at night, emitting light, first noticed by Angstrom (1868). The variability of airglow emissions having different wavelengths widely used to infer the mesosphere, lower thermosphere, ionosphere behavior (FAGUNDES et al., 1995; TAKAHASHI et al., 1998; MUKHERJEE, 2003; REISIN; SCHEER, 2004; TAORI et al., 2005). Airglow imaging of the upper mesosphere and lower thermosphere (MLT) utilizes the strong natural airglow emissions which originate at near 85-90 km for the OH Meinel bands, near 91-95 km for the O_2 atmospheric bands, near 90 km for Na airglow, and near 95-100 km for the OI (557.7 nm) green line. Molecules giving rise to airglow emissions include sodium, atomic and molecular oxygen and nitrogen (HECHT, 2004). The airglow emission line and emission band spectrum originate from energy level transitions in excited atoms and molecules at various heights in the Earth's atmosphere (SOBRAL et al., 1981). There are two extremely important geophysical parameters that can be obtained from airglow emissions. They are intensity and rotational-vibrational temperature. The intensity of individual band can give information about the chemical reaction processes associated with the emission as well as dynamical condition of the emitting region. Its obtained values and space-time variations provide the information regarding energy removal and various processes for the production of excited molecules. On the other hand, rotational and vibrational temperatures give information about the state of the medium, rates of deactivation and establishment of equilibrium. It gives the information to find the probability of transition that eventually determines all observed parameters from the emissions. The temperature is a very important parameter, which can give the information of the wave dynamical activities in the atmosphere (TAKAHASHI et al., 2009). Observations of the intensity variations of the OH, O_2 and OI (557.7 nm) airglow emissions provide information of wave parameters of passing gravity waves since the density and temperature vary with the wave's intrinsic properties.

In the MLT region, various different lines and band emissions occur at visible and near infrared (NIR) wavelengths. The visible and near infrared spectrum of the Earth's nightglow emission showing the dominant atomic and molecular emission lines and bands are shown in Figure 1.3. The airglow brightness is usually measured in 'Rayleigh' units represented by the letter 'R'. One Rayleigh is equal to $10^6 photons/cm^2/s^1$.
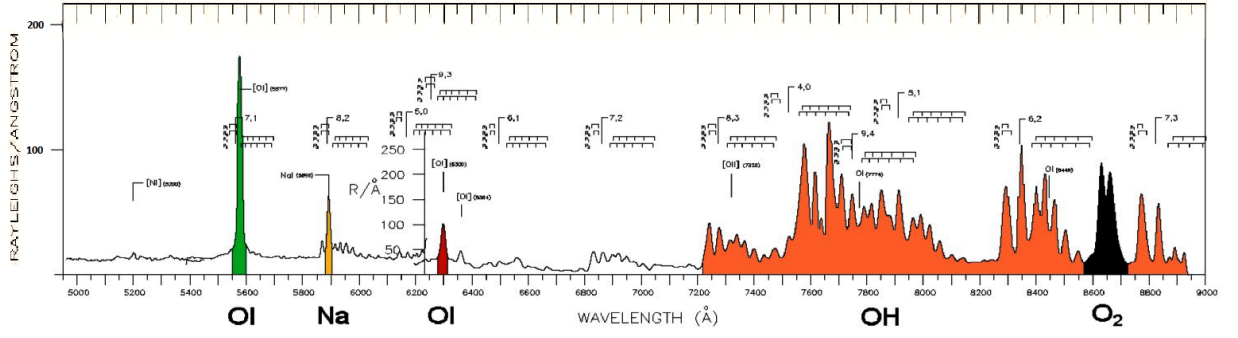
Figure 1.3 - Visible and NIR spectrum of the Earth's nightglow emission showing lines and bands.

Source: Adapted from Broadfoot and Kendall (1968), Shimkhada (2010)

Numerous sounding rocket experiments have determined the OH emission layer, Na (589.2 nm) emission layer, O_2 emission layer, and OI (green line) emission layer at the mesopause heights. Following we discuss the most important airglow emissions in the MLT region:

1.3.1 OH emission

The hydroxyl (OH) Meinel band airglow arises from the vibrationally excited OH molecules, which emits photons as they lose energy and return to lower vibrational states. It is the most dominant emission in the atmosphere. The intensity of the OH emissions at 840-846 nm layer peaks near ~ 87 km altitude. It is the height dependent which varies from 84 to 90 km altitude. For OH, transitions among various vibrational energy levels have been observed maximum up to 9th level. The spectra are determined due to rotational-vibrational transitions of the OH(ν) molecule in its ground state (MEINEL, 1950). The mechanism regarding the OH excitation was first proposed by Bates and Nicolet (1950), and further modified by Bates and Moiseiwitsch (1956). The chemical reactions involving the emission of OH airglow are given below:

$$O + O_2 + M \rightarrow O_3 + M, \qquad (1.8)$$

$$H + O_3 \rightarrow OH^* + O_2, \qquad (1.9)$$

$$OH^* \rightarrow OH + h\nu(3.34eV) \qquad (1.10)$$
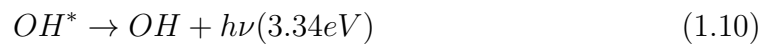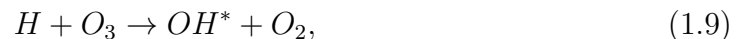
where M is a third body of major gas molecules either an N_2 or O_2. This is an

exothermic reaction and the energy released by reaction (3.34 eV) is sufficient to excite the OH molecule to the ninth vibrational level. Krassovsky (1971) proposed an alternative mechanism related to vibrationally excited O_2.

$$H + O_2^* \rightarrow OH^* + O \tag{1.11}$$

According to Bates and Moiseiwitsch (1956) this reaction is unlikely as it will give energy level higher than 9, which is not observed in the reality. There have been several measurements of wave structures imaged in the visible and NIR nightglow emissions from ground-based optical instruments.

1.3.2 Green line OI emission

The brighest airglow line emission in the visible spectrum is the OI green line at 557.7 nm, from excited oxygen atoms in a layer peak at 96 km altitude. The green line emission was first identified by McLennan and Shrum (1925) due to the forbidden electronic transition $(^1S_0 \rightarrow \, ^1D_2)$ of oxygen atoms. The oxygen molecule has only one electronic state from which normal transition can take place. Chapman (1931) proposed the three body atomic oxygen mechanism to explain the origin of this nightglow emission:

$$O + O + O \rightarrow O_2{}^* + O^* \tag{1.12}$$

The mechanism to explain the green line emission is the result from recombination of atomic oxygen (BARTH, 1964);

$$O + O + M \rightarrow O_2{}^* + M, \tag{1.13}$$

$$O_2{}^* + O \rightarrow O_2 + O(^1S), \tag{1.14}$$

$$O(^1S) \rightarrow O(^1D) + h\nu(557.7nm), \tag{1.15}$$
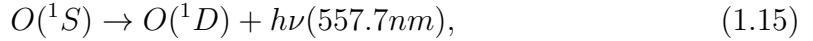
In the above reactions M is a third body of major gas molecules either an N_2 or O_2. OI and OH airglows are extensively studied using airglow photometer and imagers (SOBRAL et al., 1981; TAKAHASHI et al., 2009).

1.3.3 NaD line emission

The Na airglow emission from the neutral Na atoms in the terrestrial mesosphere has been known for many years, and Chapman (1939) first proposed that the mesospheric ozone plays a very important role for this emission (SARKHEL et al., 2010). The sodium doublet line airglow emission, is a yellow light from sodium atoms in a

layer at 92 km altitude. The yellow sodium emission is prominent at twilight, and due to photochemical processes in the night sky. The NaD radiation arises from the atomic transition Na ($3^2P_{3/2,1/2}$ - $3^2S_{1/2}$), which consists of two closely spaced lines, D_1 and D_2, at 589.0 and 589.6 nm, respectively. The following chemical scheme was proposed by Chapman (1939) to explain the origin of the Na airglow:

$$Na + O_3 \rightarrow NaO + O_2, \tag{1.16}$$

$$NaO + O \rightarrow Na^*(^2P, {}^2S) + O_2, \tag{1.17}$$

$$Na^*(^2P) \rightarrow Na(^2S) + h\nu(589.0, 589.6nm). \tag{1.18}$$
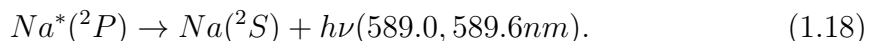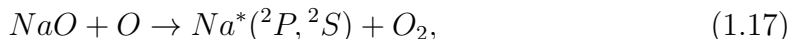
Thus, when NaO reacts with O to form Na which is in excited state ^2P, it emits energy to the ground state ^2S producing Na doublet emission. The excited Na can also be excited by the Na lidar (CLEMESHA, 1995) which is an efficient tool to study the temperature and AGWs activities in the MLT region.

1.3.4 O_2 emission

The molecular oxygen is also a very significant contributor to the atmospheric airglow emission. There are weak emissions from excited O_2. The peak of the maximum emission of the O_2 at 866-868 nm is $\sim$ 94 km. It is also the height dependent which varies from 92 to 97 km. The mechanisms regarding the O_2 emission (BARTH, 1964) are given below:

$$O + O + M \rightarrow O_2{}^* + M, \tag{1.19}$$

$$O_2{}^* + O \rightarrow O_2{}^1\Sigma + O, \tag{1.20}$$

$$O_2{}^1\Sigma \rightarrow O_2{}^3\Sigma + h\nu \tag{1.21}$$

The examples of four most important airglow images of short-period gravity waves observed in OH, Na, O_2 and OI emissions on June 5, 2002 from Bear Lake Observatory are shown in Figure 1.4. The intense night emission in the NIR OH emission, which is highly studied emission from the ground level.
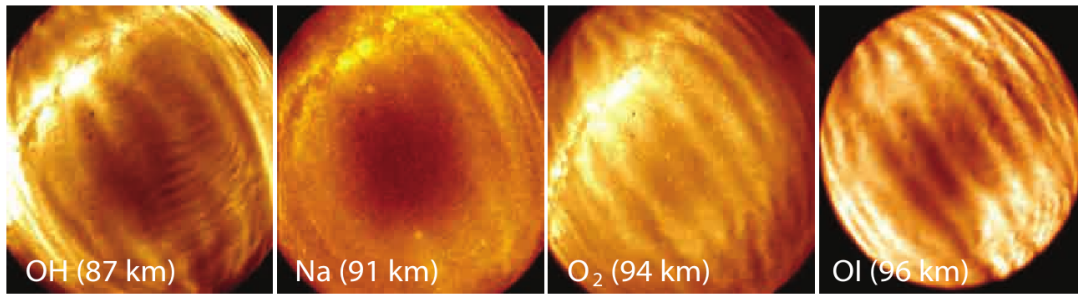
Figure 1.4 - The four most important airglow images showing short-period gravity wave structures recorded in OH, Na, O_2 and OI emissions on June 5, 2002 from Bear Lake Observatory.

Source: Adapted from Shimkhada (2010)

1.4 Ionosphere

The solar photons in the extreme ultraviolet (EUV) (17-170 nm) - X-ray (0.1-17nm) frequency range has sufficient energy to ionize the atmospheric constituents such as O_2, N_2, O. This ionized part of the atmosphere is called the ionosphere which is the partially ionized region of the upper atmosphere extending from ~ 60 km beyond 1000 km. This region contains significant numbers of free electrons and ions that affects the propagation of radio waves. It plays an important role in the communication and navigation having utility in virtually all aspects of modern society. The existence of the ionosphere was first established experimentally in 1924 using the method of radio wave reflection (APPLETON; BARNETT, 1925a; APPLETON; BARNETT, 1925b; BREIT; TUVE, 1925). The ionosphere can carry electrical currents as well as reflect, deflect and scatter radio waves.

The vertical structure of the ionosphere has been divided into four distinct layers depending on the ion constituent and associated chemistry. The solar spectrum deposits its energy at various heights depending on the absorption characteristics of the atmosphere, physics of recombination depends on the atmospheric density, and the composition of the atmosphere changes with height and these are the basic reasons for the formation of these distinct regions. Based on the substructure of the ionosphere it is usually divided into a number of characteristic layers (BRASSEUR; SOLOMON, 2005). They are basically the D, E, F_1 and F_2 layers. The ion density in each of these layers has a peak value at a certain altitude, above and below of which it decreases.

The lowermost region of the ionosphere extending up to about 90 km altitude is

known as the D-region. It is controlled by ionization of neutrals, mainly NO by solar X-rays radiations with wavelengths greater than 102.7 nm that include the Lyman alpha (121.5 nm) radiation. It is present during daytime hours, but disappears at night. In this region, the plasma density range is 10^2 -10^4 cm^{-3}.

The altitude range 90-150 km is called the E-region. In this region, the electron density is $\sim 10^5$ cm^{-3}. This region contains molecular ions such as N_2^+, O_2^+, NO^+ as primary constituents. The E-region is also characterized by the presence of metallic ions such as Mg^+, Fe^+, Ca^+ and Si^+, credited to the disintegration of meteoric bodies in the terrestrial atmosphere.

The F-region has the highest density amongst the three and it contains mostly O^+. During daytime, the F-region generally splits into two distinct regions namely F_1- and F_2-region. This is due to the presence of solar ultraviolet radiation ionizes the atomic oxygen present at F region during daytime.

The ionization layer above 150 km altitude is termed as the $F1$-region and is formed owing to the ionization of O by the radiations between 20-90 nm. The F_1-region has a peak density around 200 km and electron density range of $\sim 10^5 - 10^6 cm^{-3}$. In the E and F_1 regions, the recombination and ion-atom exchange reactions are the principal chemical reactions:

$$O_2^+ + e \rightarrow 2O(E - region) \quad ; \quad k_1 = \alpha_r[e] \quad s^{-1}$$
$$O^+ + N_2 \rightarrow NO^+ + N(F_1 - region) \quad ; \quad k_2 = \alpha_e[N_2] \quad s^{-1}$$
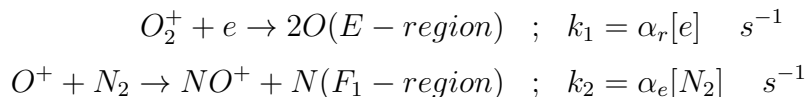
where k_1, k_2 are the reaction rates and α_r, α_e are the recombination coefficients, respectively. The square brackets represent concentration of the indicated species. If the ionization rate per unit volume is q then the chemical equilibrium at the F_1-peak is represented by following equation

$$q = \alpha_e[N_2][e]$$

Since $q \propto [O]$, it is evident that the electron density above F_1 peak is given by following relation:
$$[e] \propto \frac{[O]}{[N_2]}$$

which states that the electron density increases with altitude above F_1 peak inspite that the maximum ionization rate is at or below the F_1 peak. The density continues to increase with altitude till the diffusion (above 300 km altitude) restricts the fur-

ther increase and then the density begins to decrease. This leads to the formation of another layer above F_1 peak, called F_2 layer that extends from an altitude of $\sim$ 200 km to 1000 km and the electron density maximum varies around 300 km up to 10^6 cm^{-3}. However, the rates of production, recombination and diffusion varies with altitude, which may result in distinct F_1- and F_2-layer. During nighttime, F_1 layer disappears due to the absence of solar radiation, the E and F_1 layers disappear rapidly due to low production rate of ions and high recombination rate of molecular ions. The F_2 layer is maintained by dominant transport dynamics and low recombination rate of atomic ions at those altitudes. Similarly E region density is reduced considerably by the recombination though it is maintained by meteoric induced ionization. The ionospheric layers based on the vertical distribution of electron density is shown in Figure 1.5.
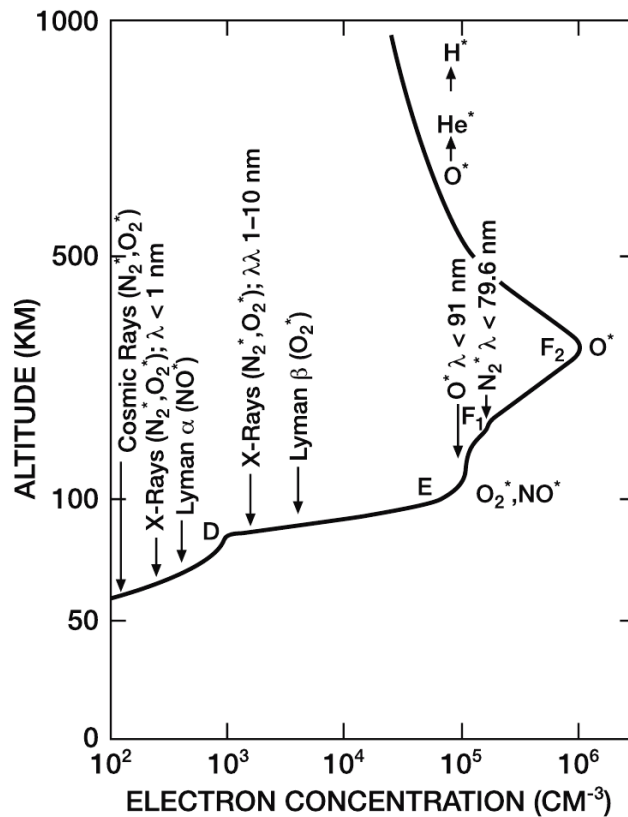
Figure 1.5 - The ionospheric layers based on the vertical distribution of electron density.
Source: Adapted from Brasseur and Solomon (2005)

The dynamics of the upper atmosphere of the Earth are driven by the solar heating tidal forces, auroral energy generated by particle precipitation and Joule heating. On the dayside, solar radiation sets up a global system of neutral winds that tend to flow toward the colder regions on the nightside. When these neutral winds push the ionospheric plasma across magnetic field lines, electric fields and currents are generated. Free electrons (and ions) are the main causes for the both electrical and thermal conductivity of the ionosphere.

The ionospheric electron density distribution in D, E and F regions of the ionosphere during day-time and night-time during solar maximum condition is shown in Figure 1.6.
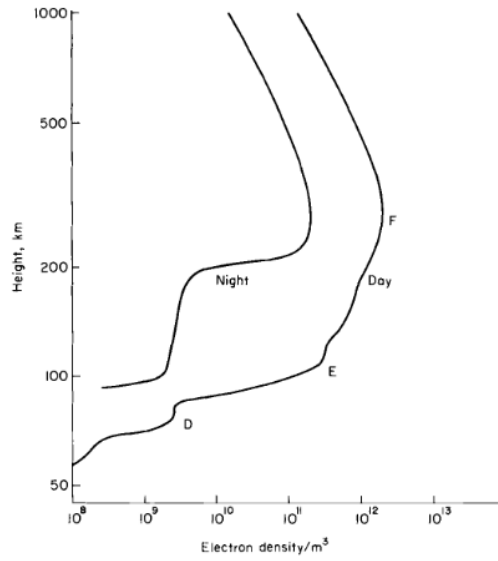
Figure 1.6 - Ionospheric vertical electron density profiles with different layers during solar maximum.

Source: Adapted from Yeh and Liu (1972)

1.4.1 Ionospheric Conductivity and Currents

E and F region are also classified, based on their transport properties, namely, based on two kind of frequencies: collision frequency (ν) and gyrofrequency (Ω) or in general the ratio κ defined as follows:

$$\kappa = \frac{\Omega}{\nu}$$

E and F region are characterized as follows:

$$E - region : \quad \kappa_e > 1; \kappa_i < 1$$
$$F - region : \quad \kappa_e \gg 1; \kappa_i > 1$$

The varying nature of κ in the E and F regions is responsible for varieties of transport dynamics in the ionosphere. More importantly, different κ for ions and electrons leads to different drift and subsequently large currents in the ionosphere which in turn generate varieties of electric fields. Under the action of external forces namely electric field $\vec{E}$ and the wind-drag force $\vec{W}$ associated with tides, the velocity of ions and electrons and current density of the ionospheric plasma, are given by following

18

expression:

$$\vec{u} = \mu \cdot \vec{F} \quad ; \quad \vec{j} = \sigma \cdot \vec{F}; \quad \vec{F} = \vec{E} + \vec{W} \times \vec{B}_o$$

where μ and σ are the mobility and conductivity tensors, given by following expressions:

$$\mu = \begin{pmatrix} \mu_P & -\mu_H & 0 \\ \mu_H & \mu_P & 0 \\ 0 & 0 & \mu_o \end{pmatrix} \quad ; \quad \sigma = \begin{pmatrix} \sigma_P & -\sigma_H & 0 \\ \sigma_H & \sigma_P & 0 \\ 0 & 0 & \sigma_o \end{pmatrix}$$

where (μ_P, μ_H, μ_o) are the Pedersen, Hall and direct mobilities and $(\sigma_P, \sigma_H, \sigma_o)$ are the Pedersen, Hall and direct conductivities respectively. They are given by following expressions:

$$\mu_P = \frac{\kappa}{B_o(1 + \kappa^2)} \quad ; \quad \mu_H = \kappa \mu_P; \quad \mu_o = (1 + \kappa^2)\mu_P$$

$$\sigma = en(\mu_i - \mu_e)$$

where n is the ionospheric density. (μ_i, μ_e) are ion and electron mobilities respectively. In terms of these mobilities and conductivities, the velocity and currents can be written in the following form:

$$\vec{u} = \mu_P \vec{F}_\perp + \mu_H \vec{F}_\perp \times \hat{b} + \mu_o \vec{F}_{||} \tag{1.22}$$

$$\vec{j} = \sigma_P \vec{F}_\perp + \sigma_H \vec{F}_\perp \times \hat{b} + \sigma_o \vec{F}_{||} \tag{1.23}$$

where $(\perp, ||)$ represent the directions perpendicular and parallel to the $\vec{B}_o$ and $\hat{b}$ is the unit vector along the magnetic field direction. It is evident that (μ_P, σ_P) are responses of the ionosphere in the direction of $\vec{F}_\perp$, (μ_H, σ_H) are responses of the ionosphere in the direction of $\vec{F}_\perp \times \hat{b}$ while (μ_o, σ_o) are responses of the ionosphere in the direction of $\vec{F}_{||}$ i.e., along the geomagnetic field $\vec{B}_o$ (KELLEY, 1989).

The altitude distributions of the direct, Pedersen and Hall conductivities are shown in the Figure 1.7. It can be seen that the Pedersen conductivity has two peaks defining the daytime E- and F-regions. The Hall conductivity is comparable to the Pedersen conductivity in the lower E-region and falls rapidly with increasing altitude to be negligible compared to the Pedersen conductivity above about 200 km. The direct conductivity is much greater than the Pedersen and Hall conductivites at all altitudes considering the magnetic field lines as approximately electric equipotentials
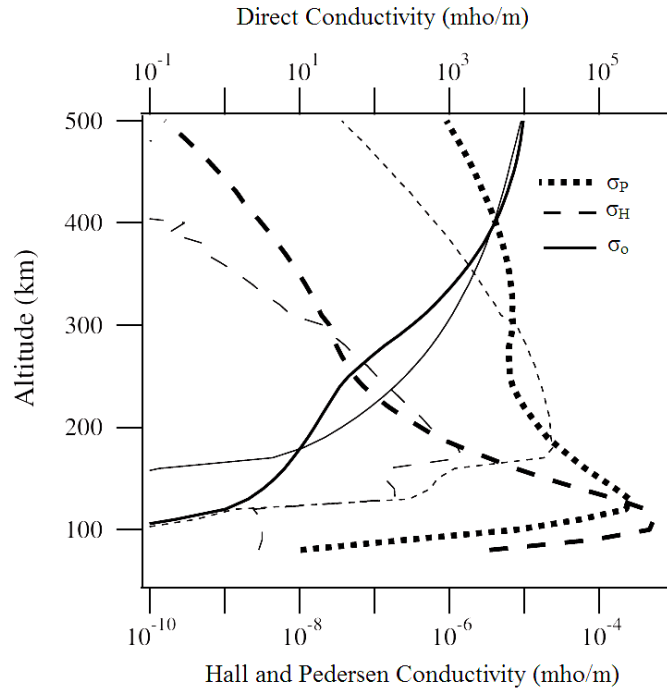
Figure 1.7 - Altitude profiles of the direct conductivity (σ_o), the Hall conductivity (σ_H) and the Pedersen conductivity (σ_P). Heavy curves denote the daytime values. Lighter curves denote nighttime values.
Source: Adapted from Heelis (2004)

(HEELIS, 2004).

1.4.2 Ionospheric disturbances by AGWs and the generation of electric field

It should be noted that the dominant Hall conductivity in the E-region is carried by electrons while the dominant Pedersen conductivity in the F-region is carried by ions. Thus the response to any external forces is rapid in the E- region owing to the large mobility of electrons. This region, thus, carries large current and can be considered as the current generator. One of the important external force is the wind-drag force arising from the atmospheric waves such as AGWs and tides. The currents generated by this force is not divergence-free and as a consequence, a electric field is generated that drives an additional current so that the total current becomes divergence-free. This process is referred as the dynamo as it is based on Faraday's electromotive law. This mechanism can be described in following steps:

- the wind $\vec{W}$ induces an electric field $\vec{E_i}=\vec{W} \times \vec{B_o}$.

20

- the induced electric field drives a current $\vec{J} = \sigma \cdot (\vec{W} \times \vec{B}_o)$

- in general this current is not divergence-free everywhere. Electric charge accumulates wherever $\mathrm{div}(\sigma \cdot (\vec{W} \times \vec{B}_o)) \neq 0$; and

- by Poisson's Law the charge produces a polarization field $\vec{E}_p$, which continually adjusts itself to make the total current divergence-free so that $\mathrm{div}(\sigma \cdot (\vec{W} \times \vec{B}_o + \vec{E}_p)) = 0$ everywhere.

Thus, at any point in the ionosphere, $\vec{E}_i$ represents the electromotive force (e.m.f) induced locally by the wind, whereas the polarization electric field $\vec{E}_p$ may be considered as the sum of the e.m.f.s produced at remote points, which builds up to satisfy the requirement of current continuity in the dynamo circuit. The resulting ionospheric current system is known as solar quiet (S_q) current system (RICHMOND, 1989; RISHBETH, 1997). In the E-layer, the induced electric field ($\vec{E}_i$) and polarization electric field ($\vec{E}_p$) are generally comparable in magnitude. Even during the night-time, when the electron density is smaller than that during the day-time, the magnitude of the direct conductivity is enough to allow currents to flow to maintain the polarization field.

1.5 Motivation

CI in the troposphere is the highly energetic phenomenon that determines Earth's climate as well affects the overlying MLT region. To date the coupling between these two regions via GWs has been studied involving either CI and GWs or GWs and MLT regions. However, the integrated approach involving CI, GWs and MLT dynamics simultaneously is yet to be developed. Moreover, instead of pure GWs, a complete AGWs scenario is desired and is not pursued to date. An integrated approach with the complete AGWs scenario is expected to provide self-consistent dynamical coupling mechanism between troposphere to MLT region. This is the motivation of the present thesis.

1.6 Objectives

The objective of the present thesis is to develop an integrated theoretical framework that includes cause and effects from troposphere to MLT region self-consistently. With this objective, the following aspects are going to be studied: (1) Convective instability (CI) in the troposphere, (2) Generation and propagation of the AGWs, and (3) Atmospheric-Ionospheric Disturbance (AID) in the MLT region arising from the CI+AGWs forcing.

1.7 Innovative nature of the thesis

The thesis intends to pursue the following new studies under this integrated approach:

1. Non-Boussinesq CI simulation, instead of Oberbeck-Boussinesq CI simulation,

2. Complete AGWs dynamics, instead of pure GW dynamics,

3. Secondary AGWs dynamics arising from the MLT-ducting dynamics,

4. OH airglow, Na density disturbances, ionospheric current and ionospheric instability growth rate disturbances in the MLT region.

The current Chapter, which is the first one gives a brief introduction into the atmosphere, airglow emissions and ionosphere. It also includes concise discussion on the acoustic gravity waves, ducting and instability mechanism. The MLT region hosts different types of atmospheric-ionospheric disturbances during high and low solar flux, seasons, convective climate etc. This thesis consists of five chapters, divided according to our concept to better understand the present study. Chapter 2 discusses the theoretical development of convective dynamics. Chapter 3 describes CI+AGWs and associated MLT dynamics. The Chapter 4 gives the atmospheric-ionospheric disturbances (AIDs) due to the excitations of CI+AGWs. Finally, Chapter 5 summarizes the results that constitute the thesis and the future research directions.

2 CI DYNAMICS IN THE TROPOSPHERE

2.1 Introduction

The effect of tropospheric convection on the atmosphere-ionosphere and thermosphere has been studied for a long time. Since temperature decreases with altitude in the troposphere, heated air parcel near the surface of the Earth can readily rise, being less dense than the cooler air parcel above it. The convection arises owing to the convective instability (CI) in the presence of destabilizing negative environmental temperature gradient that competes with the stabilizing adiabatic temperature gradient (SPIEGEL; VERONIS, 1960; OGURA; PHILLIPS, 1962; NORMAND et al., 1977; MARKOWSKI, 2007). Under such temperature profile, the cooler (or more dense) fluid parcel is supported by the heated (or less dense) fluid parcel against the gravity, leading to an unstable equilibrium or CI.

During convection, the altitude variation of the lapse rate in the lower troposphere, significantly departs from that expected from the moist-adiabatic and adiabatic flow conditions. In recent years, such departure is diagnosed as the other processes such as the non-moist/non-adiabatic convective instability (CI) and gravity waves, though very few theoretical attempts are made to examine them in detail. We examine the non-adiabatic contribution to the non-moist or dry CI, arising owing to the weaker lapse rate (than the adiabatic lapse rate) in the lower troposphere. We show that this non-adiabatic contribution can be examined through a parameter η that depends on the ratio of the ambient to convective densities. This parameterization self-consistently monitors the convective adjustment of CI from the non-adiabatic to adiabatic nature. The resulting lapse rate is found to have attributes similar to the observed ones, suggesting that the non-adiabatic contribution to the CI offers an alternative interpretation to the observed lapse rate variation in the lower troposphere. This theoretical framework for the CI in the dry troposphere is given in appendix A. In appendix A, we derive the governing equations for the CI using inviscid hydrodynamic equations. These governing equations include the growth (or wave) equation for the vertical wind w_y, temperature equation and the convective density (total density minus hydrostatic density) equation. The growth equation contains the general expression of Brunt-Vaisala frequency ω_b.

In Figure 2.1, the solid curves show the annual mean altitude profiles of lapse rate (dT_v/dy) at three radiosonde locations, Koror (7.33°N, 134.48°E), Truk (7.47°N, 151.85°E), and Yap (9.5°N, 138.08°E), within the Western Tropical Pacific Warm Pool. These profiles are based on lapse rate data taken up to twice daily for the

period 1999-2001. The thin dashed line is the dT_v/dy obtained by diagnostic model for a moist pseudoadiabat with a pseudoequivalent potential temperature equal to 350 K. Here T_v represents the virtual temperature at height y (km) during moist pseudoadiabat ascent, where all condensate is assumed to be immediately removed from the air parcel. This is in good agreement with observed lapse rates between 5.2 km and 10 km. The thick dashed line shows the diagnostic model dT_ρ/dy for moist adiabat with equivalent adiabat temperature of 350 K. Here T_ρ is the density temperature at height y (km) during reversible moist adiabat, where it is assumed that all condensate is retained by the air parcel. Below the melting level, the reversible adiabat is in better agreement with the observed lapse rate than the pseudoadiabat (FOLKINS, 2006). The melting level denotes a change between two different convective regimes. It also shows a transition from a conditionally unstable to stable atmosphere.
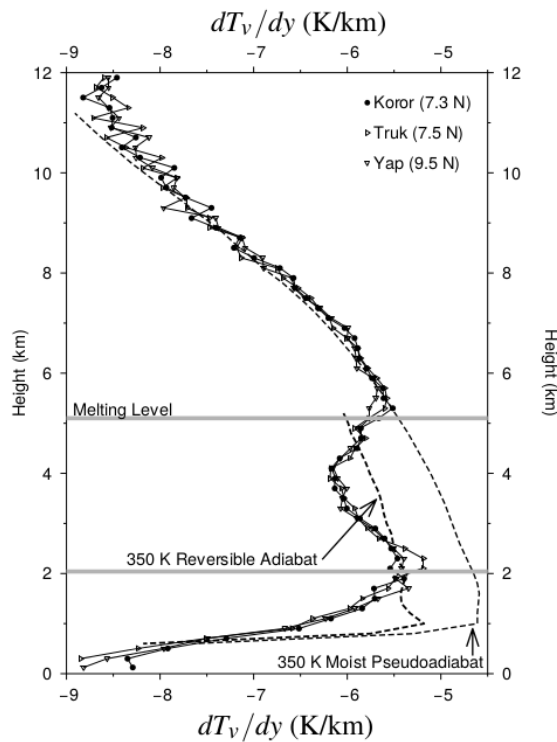
Figure 2.1 - Annual mean altitude profiles of lapse rate (dT_v/dy) variations at three radiosonde locations within the Western Tropical Pacific Warm Pool. These profiles are generated from radiosonde measurements, taken up to twice daily from 1999-2001. The thin dashed line is the dT_v/dy of a moist pseudoadiabat and thick dashed line is the dT_ρ/dy of a reversible moist adiabat, generated by diagnostic approach.]

Source: Adapted from Folkins (2006)

The altitude variation of the lapse rate in the lower troposphere of deep convective tropical regions is an important unsolved problem in tropical meteorology (MAPES, 2001; FOLKINS; MARTIN, 2005). One difficulty is that the lapse rate in between 2-6 km altitude deviates significantly from that predicted by moist adiabatic ascent (FOLKINS; MARTIN, 2005; FOLKINS, 2006). This observed lapse rate variation (as shown in Fig.2.1) is yet to be explained by any modeling study of convective instability (CI).

Folkins (2006) has pointed out that both moist-adiabatic and adiabatic approaches can not account for the observed lapse rate variation in the lower troposphere. He presented a diagnostic model that infers the lapse rate variation arising from the non-moist/non-adiabatic processes such as the diabatic or non-adiabatic convection and the gravity waves. The model relies on a conceptual separation of the density into convective and background domains. In his diagnosis, the observed lapse rate of the tropical lower troposphere is attributed to the non-local effects of the non-adiabatic/gravity wave processes, leading to the updrafts and downdrafts to produce zero net mass flux divergence, when averaged over an appropriate spatial scale.

The diagnostic approach by Folkins (2006) suggests the importance of non-moist/non-adiabatic/non-local contributions to the CI. In this context, a dynamical model of the dry CI involving non-adiabatic processes and non-local dynamics is yet to be examined. The lower troposphere presents a scenario where the lapse rate (γ_e) becomes smaller than the adiabatic lapse rate (γ_{ad}) i.e., ($|\gamma_e| < \gamma_{\text{ad}}, \gamma_e < 0$) (MARKOWSKI, 2007). In this scenario, the non-adiabatic flow condition arises since the temperature gradient is weak and not strong enough to support the adiabatic dynamics which is a rapid process. The governing equations of non-adiabatic CI with the non-adiabatic growth rate expressions are available in literature (NORMAND et al., 1977; LILLY, 1996). These equations are not yet examined in the context of non-adiabatic scenario discussed above that prevails in the lower troposphere. Moreover, the non-adiabatic growth of CI is a complex function of the atmospheric variables (NORMAND et al., 1977) whose parameterization is desired to monitor the evolving flow conditions during the evolution of CI.

In this Chapter, we aim to present a parameterized non-adiabatic growth rate and corresponding nonlocal dynamical equations for the dry CI. Two numerical experiments with and without the nonlocal effects are considered and the temporal-altitude evolution of the updraft, lapse rate and the proposed parameter (η) are simulated. The resulting altitude variation of the lapse rate is examined and compared with

the reported lapse rate variation.

2.2   Parameterized Non-adiabatic model of CI

In appendix A, we derive an equation (A.3) for the updraft (w_y) in which the growth rate or Brunt-Vaisala frequency (ω_b) appears as a function of the atmospheric variables. In appendix A.1.1, based on a general expression of ω_b given by Normand et al. (1977), we propose a parameterized non-adiabatic expression (A.12) of ω_b. In appendix A.1.2, the parameter (η) is identified as the ratio of hydrostatic (ρ_h) to the total density ($\rho = \rho_h + \rho_t$) where ρ_t is the convective density (or non-hydrostatic density). In appendix A.1.2, equation (A.14) for the (ρ_h, ρ_t) and hence for the η is obtained which contain the lapse rate (γ_e) term. The governing equation for the temperature (T) and hence for the γ_e is obtained using the pressure and continuity equations in (A.1). These governing equations are summarized as follows:

$$\frac{\partial^2 w_y}{\partial t^2} = -\omega_b^2 w_y - \eta g \frac{\partial w_y}{\partial y}$$

$$\frac{\partial \rho_t}{\partial t} = w_y \left(\rho_h + \rho_t \right) \gamma_e, \qquad \frac{\partial \rho_h}{\partial t} = -w_y \frac{\partial \rho_h}{\partial y}$$

$$\frac{\partial T}{\partial t} = -w_y T \gamma_e, \qquad \gamma_e = \frac{1}{T} \frac{\partial T}{\partial y} \tag{2.1}$$

The non-adiabatic Brunt-Vaisala frequency ω_b is given by (A.12) as follows:

$$\omega_b^2 = \eta g \left(\gamma_d + \gamma_e \right) \qquad \text{where} \qquad \gamma_d = (\eta - 1) \gamma_{ac}, \quad \eta = \frac{\rho_h}{\rho} \approx 1 - \frac{\rho_t}{\rho_h}$$

where γ_d is defined as the non-adiabatic lapse rate.

This set of equations in 2.1 are solved using Forward-Time Central-Space (FTCS) finite-difference, Crank-Nicholson implicit integration scheme and Successive Over-relaxation (SOR) method. This numerical scheme is discussed in detail by Kherani et al. (2011), Kherani et al. (2012) to simulate the convective instability in the ionospheric plasma and to simulate its influence of the acoustic-gravity waves in the atmosphere.

The simulation domain is one-dimensional, consists of altitude covering 0-20 km altitude with grid resolution $\Delta y = 0.5$km. The time step $\Delta t = 0.5/\omega_b^{max}$ and at the boundaries, gradients are kept constant in time. The initial hydrostatic density ρ_h profile is considered to be exponentially decreasing with scale height equals to 5 km.

In Figure 2.2a, the chosen equilibrium temperature profile is shown. In Figure 2.2b, the initial γ_e multiplied by the initial temperature (T_o), is plotted. For comparison, the adiabatic (γ_{ad}) and auto-convective (γ_{ac}) lapse rates multiplied by T_o are also plotted. It is evident from Figure 2.2b that the chosen temperature profile satisfies $|\gamma_e| < \gamma_{\mathrm{ad}}$ i.e., the profile is conditionally stable in the entire troposphere. The source of forcing can be either of wind type or thermal type. We study a wind type forcing such that a uniform (over altitude) amplitude $= 10^{-3} m/s$ at t=0 is chosen.
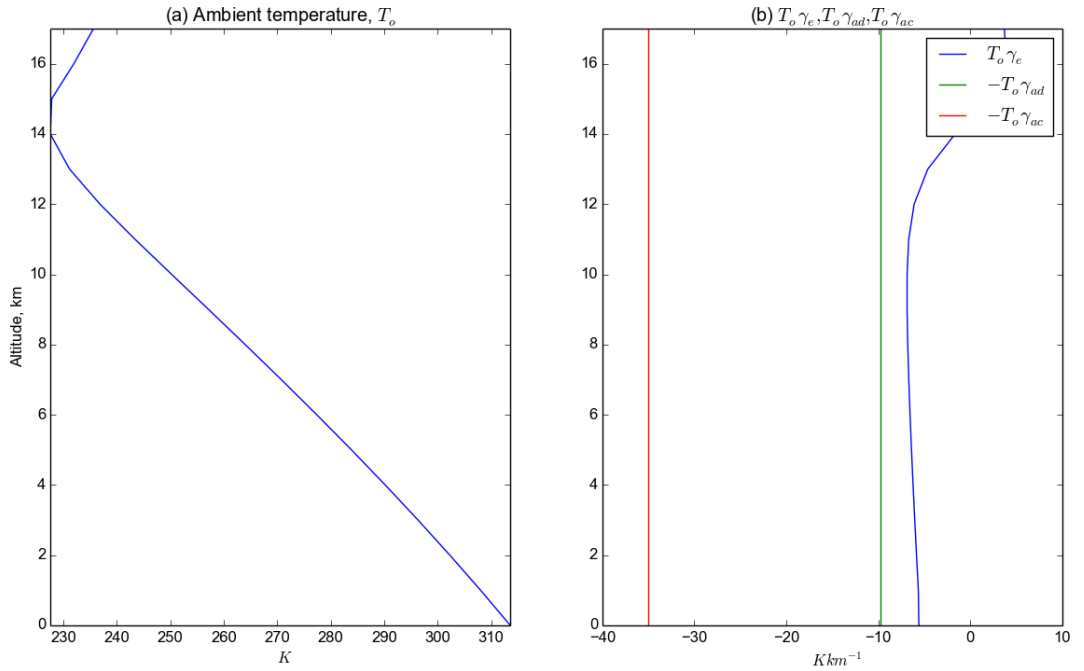
Figure 2.2 - (a) The ambient radiative-convective equilibrium temperature (T_o) profile, (b) The environmental lapse rate γ_e^o multiplied by T_o . For comparison, the adiabatic and auto-convective lapse rates (γ_{ad}, γ_{ac}), multiplied by T_o are also plotted.

2.3 Results and Discussion

Using (2.1-2.2), two numerical experiments, referred as S1 and S2, are carried out. In S1, the non-local term, i.e., the $\frac{\partial w_y}{\partial y}$ term in the governing equation of w_y is not considered while in S2, this non-local term is considered. In these experiments, the temporal-altitude evolution of the $(w_y, \rho_t, \rho_h$ and T) are simulated. From these quantitites, $\eta = \frac{\rho_h}{\rho_h + \rho_t}$ and $\gamma_e = \frac{1}{T} \frac{\partial T}{\partial y}$ are estimated.

2.3.1 Non-adiabatic growth of CI

In Figure 2.3, results are presented for S1. In Figures 2.3a-2.3c, respectively, the temporal-altitude evolution of $\eta = \frac{\rho_h}{\rho_h + \rho_t}$, $T\gamma_e = \frac{\partial T}{\partial y}$ and w_y are shown. In Figure 2.3d, the temporal evolution of the maximum (over altitude) value $\left(w_y^{\max} \right)$ of w_y is plotted as a blue curve. The green curve in the Figure 2.3d represents the average value w_y^{av} of w_y where average is taken over lower troposphere between 0-12 km altitude.
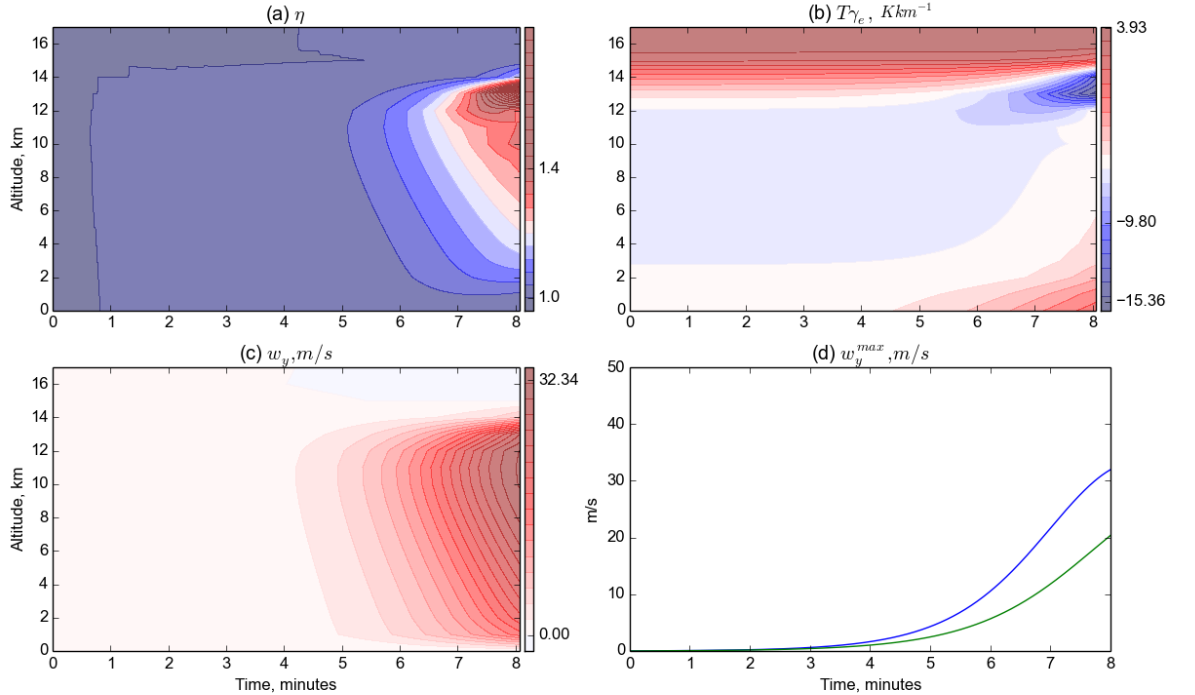
Figure 2.3 - Simulation results for S1: Temporal-altitude evolution of the (a) $\eta = \frac{\rho_h}{\rho_h + \rho_t}$, (b) $T\gamma_e$ and (c) w_y are shown respectively. In (d), blue and green curve represent the temporal evolution of the maximum value $\left(w_y^{\max} \right)$ of w_y and an average w_y^{av}. The average is taken over the density scale height. (ρ_h, ρ_t) represent the hydrostatic and convective density respectively.

We may note the following characteristics from Figure 2.3: (A) $w_y^{\max}$ grows linearly and then exponentially for first 7 minutes and then its growth slows down, (B) At time lapses, η, T and w_y grow in the altitude region where $\gamma_e < 0$ such that the maximum growth is at the altitude near 10 km where the $T_o\gamma_e$ at t=0 (Figure 2.2b) has the maximum negative value, (C) At around t=7 minutes, η becomes equal to $\gamma \sim 1.4$ and simultaneously, $T|\gamma_e|$ becomes equal to $T_o\gamma_{\mathrm{ad}} = 9.8$, (D) After this time, w_y^{max} tends to remain constant ~ 30 m/s though, both η and γ_e continue to grow.

The exponential growth of $w_y^{\max}$ under characteristic (A) is an indication of the linear phase of the CI. The growth suggests that the small wind perturbation of $\sim 10^{-3} m/s$ has grown to 30 m/s within 8 minutes under the action of CI. The characteristics under (A-B) suggest that in spite of the conditionally stable temperature profile, the CI grows in the troposphere. The growth is owing to the non-adiabatic nature of the CI during linear phase ($\eta < \gamma$) when the stabilizing non-adiabatic lapse rate $(\eta - 1)\gamma_{ac}$ remains smaller than the $|\gamma_e|$. As time progresses, both η and γ_e and thus both stabilizing and destabilizing lapse rates grow, leading to the slowing down of the growth, as indicated by the almost constant value of w_y^{max} at t=8 minutes. The characteristic under (C) suggests that as the tropospheric state approaches to the adiabatic state of gas, the environmental lapse rate $|\gamma_e|$ approaches γ_{ad}. This suggests a consistent adjustment of the temperature profile following the nature of compression within the heated fluid parcel and consistent transition of CI from the non-adiabatic-Boussinesq to the Oberbeck-Boussinesq nature.

2.3.2 Non-local effects

In Figure 2.4, the results corresponding to the scenario S2 is presented. We note that in addition to the growth of CI as noted for S1, the updraft and downdraft are developed in the lower troposphere. Such wave structures are also noted in η and γ_e. It is known from the dynamics of CI and gravity waves that the non-local effects arise owing to the various scale heights present in the troposphere. The wave structure noted here is owing to the non-local effects of both the density and temperature variations.

It is also noted from Figure 2.4d that the average w_y^{av} value of updraft is highly reduced in comparison to the large average updraft noted for S1 in Figure 2.3d and remains slightly positive. This is a novel outcome of the present dynamical approach which confirms the outcome of the diagnostic approach presented by Folkins (2006).

For S1, from Figure 2.3c, we note that the CI only excites updrafts. Moreover,
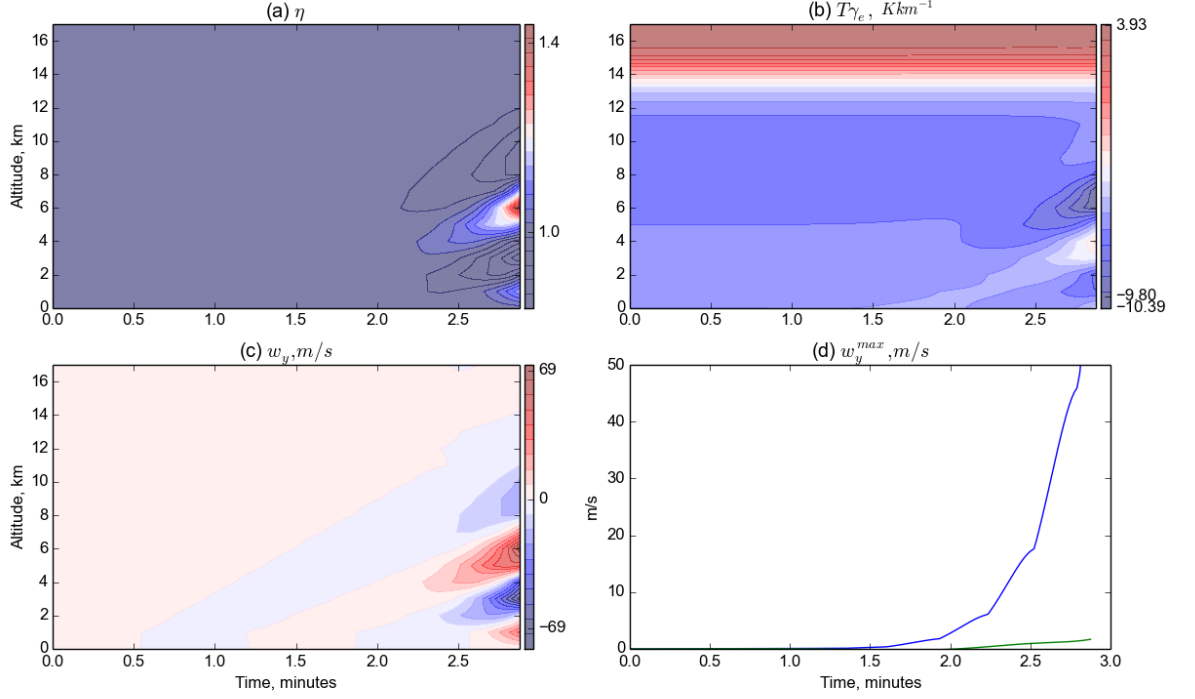
Figure 2.4 - Simulation results for S2: Temporal-altitude evolution of the (a) $\eta = \frac{\rho_h}{\rho_h + \rho_t}$, (b) $T\gamma_e$ and (c) w_y are shown respectively. In (d), blue and green curve represent the temporal evolution of the maximum value $\left(w_y^{\max}\right)$ of w_y and an average w_y^{av}. The average is taken over the density scale height. (ρ_h, ρ_t) represent the hydrostatic and convective density respectively.

also noted from Figure 2.3d that the average updraft is following the evolution of maximum updraft i.e., it is large positive. These two aspects are not consistent with the observations (LUCAS et al., 1994; WEI et al., 1998). On the other hand, for S2, the outcome confirms these observations by revealing that the CI excites both updrafts and downdrafts and that the average updraft is slightly positive.

2.3.3 Simulated and observed lapse rates in the lower troposphere

In Figure 2.5, the altitude variations of the temperature gradient, $T\gamma_e$, during t=0-170 seconds are presented for S2 run. These variations are obtained from Figure 2.4b by selecting the variation at various times. The dashed-black and solid-black variations correspond to the time t=0 and t=135 seconds, respectively. The variation at t=135 seconds can be compared with the Figure 2.1 in which the observed temperature gradient in the lower troposphere was plotted. It can be noted that the simulated lapse rate structure in between 2-8 km altitude is similar to the observed variations. This similarity suggests that the non-adiabatic/non-local contributions examined in the present work, can account for the observed lapse rate variations in the lower troposphere.
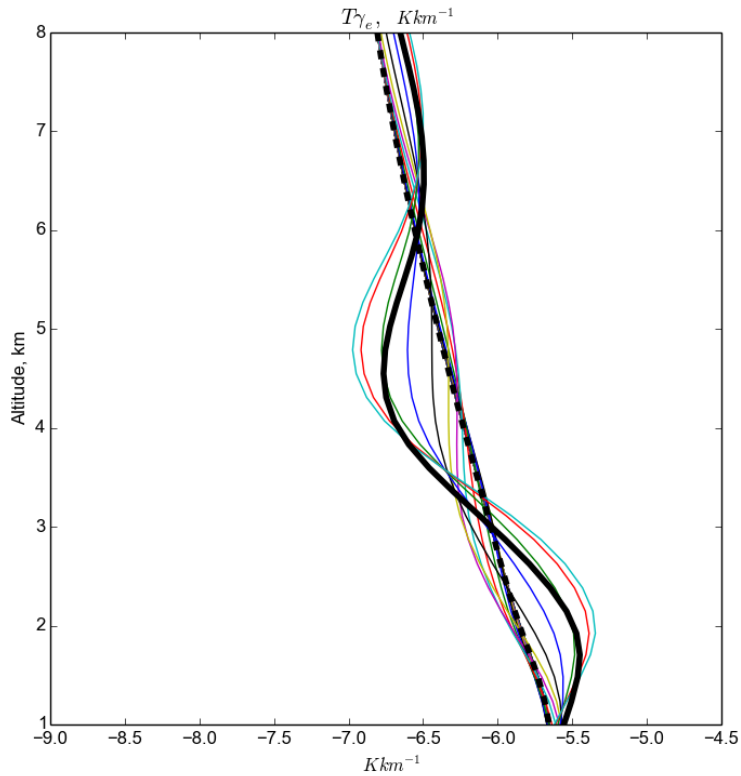
Figure 2.5 - Results from S2: Altitude variations of the $T\gamma_e$ at a few selected times during 0-170 seconds are shown. The dashed-black and solid-black profiles represent the variations at time=0 and 135 seconds, respectively.

2.4 Summary

In this simulation work, we examine the role of non-adiabatic convective instability (CI) to understand the lapse rate variation in the lower dry troposphere. In this region, the non-adiabatic flow condition prevails since the lapse rate is smaller than the adiabatic lapse rate.

In a set of governing equations of the CI, the non-adiabatic contribution to the growth rate is introduced through a parameter η which is a function of ambient and convective densities.

The numerical experiment reveals that the growth of CI is accompanied by the updraft and downdraft in the lower troposphere such that the average updraft remains slight positive. The wave structures in the altitude are simultaneously noted in both η and lapse rate.

The simulated lapse rate variation with altitude is compared with the previously observed variation in the lower troposphere and fairly good agreement is found between them. In particular, the observed depression in the lapse rate between 2-5 km altitude is noted in the simulated variation which was not explained previously. Therefore, the non-adiabatic contributions to the CI in the lower dry troposphere offer an alternative interpretation to the observations.

3 ATMOSPHERIC DISTURBANCES EXCITED BY CI AND AGWs IN THE MLT REGION

3.1 Introduction

In the MLT (Mesosphere-Lower-Thermosphere) region of the atmosphere that lies between 70-140 km altitude, varieties of atmospheric disturbances are observed (TAKAHASHI et al., 1979; HECHT, 2004). Among them, long period-large scale wave-like disturbances and superimposed short period-small scale wave-like disturbances or bands and transient ripples in the OH airglow (TAKAHASHI et al., 1985; TAYLOR; HAPGOOD, 1990; MUKHERJEE, 2003; HECHT et al., 2007; MEDEIROS et al., 2007), C-shaped disturbances and quasi-periodic (QP) descending layer disturbances (KANE et al., 2001; CLEMESHA et al., 2004; CLEMESHA et al., 2011; SARKHEL et al., 2015), are phenomena in the mesosphere which are extensively studied. Presence of these disturbances reflects the nonlinear dynamical state of the MLT region (FRITTS; RAS-TOGI, 1985; TAYLOR; EDWARDS, 1991; HECHT et al., 1997; YAMADA et al., 2001).

Several experimental and theoretical studies reveal that the large scale wave-like disturbances are mainly attributed to gravity waves (GWs)/Inertial gravity waves (IGWs), which are presumably produced in the troposphere and propagate to the mesosphere/lower thermosphere (SWENSON; GARDNER, 1998; WALTERSCHEID et al., 2001; NAKAMURA et al., 2003; VARGAS et al., 2007). On the other hand, the observed transient ripples are more likely generated in situ in the MLT region, and they are the manifestation of the nonlinear wave breaking and subsequent formation of convectively and/or dynamical unstable regions within the MLT region (LI et al., 2005; NARAYANAN et al., 2010). Convective instability results whenever the environmental lapse rate becomes higher than the dry adiabatic lapse rate. Dynamical instability results due to large shears between adjacent layers.

The ripples are highly diversified in nature. They are high frequency small-scale disturbances having periods about the Brunt-Vaisala period ($\sim$ 5 minutes) and horizontal wavelength about the vertical size of the mesopause ($<$ 15 km) (HECHT, 2004). However, much higher frequency ripples having period of order of acoustic cut-off period ($\sim$ 4 minutes) are also observed (HECHT et al., 2007).

Numerical simulations of ripples are few (FRITTS et al., 1997; WALTERSCHEID et al., 2001; HORINOUCHI et al., 2002; SNIVELY; PASKO, 2008) though they have provided detailed insight into the mechanisms involved in the generation of these ripples. Fritts et al. (1997) have shown that the ripples are generated in situ in the MLT duct

by the nonlinear dissipation/breaking of large-scale primary IGWs into secondary IGWs and subsequent development of convective and dynamical instabilities. The convectively and dynamically generated ripples are found to have their phase fronts aligned perpendicularly and parallel to those of the breaking large and small scale wave-like disturbances. Once generated, the ripples may rotate and/or advect along with the background wind. Horinouchi et al. (2002) have presented the simulation of ripples formed by the superposition of GWs arising from the spatially distributed multiple tropospheric sources. Snively and Pasko (2008) have shown the in situ generation of small scale disturbances or secondary GWs in the MLT region arising from the ducting of the primary GWs of tropospheric origin.

Although, from these theoretical studies, the origin of ripples is well understood, the detailed features as they appear in OH airglow images remain to be fully understood. For example, they often appear as disturbances occupying a small portion of the image, suggesting that the mechanisms responsible for them are highly localized (HECHT et al., 2007). Also, they appear mostly oblique, having a wide range of inclination angles with respect to the bands as well appear parallel to the bands (HECHT, 2004). From Figure 3.1(a) we can see the ripples structure in the OH airglow. It can be noted that the observed ripples are oblique to the bands but in the Figure 3.1(b) we can see that the observed ripple structures are parallel to the bands.
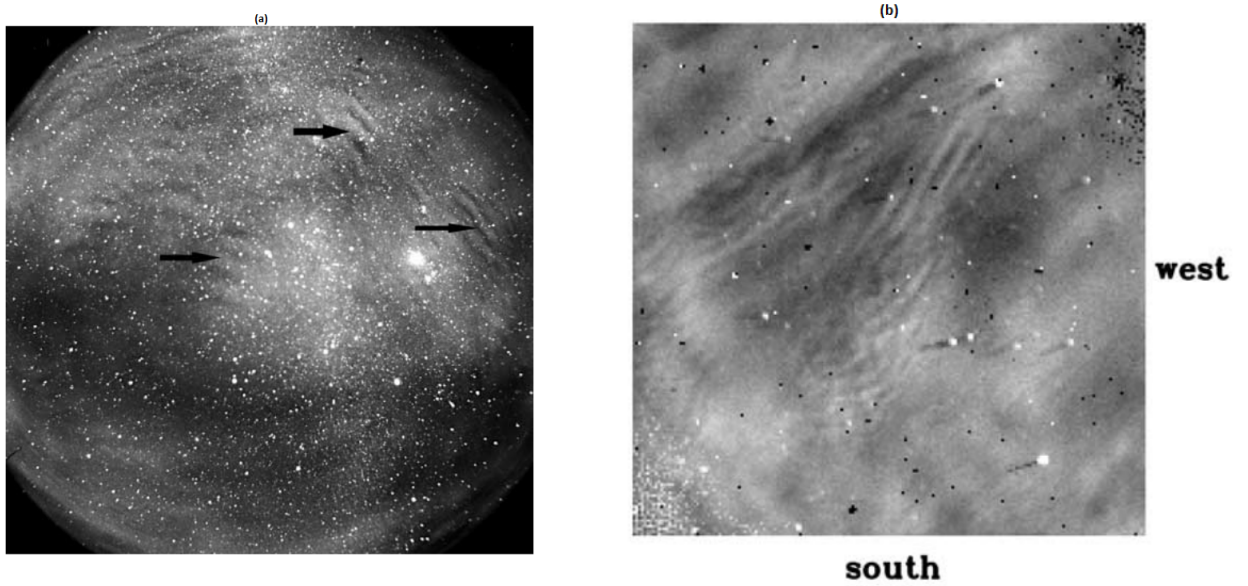
Figure 3.1 - (a) Ripple structures which are oblique to bands are shown in an all-sky image of the OH airglow taken at Bear Lake Observatory. The arrows point to some of the regions where the oblique ripples are present, (b) Ripple structures which are parallel to bands are shown in an image of the OH airglow taken by The Aerospace Corporation.

Source: Adapted from Hecht (2004)

In addition to the ripples, other kinds of disturbances such as the C-shaped Sodium (Na) density disturbances in the lower thermosphere, descending quasi-periodic (QP) Na airglow disturbances are reported and their formation mechanism remain unresolved till date (KANE et al., 2001; CLEMESHA et al., 2004; SARKHEL et al., 2015). Moreover, the descending Na airglow layers reveals an unexplained fast descending rate (Fig: 3.2), apart from the slow descending rate associated with the tidal forcing. The locally produced ripples as well as the fast descending Na density layer are the subject of present investigation.

In Section 3.2 up to 3.3.2 we have performed the numerical experiments of the ripples. At 3.3.3 Section, a fast descending Na layer is shown. These issues are the subject of present investigation in which we perform numerical experiments of integrated CI and AGWs dynamics to simulate these disturbances.

Figure 3.2a shows the atomic Na height-time-concentration map (or lidargram) for the night of 18 to 19 March 2007 over the 80- to 105-km altitude range above Gadanki, India. Figure 3.2b gives a detail of Na distribution in the altitude range

90- to 105-km during the same night. Figures 3.2c and 3.2d give the sequence of individual Na concentration profiles and integrated column content between the base and top of the λ_{image} structure in altitude range 93-100 km, respectively.
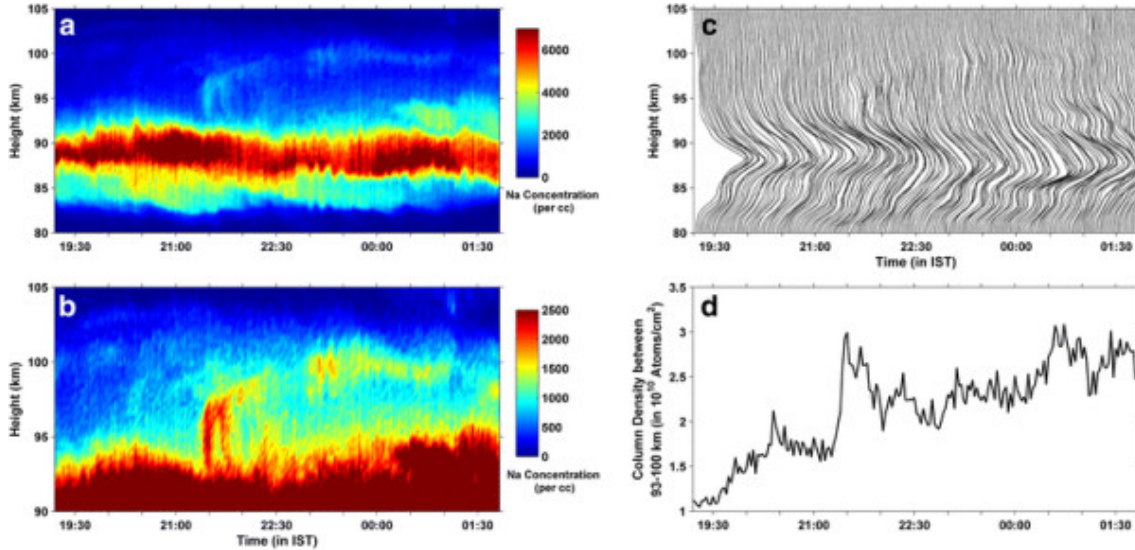
Figure 3.2 - Na density disturbances observed from Na lidar are shown. Rapid descending Na disturbances and C-shaped disturbances above this layer are noted. Their presence remain unexplained. (a) Altitude-time-concentration maps of Na atoms obtained from Na lidar over Gadanki during 18 to 19 March 2007. (b) Height-time-concentration of Na atoms in the 90 to 105 km altitude showing the λ_{image} structure. (c) Sequence of Na concentration profiles. (d) The column density of Na atoms between 93 and 100 km.
Source: Adapted from Sarkhel et al. (2015)

Figure 3.3 shows the altitude and local time variation of the temperature (left) and Na concentration (right). We can see from this figure that the heights of the strong positive gradients in temperature and Na concentration correspond, but also their vertical motions are almost identical. These vertical downward propagation would be expected from the perturbation due to a tidal forcing. Moreover, these slow descending rate of temperature and Na concentration associated with tidal forcing but the fast descending rate of temperature and Na concentration still an unresolved mechanism.
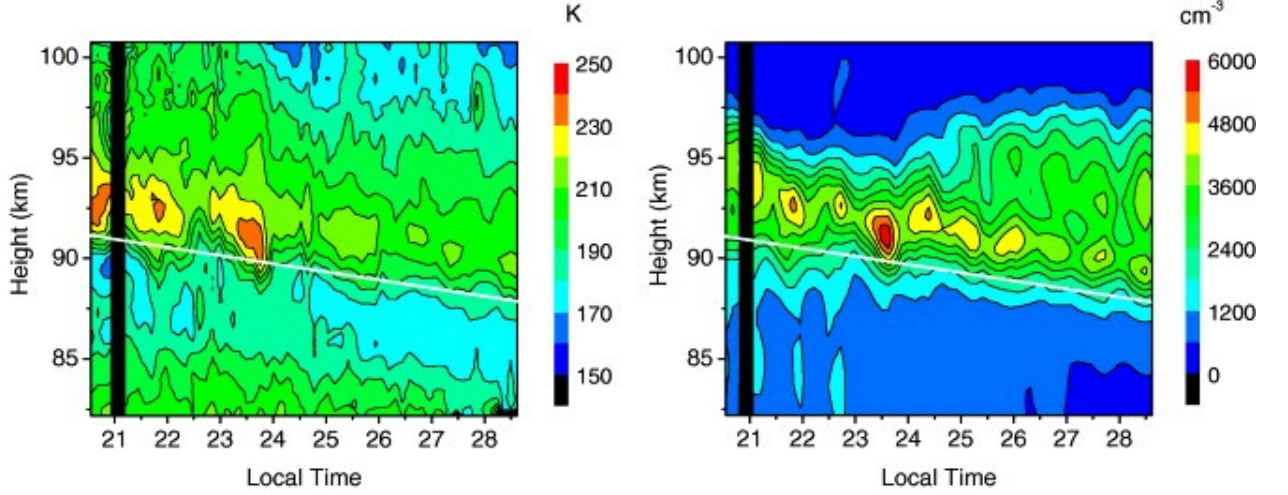
Figure 3.3 - Temperature (left) and Na density (right) disturbances measured from Na lidar are shown. Long-lasting layer with slow descending rate and short-lived layer with large descending rate are observed. The descending nature of long-lasting layer is owing to the tidal forcing which is well understood. However, the presence of short-lived layers and their rapid descending nature remain unexplained.

Source: Adapted from Clemesha et al. (2011)

3.2 Integrated CI and AGWs model

The governing hydrodynamic equations for the CI+AGWs in the atmosphere can be written as follows:

$$\frac{\partial^2 \vec{W}'}{\partial t^2} = -\omega_{BCI}^2 \vec{W}' + \frac{1}{\rho}\nabla(\gamma p \nabla \cdot \vec{W}') - \frac{\nabla p}{\rho^2}\nabla \cdot (\rho \vec{W}') + \frac{1}{\rho}\nabla(\vec{W}' \cdot \nabla)p + \vec{E}_{visc} + \vec{E}_{nl} \quad (3.1)$$

$$\vec{W}' = \vec{W}(\vec{r}, t) + \vec{W}_o(\vec{r})$$

$$\frac{\partial \rho}{\partial t} + \nabla \cdot (\rho \vec{W}') = 0; \quad (3.2)$$

$$\frac{\partial p}{\partial t} + (\vec{W}' \cdot \nabla)p + \gamma p \nabla \cdot \vec{W}' = 0 \quad (3.3)$$

$$\omega_{BCI}^2 = \frac{\eta}{\rho}\nabla p \cdot \left[(\eta - 1)\frac{\nabla p}{p} + \frac{1}{T}\nabla T \right] \quad (3.4)$$

$$\vec{E}_{visc} = \frac{\partial}{\partial t}\left(\nu\nabla^2\vec{W}' + (\xi' + \frac{\nu}{3})\nabla(\nabla \cdot \vec{W}') \right) \quad (3.5)$$

$$\vec{E}_{nl} = -\frac{\partial}{\partial t}(\vec{W}' \cdot \nabla\vec{W}') \quad (3.6)$$

37

where $\vec{W}$ is the perturbation wind, $\vec{W}_o$ is the background wind, $p = R\rho T$ is the pressure, (ρ, T) are the atmospheric mass density and temperature. Here $(\nu = \mu/\rho, \xi' = \xi/\rho)$ are the first and second kinematic viscosities and (μ, ξ) are the dynamic first and second viscosities respectively. The term with ω_{BCI}^2 represents the non-adiabatic convective instability. $\vec{E}_{visc}$ and $\vec{E}_{nl}$ represent the viscous term and non linear saturation term, respectively.

3.2.1 OH Airglow model

OH airglow, also known as the Meinel band, can be observed by several ways such as through ground-based, satellite-based and rocket measurements. The OH rotational temperatures have been measured using several different bands, e.g., (9-4), (8-3), (6-2), (4-2) and (3-1) bands with a combination of different Einstein coefficients (MIES, 1974; LANGHOFF et al., 1986; TURNBULL; LOWE, 1989; NELSON et al., 1990). Its volume emission rate has a maximum around 87 km altitude, so that OH airglow observation can provide a significant source of information about the atmospheric disturbances in the MLT region. We aim to simulate the OH airglow disturbances arising from the CI+AGWs forcing. The OH airglow model used in the present work consists of the following set of chemical equations based on Snively and Pasko (2005):

$$O_2 + O + M \xrightarrow{k_6^{N_2,O_2}} O_3 + M; H + O_3 \xrightarrow{k_2} OH + O_2 \tag{3.7}$$
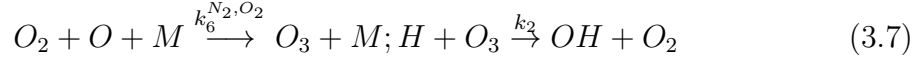
$$V_{OH} = \frac{A(8,3)k_2[H][O_3]f(8)}{L(8)}(m^{-3}s^{-1}) \tag{3.8}$$

$$\frac{\partial[O_3]}{\partial t} + \nabla \cdot (\vec{W}[O_3]) = -k_2[H][O_3] + k_1[O][O_2] \tag{3.9}$$

$$k_1 = k_6^{N_2}[N_2] + k_6^{O_2}[O_2] \approx 1.26 \times 5.84 \times 10^{-45}[O_2](200/T)^{2.5}(m^3 s^{-1})$$

$$k_2 = 1.4 \times 10^{-16} \exp(-470/T)(m^3 s^{-1})$$

$$f(8) = 0.27; L(8)/A(8,3) = 260 + 2 \times 10^{-17}[O_2](m^3)$$

$$O_2 = 2 \times 10^{19}(m^{-3});$$

$$[O] = 5 \times 10^{16} exp\left[-\left(\frac{(r-85)^2}{20^2}\right)\right](m^{-3}); [H] = 1 \times 10^{14} exp\left[-\left(\frac{(r-100)^2}{9^2}\right)\right](m^{-3})$$

where M is a third body of the major gas molecules either an N_2 or O_2. $A(8,3)$, $f(8)$ and $L(8)$ are the Einstein coefficient, branching value for excitation of OH (ν=8) and an empirical loss term, respectively. V_{OH} is the volume emission rate for the NIR photons. Reaction rates $k_6^{N_2}[N_2]$ and $k_6^{O_2}[O_2]$ are given by McDade

et al. (1987) and Swenson and Gardner (1998), respectively (SNIVELY; PASKO, 2005). The temperature-dependent rate coefficient we use in the simulation, $k_2 = 1.4 \times 10^{-16} \exp(-470/T)(m^3 s^{-1})$, describing production of $OH(\nu)$ with vibrational states ν=6–9, where a branching value equal to $f(8) = 0.27$ correspond to the ν =8 state (MAKHLOUF et al., 1995).

3.2.2 Simulation domain and boundary conditions

The simulation domain occupies space in the spherical coordinate system (r,θ,φ) representing altitude, latitude (positive towards north) and longitude (positive towards west). It covers 0-300 km in altitude, -21.7°- -23.7° in latitude and 314°-316° in longitude with grid resolution Δr=2 km and $\Delta\theta$=$\Delta\varphi$=0.02° $\sim$ 2 km while time resolution Δt=2 seconds.

Equations (3.1)–(3.9) are solved numerically using finite-difference method. The implicit Crank-Nicholson scheme is employed to perform the time integration leading to a matrix equation that is subsequently solved by the Successive Over-relaxation (SOR) method. This numerical scheme is discussed in detail by Kherani et al. (2011) and Kherani et al. (2012) to simulate the convective instability in the ionospheric plasma and to simulate its influence of the acoustic-gravity waves in the atmosphere in two dimensions and three dimensions (KHERANI et al., 2005) and discussed in Appendix B. To solve the Equations (3.1)–(3.9), the local magnetic dipole central aligned coordinate system (p,q,φ) is adopted where p, q, φ represent the coordinates outward normal to the Earth's magnetic field, northward directed parallel to the Earth's magnetic field and azimuth angle (positive towards west) respectively. The transformation matrix from spherical to magnetic field coordinate system is described in Appendix C. It should be mentioned that the simulation domain is chosen in the global spherical coordinate system inside which the Equations (3.1)–(3.9) are transformed into the local magnetic dipole coordinate system.

3.2.2.1 Ambient atmosphere: Initial conditions

At $t = 0$, ambient atmosphere inside the defined simulation domain is obtained from the longitude-extended SAMI2 model (HUBA et al., 2000). The SAMI2 model provides the distributions of (ρ_o, T_o) in the altitude-latitude domain. We have incorporated the longitude domain into this model which we refer as the longitude-extended SAMI2 model. The basic introduction of SAMI2 model is given in Appendix D.

In Figures 3.4 (a-c), the initial atmospheric profiles of density (ρ_o), temperature (T_o),

acoustic speed (c_s), the acoustic-cutoff period (τ_a) and the Brunt-Vaisala period (τ_b) are shown. These profile correspond to high solar flux condition during December. The (T_o,c_s) profiles are obtained using NRLMSISE00 model (PICONE et al., 2002) and from them (τ_a, τ_b) are obtained by the following expressions:

$$\tau_a = \frac{2\pi}{\omega_a} \quad ; \quad \tau_b = \frac{2\pi}{\omega_b}$$

$$\omega_a = \frac{c_s}{2}\left(\frac{1}{\rho_o}\frac{d\rho_o}{dr}\right) \quad ; \quad \omega_b = \left(\frac{g}{\theta_p}\frac{d\theta_p}{dr}\right)$$

where $\theta_p = T_o(p_o/p)^{R/c_p}$ is the potential temperature [1] , $p_o = 1000$ mbar, c_p is the specific heat at constant pressure, and R is the gas constant.

In Figure 3.4 (d), a chosen horizontally uniform and constant mean wind profile ($\vec{W}_o = W_{o\theta}\hat{\theta} + W_{o\varphi}\hat{\varphi}$) is shown where ($W_{o\theta}, W_{o\varphi}$) are the northward and westward components of the mean wind. The resultant mean wind blows northward-westward making 45° angle with k_φ.

3.2.2.2 Characteristics of the forcing

At the lower boundary ($r=0$ km), the radial wind forcing, of the following form is given:

$$W_r(r = 0, \theta, \varphi) = 10^{-3}e^{-(\theta-\theta_o)^2/\sigma_\theta^2}e^{-(\varphi-\varphi_o)^2/\sigma_\varphi^2}e^{-(t-t_o)^2/\sigma_t^2}cos(k_\varphi\varphi) \quad (m/s) \quad (3.10)$$

where $\sigma_\theta = 10\Delta\theta$; $\sigma_\varphi = 10\Delta\varphi$; $\sigma_t = 2$ minutes $< \tau_a$

$\theta_o = 22.7°$; $\varphi_o = 315°$; $t_o = 5$ minutes

$k_\varphi = \frac{2\pi}{\lambda_\varphi}$; $\lambda_\varphi = 20\ \Delta\varphi \approx 40$ km

At the lower boundary i.e., at $r = 0$, the outward normal component W_r of the wind $\vec{W}$ is continuous and equals to Equation 3.10. The lower boundary condition at all time acts as the driving source for the excitation of AGWs. At the subsequent time, other wind components (W_θ, W_φ) in entire simulation domain and W_r in entire simulation domain except at the lower boundary are self-consistently determined from the Equation 3.1. The presence of AGWs modifies the atmosphere and ionosphere which in turn alters the characteristics of AGWs itself. This cause-effect mechanism

---

[1] The potential temperature of a parcel of fluid at pressure p is the temperature that the parcel would acquire if adiabatically brought to a standard reference pressure p_o usually 1000 milibars.
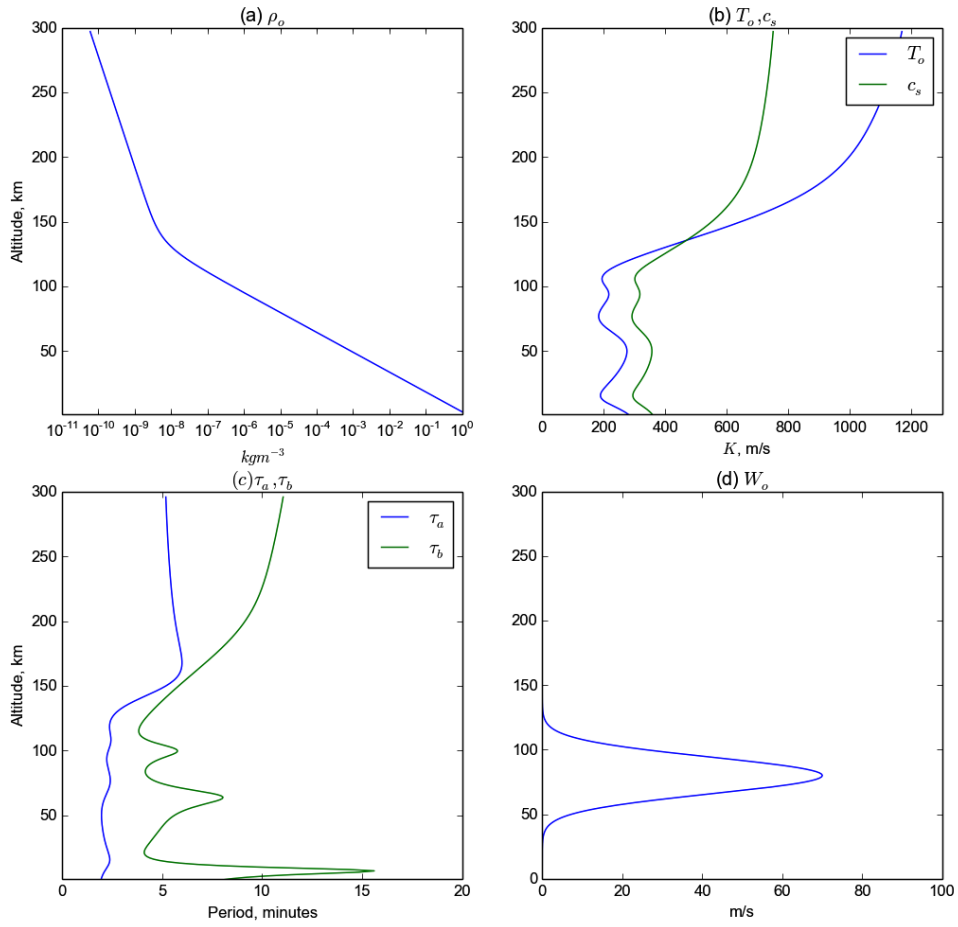
Figure 3.4 - Initial atmosphere: The altitude profiles of (a) atmospheric mass density (ρ_o),
(b) Temperature (T_o) and acoustic speed (c_s), (c) Acoustic cut-off period (τ_a)
and Brunt-Vaisala period (τ_b), (d) Mean wind components ($|W_{m\theta}| = |W_{m\varphi}|$)
which is blowing southward-westward.

continues for next one hour which is the time chosen to stop the simulation.

3.3 Results and Discussion

We perform following numerical experiments for high solar-flux conditions:

(1) NE1: Simulation of AGWs+CI with $\nabla \cdot \vec{W} \neq 0$ in Equation 3.2

(2) NE2: Simulation of AGWs+CI with $\nabla \cdot \vec{W} = 0$ in Equation 3.2

3.3.1 Formation of ripples

We carry out a numerical experiment (referred as NE1) with aforementioned inputs and by retaining $\nabla \cdot \vec{W}$ terms in the Equations (3.1–3.3). Results corresponding to the NE1 are shown in Figures 3.5-3.9. In Figures 3.5-3.7 respectively, three dimensional disturibution of radial component (W_r) of AGWs, % temperature disturbance $\delta T/T_o = (T(t) - T_o)/T_{\max}$ and % OH airglow disturbance $\delta = (V_{OH}(t) - V_{OH}(0))/V_{OH\max}$ are shown. In Figures 3.8-3.9, color images represent δ and arrows represent the wind field disturbance or the amplitude of the AGWs ($\vec{W}$). In Figure 3.8, the horizontal distribution of $(\delta(\theta, \varphi), \vec{W}_h = W_\theta \hat{\theta} + W_\varphi \hat{\varphi})$ corresponding to altitude $r = 84$ km and simulation time $t = 920$ seconds are plotted in the entire horizontal domain and in few enlarged areas. In the upper and lower panels of Figure 3.9, vertical-zonal distribution $(\delta(r, \varphi), \vec{W}_z = W_r \hat{r} + W_\varphi \hat{\varphi})$ corresponding to $\theta = \theta_o$=22.7° and meridional distribution $(\delta(r, \theta), \vec{W}_m = W_\theta \hat{\theta} + W_r \hat{r})$ corresponding to $\varphi = \varphi_o$=315° are plotted at two simulation time t =440 seconds and t= 920 seconds.
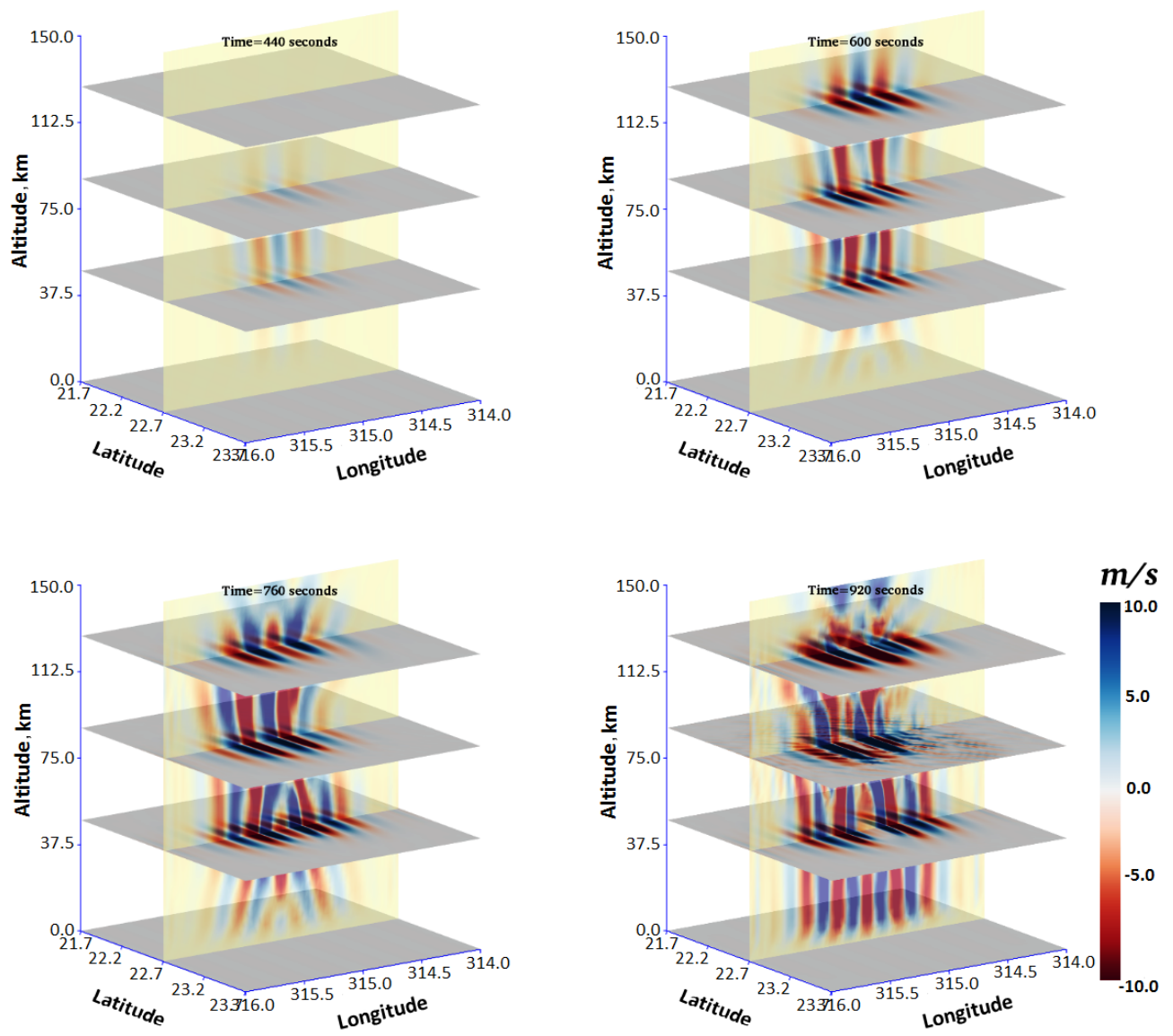
Figure 3.5 - Results from NE1 at simulation time $t = 440, 600, 760$ and 920 seconds: A three dimensional distribution of radial wind disturbance $\vec{W}_r$.
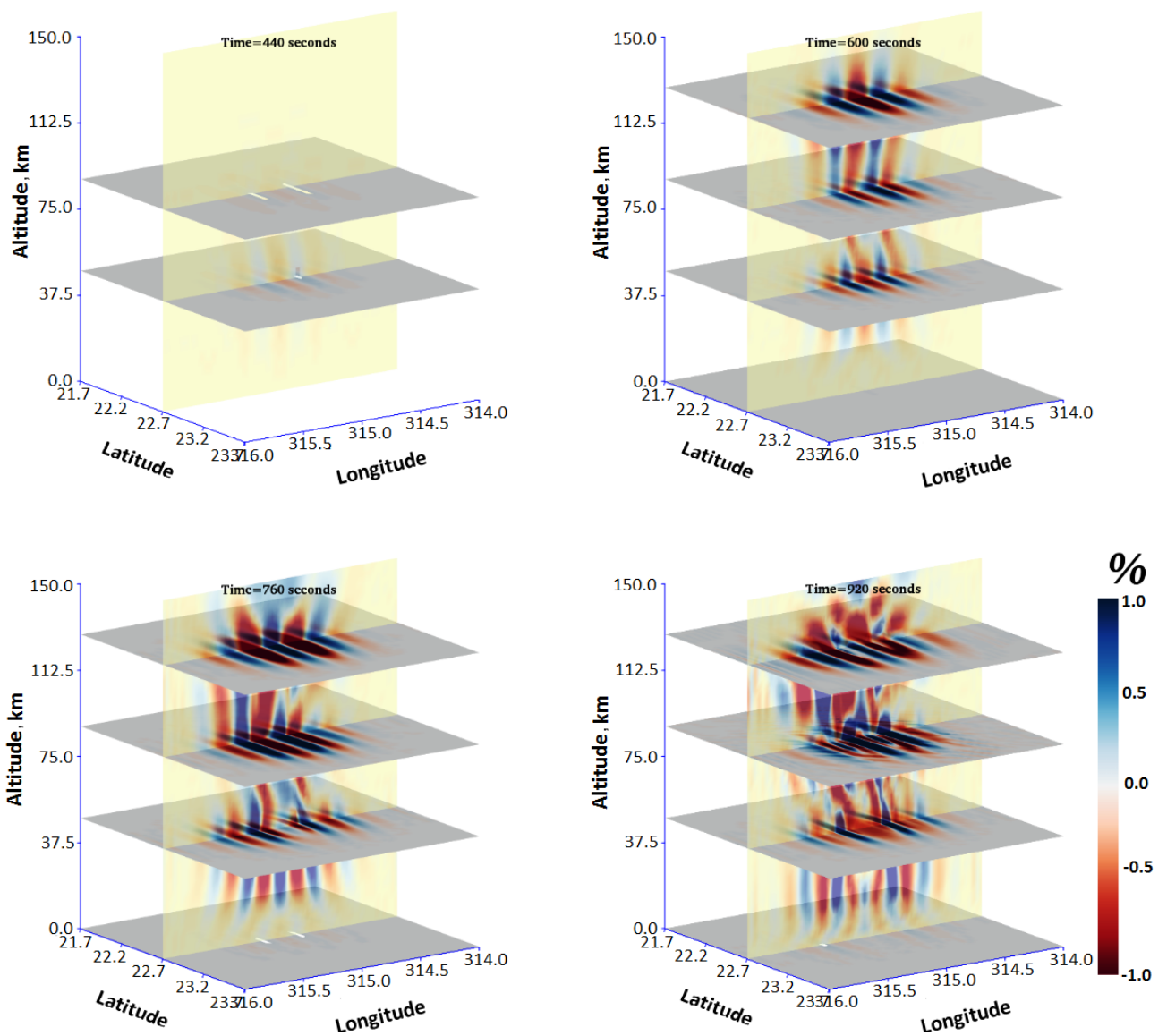
Figure 3.6 - Results from NE1 at simulation time $t = 440$, 600, 760 and 920 seconds: A three dimensional distribution of % temperature disturbance $\delta T/T_o = (T(t) - T_o)/T_{\max}$.
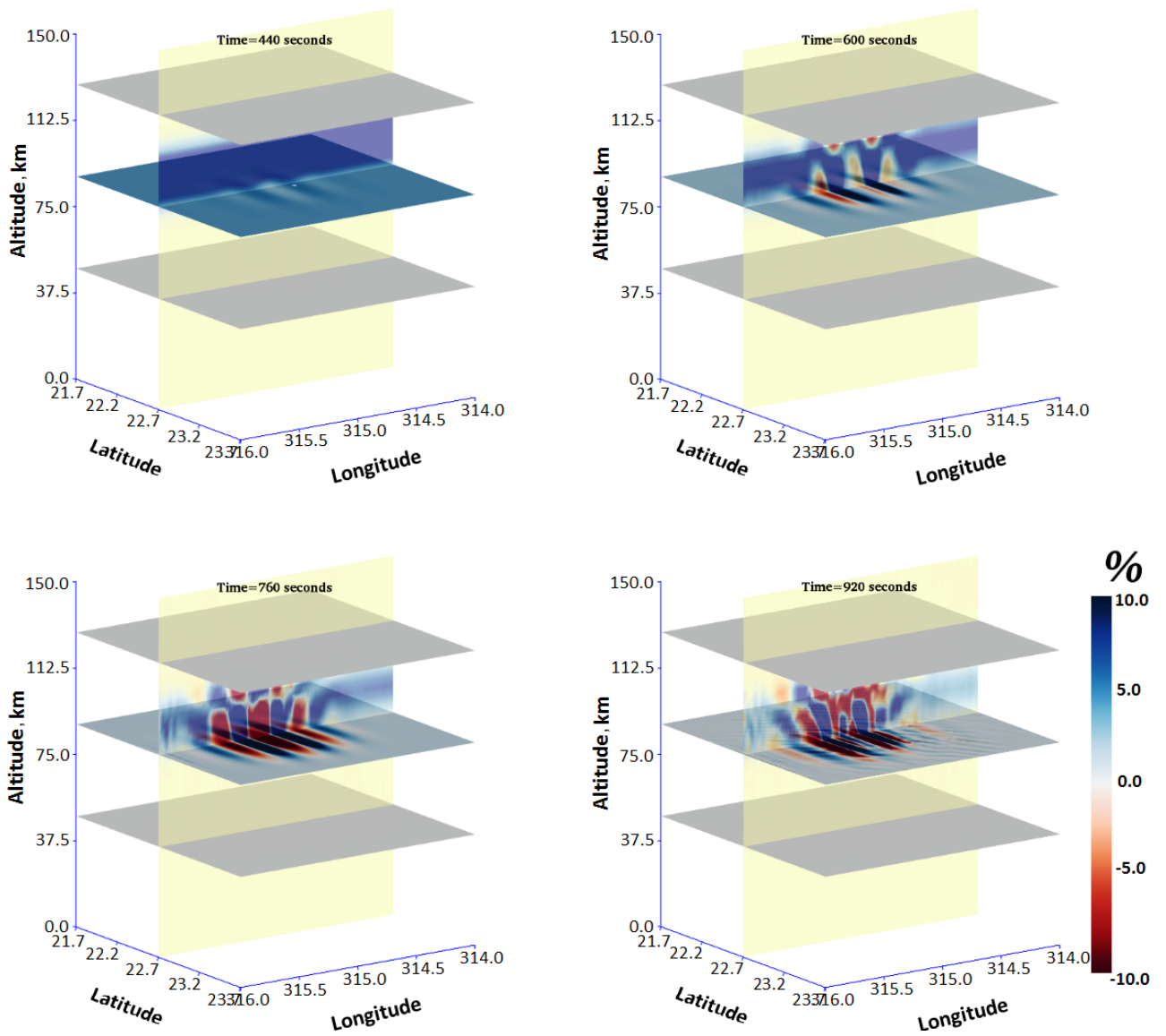
Figure 3.7 - Results from NE1 at simulation time $t = 440, 600, 760$ and 920 seconds: A three dimensional distribution of % OH airglow disturbance $\delta = (V_{OH}(t) - V_{OH}(0))/V_{OH\,\mathrm{max}}$.
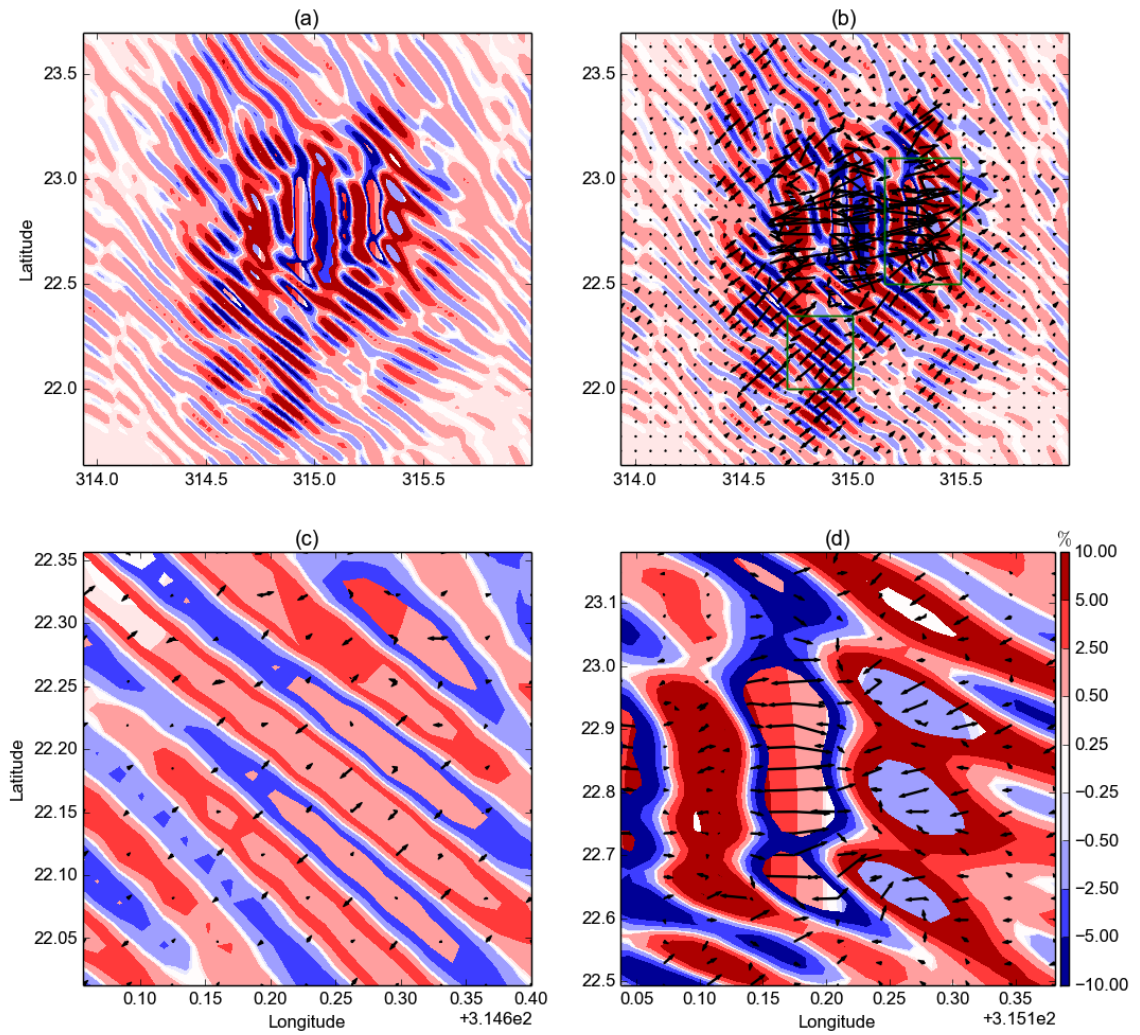
Figure 3.8 - Results from NE1 at simulation time $t = 920$ seconds: The horizontal distribution of atmospheric disturbances at altitude $r = 84$ km. The colored contours and arrows represent the airglow disturbance δ and horizontal wind disturbance $\vec{W}_h = W_\theta \hat{\theta} + W_\varphi \hat{\varphi}$ respectively. Lower panels show the enlarged view of the selected areas shown as rectangles in (b).
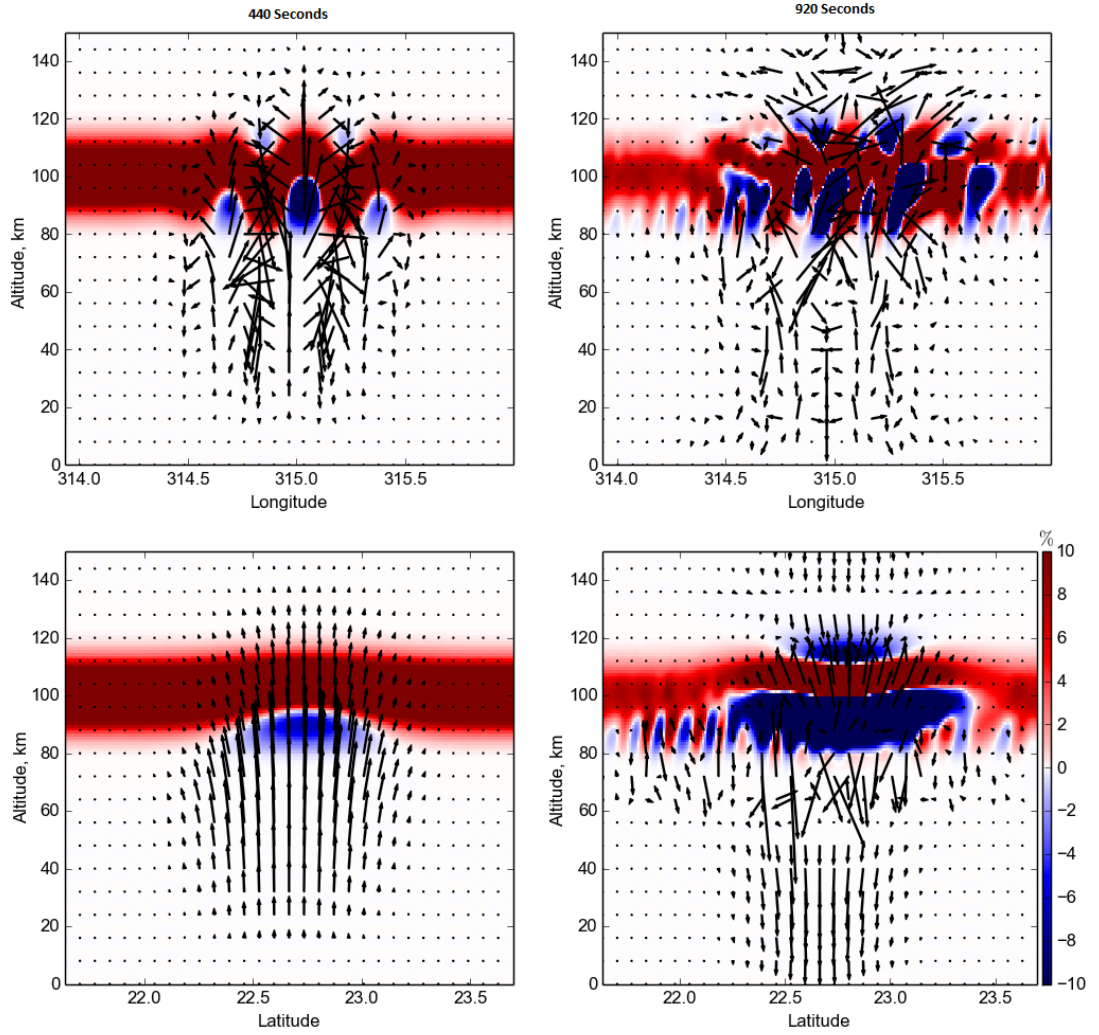
Figure 3.9 - Results from NE1 at two simulation times $t = 440$ seconds (Left panel) and $t = 920$ seconds (Right panel): In the upper panel, the altitude-zonal distribution of $(\delta, \vec{W}_z)$ at latitude $\theta = \theta_o$ is shown. In the lower panel, the meridional distribution of $(\delta, \vec{W}_m)$ at longitude $\varphi = \varphi_o$ are shown. Here $\vec{W}_z = W_r \hat{r} + W_\varphi \hat{\varphi}$ and $\vec{W}_m = W_r \hat{r} + W_\theta \hat{\theta}$.

From these Figures, we note the following features: (A) Formations of ripples near 84 km altitude within 920 seconds ($\sim$ 16 minutes) that are oblique having wide range of inclination angles with respect to the large-scale disturbances, (B) Presence of highly localized ripples, (C) Presence of ripples at the lateral edges of the large-scale/small-scale disturbances showing large convergence and divergence of $\vec{W}_h$ i.e., large $\nabla_h \cdot \vec{W}_h$, (D) Presence of ripples superimposed on the large-scale structures showing mixed wind-field structure of divergence and vortices, (E) Formation of counter-rotating vortices in the ($\vec{W}_z$) wind-fields, (F) Amplification of ($\vec{W}_z, \vec{W}_m$) within three altitude regions corresponding to the three ducting regions.

We carry out another simulation (referred as NE2) that is similar to NE1 but without the $\nabla \cdot \vec{W}$ term in the continuity Equation 3.2. In Figure 3.10 (a-b), corresponding results are shown for $(\delta, \vec{W}_h)_{r=84km}$ and $(\delta, W_z)_{\theta=\theta_o}$ at simulation time $t=$ 920 seconds ($\sim$ 16 minutes). From this Figure, we note the absence of ripples while large and small scale disturbances are formed having counter-rotating vortices in the ($\vec{W}_z$) wind-fields.

In Figures 3.5–3.9 for NE1, the ripples at the lateral edges of the large-scale disturbances have scale size $\sim$0.05° $\approx$5 km while the super-imposed ripples have scale size $\sim$0.1° $\approx$10 km. Strong ripples are in few places and they are highly localized forming different groups. Moreover, they have wide range of inclination angles but mostly oblique to the large scale disturbances. These characteristics are novel outcome of the present simulation study and are consistent with the observed characteristics of the ripples (HECHT, 2004). It should be pointed out that the ripples with such characteristics are also simulated by Horinouchi et al. (2002) by considering that the realistic forcing consists of wavefronts with wavevectors $\vec{k} = k_\varphi \hat{\varphi} + k_\theta \hat{\theta}$ covering wide range of directions and magnitudes. In the present study, the forcing is a monochromatic a single wavevector $\vec{k} = \vec{k}_\varphi$. In spite of such simple forcing, ripples having wide range of inclination angles are formed.

A novel feature is the presence of large $\nabla_h \cdot \vec{W}_h$ across the ripples that are located at the edges of the large-scale disturbances. This suggests that they are formed by the wind divergence mechanism, similar to the formation of the sporadic layer by the ion-drift divergence mechanism in the ionosphere (HALDOUPIS, 2011). Important role of $\nabla \cdot \vec{W}$ in the formation of ripples becomes more evident from numerical experiment NE2 carried out without $\nabla \cdot \vec{W}$ term, that does not show the ripple formations. In the present study, the wind divergence is created by the streaming of the Gaussian wave packet through the atmosphere. The horizontal mean wind ($\vec{W}_o$) provides a
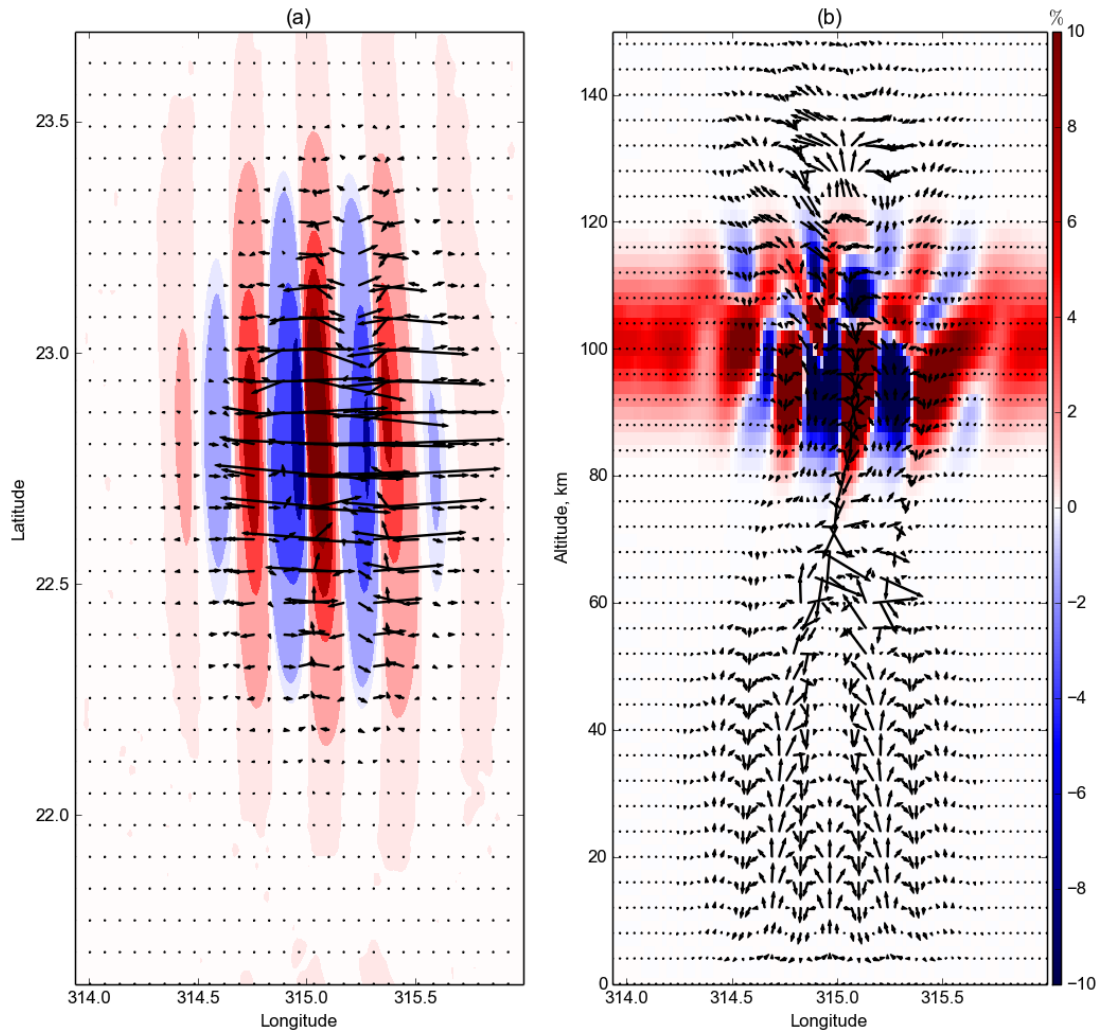
Figure 3.10 - Results from NE2 at simulation time $t = 920$ seconds: (a) The horizontal distribution $(\delta_h, \vec{W}_h)$ at altitude $r = 84$ km and (b) The vertical-longitudinal distribution $(\delta_z, \vec{W}_z)$ at latitude $\theta = \theta_o$ are shown.

scenario in which the large scale Gaussian wave packet (Equation 3.10) is streaming across the atmosphere, opposite to the mean wind. This scenario generates ripples in similar way as a boat streaming through a river generates ripples whose orientation is determined by the relative angle between the streaming direction and the edge of the boat. Therefore, in the present study, the formation of ripples is owing to the wind divergence originated from the streaming of the Gaussian wave packet through the atmosphere. We have performed another experiment (not shown here) similar to NE1 but without the mean wind i.e., $\vec{W}_o = 0$. In this case, both primary and secondary AGWs are generated but ripples are not formed in spite of the $\nabla \cdot \vec{W} \neq 0$ condition. Therefore, the mean wind or relative motion of the atmosphere relative to the forcing is essential for the formation of ripples.

Another novel feature is the wind-field structures of the superimposed ripples, consisting of incomplete vortices and divergences of $\vec{W}_h$. These incomplete vortices are not excited by the Kelvin-Helmholtz instability whose dynamics is not included in the simulation. Rather, they are owing to the superposition of $\vec{W}_z$ divergence (associated with the horizontal cross-section of the counter-rotating vortices as noted from the upper panel in Figure 3.9) and the oblique horizontal mean wind ($\vec{W}_o$).

Formation of counter-rotating vortices in the ($\vec{W}_z$) wind-fields are noted at $t=440$ seconds and $t=920$ seconds in Figure 3.9. These counter-rotating vortices are owing to the AGWs in which vertically large scale acoustic wave disturbances are coupled to the horizontally large scale gravity wave disturbances through the second term $\left(\frac{\nabla p}{\rho} \nabla \cdot \vec{W}' \right)$ in the wave Equation 3.1 of AGWs. As time progresses, these vortices become smaller in size in the mesospheric duct which is an indication of ducting and subsequent generation of secondary AGWs.

The simulated wind divergence mechanism and associated ripples in the present study offers an alternative generation mechanism for the ripples. In fact, the momentum flux divergence is a widely known saturation mechanism of the gravity waves (FRITTS; YUAN, 1989). In general, this includes both advection and wind divergence dynamics and their combined effects have been studied in detail Fritts et al. (1997). However, the present study brings out effects of wind divergence separately. Moreover, these effects are discussed in the context of atmospheric disturbances arising from the AGWs that include the acoustic dynamics. Important role of AGWs and associated acoustic dynamics give rise to rapid and small-scale disturbances within the mesospheric duct is recently presented in the simulation study by Snively (2013). The present study is similar in this aspect and further explores the role of

wind divergence in the ripple formation.

3.3.2 Formation of ripples parallel to the large scale bands

Ripples are diverse in nature, observed both oblique and parallel to the bands (HECHT, 2004). Above, we have simulated the ripples oblique to the bands. In this Section, we attempt to simulate ripples parallel to the bands. We perform another simulation, referred as NE3, similar to the NE1 but with pure Gaussian forcing having no wave-like disturbance in $\hat{\varphi}$ direction i.e., k_φ=0 in expression 3.10. Result for NE3 is shown in Figure 3.11 where horizontal distribution of airglow disturbance δ at 84 km is plotted at t = 920 seconds. From this Figure, we note the presence of band and parallel ripples. Formation mechanism for ripple in this case is same as that in NE1, i.e., the wind divergence mechanism. However, the presence of band is an interesting aspect which are formed in spite of the absence of any wave-like forcing. This is unlike NE1 in which bands are formed in the presence of wave-like forcing. In NE3, bands are arising from the interaction between Gaussian forcing and drifting background in which circular wavefronts generated by AGWs in the amosphere acquires both band and ripple structures.
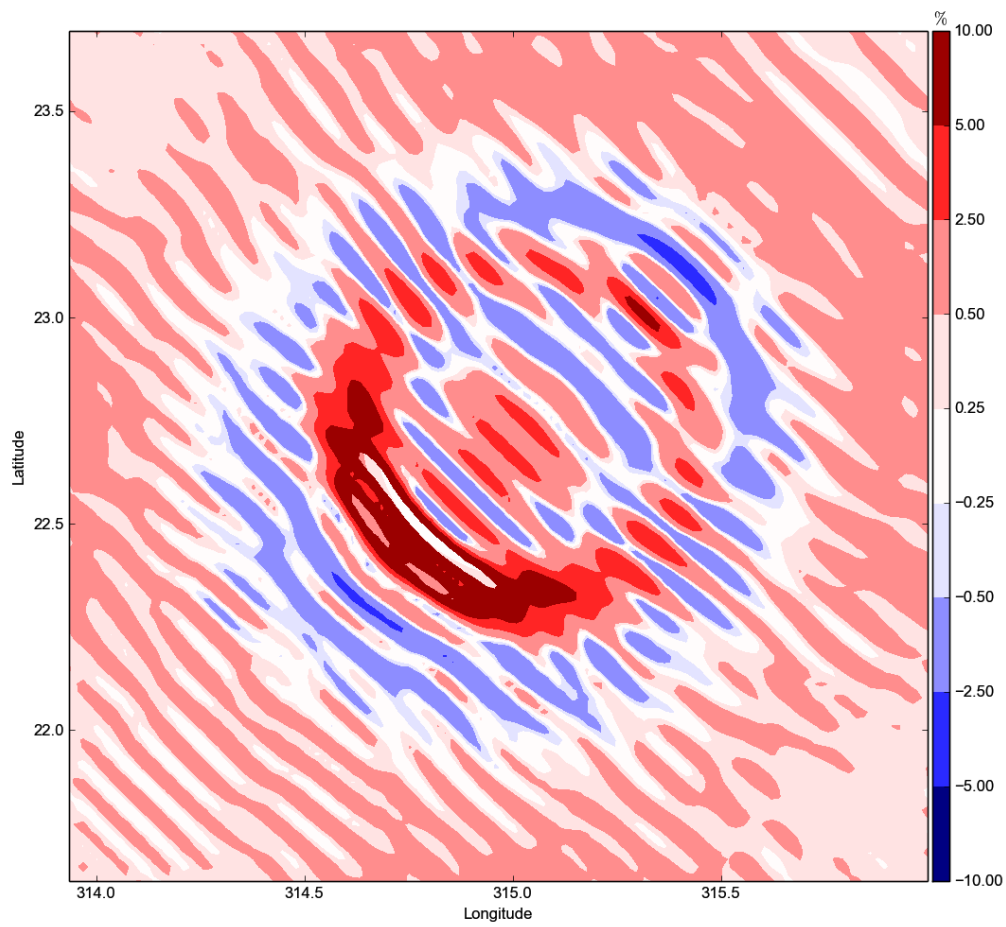
Figure 3.11 - Results from NE3 at simulation time t =920 seconds: The horizontal distribution of atmospheric disturbances at altitude r = 84 km.

3.3.3 Formation of descending disturbances and C-shaped disturbances in the MLT region

In the MLT region, short-lived descending quasi-periodic (QP) disturbances are often reported from the Na lidar observations (CLEMESHA et al., 2010; CLEMESHA et al., 2011) as shown in Figure 3.3 in Section 3.1. Also, in the lower thermosphere in between 100-110 km altitude region, C-shaped disturbances are observed (KANE et al., 2001; CLEMESHA et al., 2004; SARKHEL et al., 2015) as shown in Figure 3.2 in Section 3.1. Their presence remains unexplained from the theoretical point of view.

To simulate Na density disturbances, we assume following altitude profile of Na density, $n_{Na} = 4 \times 10^9 exp\left[-\left(\frac{(r-90)^2}{\sigma^2}\right)\right](m^{-3})$, where the prescribed source is a Gaussian envelope over an altitude of half-width σ=20 km, if r >90 and σ=10 km, if r <90.
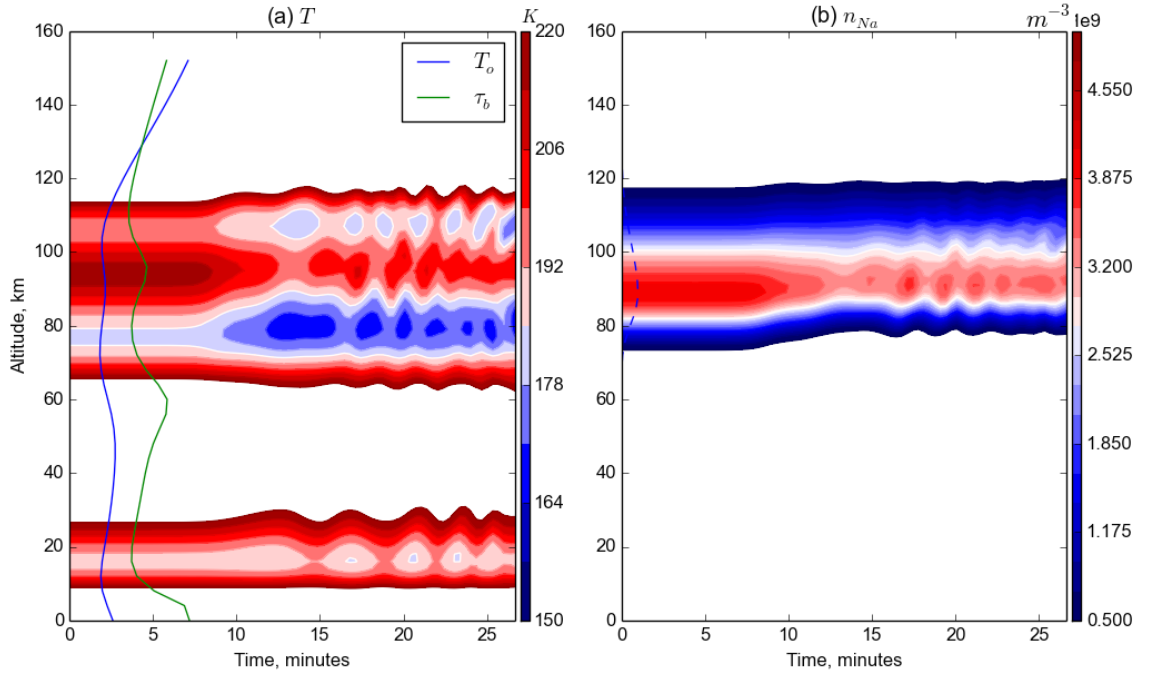
Figure 3.12 - Simulation results showing temporal-altitude distribution of the temperature and Na density (n_{Na}) disturbances at (θ_o, φ_o). In (a), blue and green profiles represent the initial temperature and Brunt-Vaisala period and in (b) dashed-blue profile represents the initial Na density, normalized to the maximum density.

In Figure 3.12, we present simulation results for NE1 in which temporal-altitude distribution of temperature and Na density disturbances at (θ_o, φ_o) are shown. We note the presence of descending and QP disturbance layer of temperature in 80-110 km altitude region. There are two denscending layers appearing around two temperature minima in the MLT region. Also, another layer appears in between them, having comparatively larger temperature.

The simulated temperature and Na density disturbances in Figure 3.12 are in fairly good agreement with the observed disturbances in Figures 3.2–3.3. Therefore, QP descending disturbances as observed in the temperature and Na density are explained based on AGWs arising from the wind forcing at the ground.

A noteworthy difference between observed and simulated Na density disturbance is that the C-shaped disturbance is not obviously evident in the simulated n_{Na} though it is evident in the simulated temperature disturbance. In order to verify the presence of C-shaped disturbances in the Na density, we plot % density disturbance $\delta n_{Na} = (n_o - n_{Na})/n_{\max}$ in Figure 3.13. In this Figure, presence of disturbed Na layer above the descending layer is evident. This layer consists of QP disturbances and some of QP resemble C-shaped disturbances. Moreover, this layer is weaker than the underlying descending layer. These aspects are in fairly good in agreement with the observation shown in Figure 3.3. Therefore, the origin of observed weak Na disturbance layer with C-shaped QP structures within it can be explained based on the AGWs driven disturbances in the ducting MLT region.
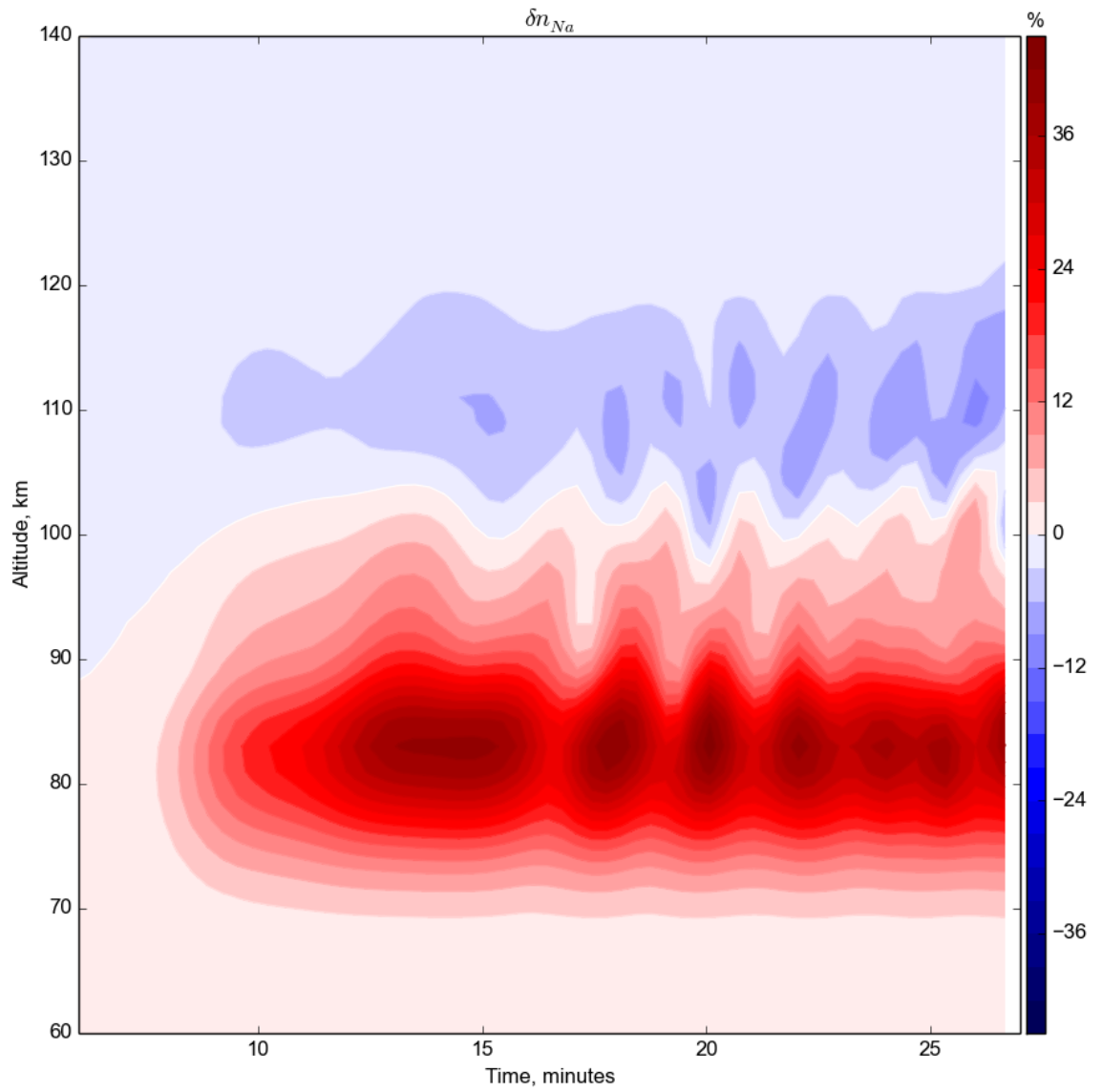
Figure 3.13 - Simulation result showing relative Na density disturbance, defined as $\delta n = (n_o - n_{Na})/n_{Na}$ where (n_o, n_{Na}) are the initial and instantaneous Na density as plotted in Figure 3.12 (b).

MLT region offers varieties of obstacles to the AGWs owing to the rapid altitude variation of the temperature and density scale heights. These obsctacles are referred as ducts and they can be categorized in to two types: thermal and density ducting (SNIVELY; PASKO, 2008; KHERANI et al., 2011). These are the two regions near 90-100 km and 100-110 km respectively where thermal and density scale heights change suddenly, leading to the negative ω_b^2, depending on the vertical wavelength of the AGWs. Here ω_b is the Brunt-Vaisala frequency defined in section 1.2.1 in Chapter 1. A general wave equation of AGWs is written as Equation 1.4 in the Chapter 1.

Based on this form, Kherani et al. (2011) have described the ducting mechanism, mathematically, as follows: the ducting arises in the presence of fourth term in the R.H.S. of Equation 3.1. All wavelengths $\lambda \leqslant h$ are ducted within these ducts where h is the spatial scale associated with the altitude variation of the scale height of the temperature and density. The amplitude W of AGWs grows in the ducting region. However, as the W grows, the viscous dissipation arising in the presence of fifth term in Equation 3.1, which are proportional to W, also grows. This leads to the momentary equlibrium between growing and dissipating mechanism. At this moment, AGWs escape to the higher heights. As they escape to higher altitude and/or dissipate in the MLT region, the amplitude begins to decrease, leading to the weakning of the viscous dissipation. As a consequence, the amplitude of AGWs again begins to grow owing to the ducting which again attains the momentary equilibrium. Thus, the MLT region oscillates in time owing to competition between ducting and dissipation and at the equilibrium AGWs are launched to the thermosphere and/or dissipate in the MLT region. This oscillation time is of the order of Brunt-Vaisala period in the MLT region which is $\sim$ 5 - 7 minutes. Indeed, the lidar observations show the QP disturbances in the MLT region that are attributed to the ducting of AGWs (CLEMESHA et al., 2010). Thus, the MLT region acts as a source of forcing for the upper thermosphere or generation of secondary AGWs, despite that the primarily source resides in the troposphere. The ducting leads to the QP large thermal disturbances in the MLT region, as noted in Figure 3.12 (a). These ducted AGWs also give rise to the density disturbances in the constituents residing in the MLT region, such as the Na density disturbances, as noted in Figure 3.12 (b).

In Figure 3.13, we note the presence of QP disturbances of period $\sim$ 3–5 minutes though the $\tau_b = \frac{1}{\omega_b}$ in the MLT region larger than 4 minutes. Such higher frequency ($<$ 4 minutes) QP are owing to the nonlinear modification of τ_b in the MLT region arising from nonlinear CI+AGWs dynamics.

3.3.4 Solar-flux effects

Simulation results presented above are performed with high solar-flux background conditions. Atmospheric disturbances in the MLT region are observed in both high and low solar flux conditions, revealing similar charcateristics with one obvious difference which is a slight weakening in temperature disturbances under low-solar flux conditions. Concerning Na density disturbance, no such study is done. In this section, we present the simulation results under low-solar flux conditions. The density and temperature profiles are shown in Figure 3.14.
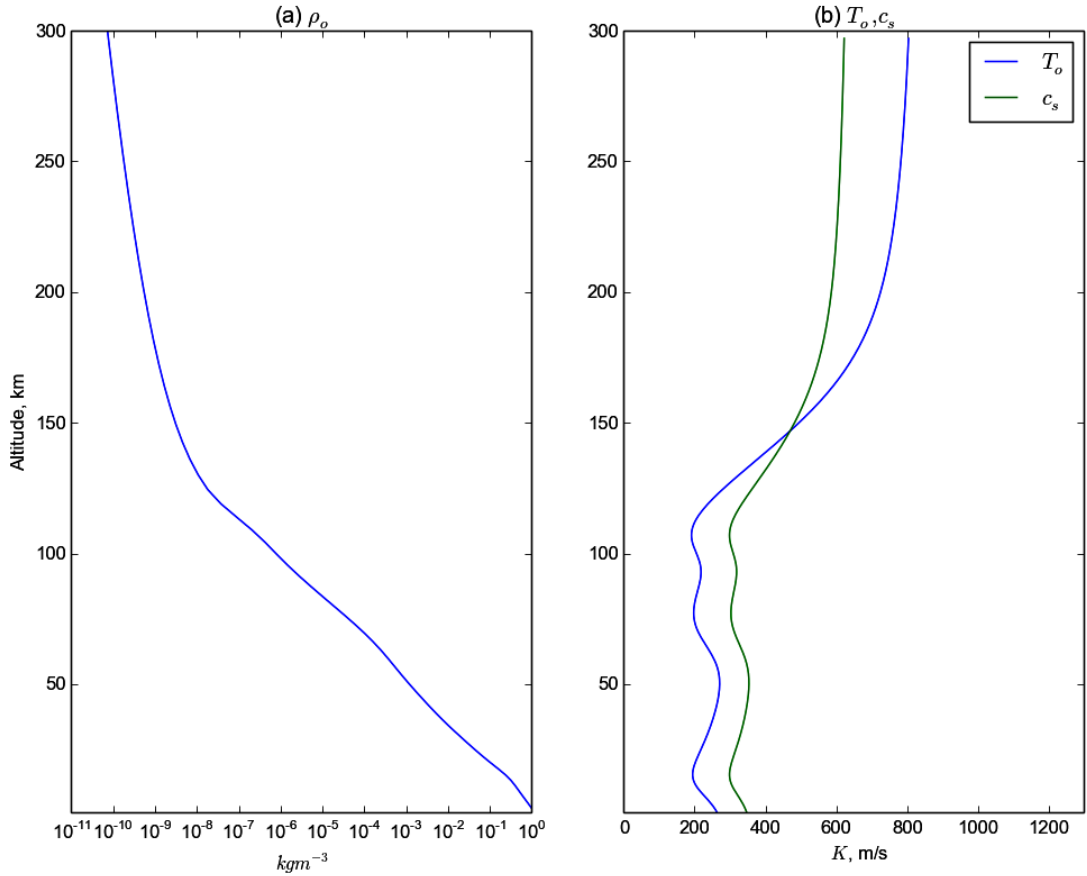
Figure 3.14 - Ambient atmospheric density, temperature and sound speed profiles for low solar-flux ($F_{10.7}$=50.0) condition.

In Figure 3.15, simulated temperature and δn_{Na} disturbances are shown. We note the weakening of temperature disturbance in comparison to high solar-flux conditions in Figure 3.12. The Na density disturbance reveals weakening of C-shaped disturbances

while strengthening of underlying descending layer.
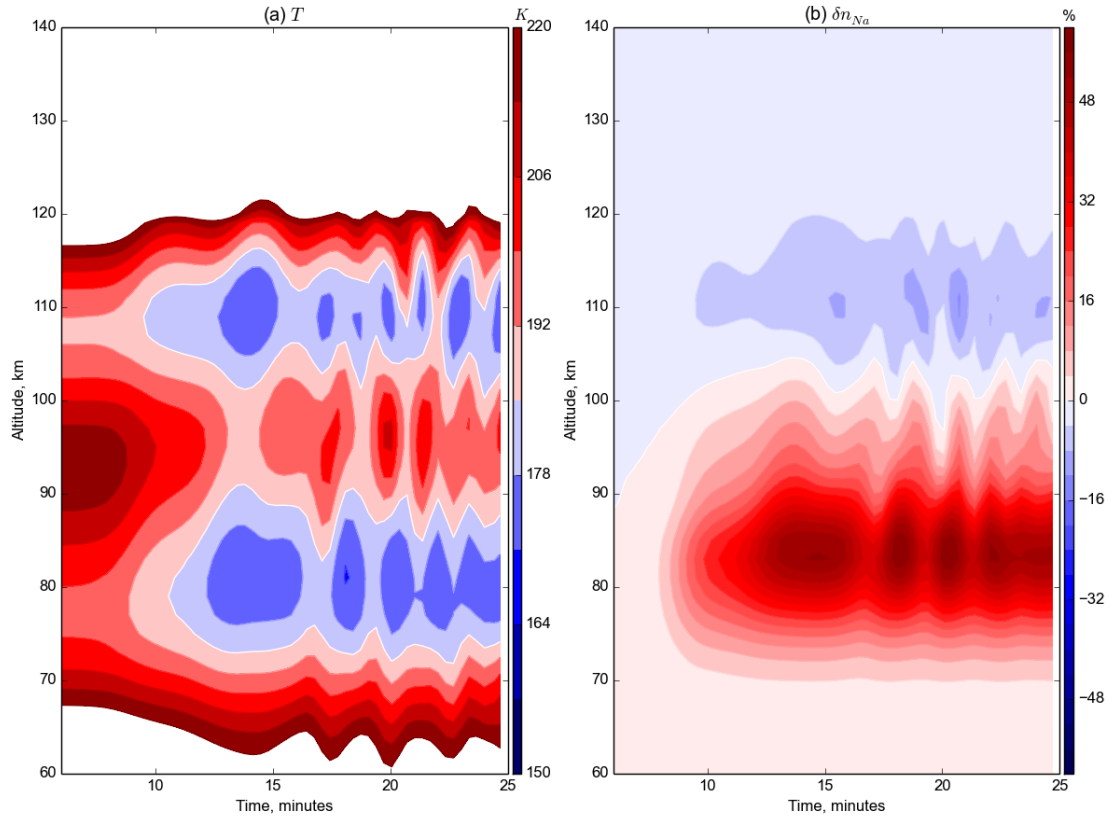
Figure 3.15 - Simulation result showing temperature and relative Na density disturbance, defined as $\delta n = (n_o - n_{Na})/n_{Na}$ where (n_o, n_{Na}) are the initial and instantaneous Na density as plotted in Figure 3.12 (b).

3.4 Summary

In this Chapter, we present results from several numerical experiments of CI+AGWs simulation with the objective of simulating the atmospheric disturbances such as ripples, quasi-periodic (QP) descending disturbances and C-shaped disturbances, whose formation mechanisms are not well understood till date.

Firstly, we present the simulation of the mesospheric ripples arising from the CI+AGWs dynamics. These AGWs are excited by the high frequency monochromatic wave-like wind forcing at the ground and simulation is performed in the presence of a horizontally uniform constant mean wind blowing $45°$ from the forcing wave-front.

We perform two numerical experiments, with and without the wind divergence $(\nabla \cdot \vec{W})$ in the continuity equation while retaining it in the wave and energy equations. In these experiments, the excited AGWs propagate from ground to the lower thermosphere, with large amplification in the ducting regions wherein subsequent generation of small scale disturbances are noted. In the first experiment referred as NE1, we note the formation of ripples in the mesospheric ducting region. These ripples have a wide range of inclination angle but mostly oblique to the large-scale primary and small-scale secondary AGWs wave-fronts. A novel outcome is the formation of strong highly localized ripples in the regions of large horizontal wind divergence. These ripples have scale size ~ 5 km and they reside near the lateral edges of the large-scale wave-fronts. Another set of ripples of scale size ~ 10 km are formed within the large-scale disturbances.

Another novel outcome is that in the numerical experiment (referred as NE2) without the wind divergence term, the ripples ceased to exist, indicating the important role of wind divergence to generate them. Though the momentum flux divergence leading to the saturation of the gravity waves has been extensively studied in the past, the contribution from the wind divergence alone had remained unexplored. Inclusion of this contribution in the present study leads to the formation of ripples having features similar to the observed features which were not fully understood in the past. Therefore, along with the other known mechanisms such as the convective and dynamical instabilities, the wind divergence mechanism presented in this study can contribute to the formation of ripples.

From the third experiment referred as NE3, similar to the NE1 but with pure Gaussian forcing having no wave-like disturbance in $\hat{\varphi}$ direction. From this experiment,

we note the presence of band and parallel ripples. This is unlike NE1 in which bands are formed in the presence of wave-like forcing. In NE3, bands are arising from the interaction between Gaussian forcing and drifting background in which circular wavefronts generated by AGWs in the amosphere acquire both band and ripple structures.

We perform the simulation of the Na density disturbances under NE1 and noted the presence of two descending layers near 80 and 100 km altitudes. These two layers are composed on quasi-periodic disturbances having periods in the range of 3-5 minutes. In addition, the C-shaped structures are noted in above 100 km altitude. These characteristics are in fairly good in agreement with the observations. We have also presented numerical experiments corresponding to the low solar flux conditions. We found the weakening of temperature disturbance during the low solar flux conditions. The Na density disturbance reveals weakening of C-shaped disturbances while strengthening of underlying descending layer.

4 ATMOSPHERIC-IONOSPHERIC DISTURBANCES (AIDs) EXCITED BY CI AND AGWs

4.1 Introduction

E region of the ionosphere is collocated with the MLT region and dissipative AGWs dynamics in the MLT region can greatly influence the E region through the atmosphere-ionosphere coupling. This coupling is established through collisions between neutrals and E region plasma and the subsequent flow of plasma current across the Earth's magnetic field, which is referred to as E region dynamo.

The E region dynamo is driven by the wind in the atmosphere mainly of tidal origin (BAKER; MARTYN, 1953; CHAPMAN, 1956; HEELIS et al., 1974). The tidal wind ($\vec{W}$) gives rise to the current $\vec{J}^W$ which is mainly carried by electron and is perpendicular to the Earth's magnetic field ($\vec{B}_o$). This current is not divergence free ($\nabla \cdot \vec{J}^W \neq 0$) owing to the spatial variation in the E region density and wind. As a results, charges or dynamo electric field ($\vec{E}_d$) builds up across the boundaries such that it drives an opposite current ($\vec{J}_d$) to make the total current ($\vec{J} = \vec{J}^W + \vec{J}_d$), turning a divergence free. Here, these currents are given by following expressions:

$$\vec{J}^W = \sigma_P(\vec{W} \times \vec{B}_o) + \sigma_H(\vec{W} \times \vec{B}_o) \times \hat{b} \approx \sigma_H(\vec{W} \times \vec{B}_o) \times \hat{b} \tag{4.1}$$

$$\vec{J}_d = \sigma_P \vec{E}_d + \sigma_H(\vec{E}_d \times \hat{b}) \approx \sigma_H(\vec{E}_d \times \hat{b}) \tag{4.2}$$

$$\nabla \cdot \vec{J} = \nabla \cdot (\vec{J}^W + \vec{J}_d) = 0 \tag{4.3}$$

$$\nabla \cdot \sigma_H(\vec{E}_d + \vec{W} \times \vec{B}_o) \times \hat{b} = 0 \Rightarrow \nabla \cdot [\sigma_H(\vec{E} \times \hat{b})] = 0 \tag{4.4}$$

where

$$\vec{E} = \vec{E}_d + \vec{W} \times \vec{B}_o \tag{4.5}$$

$$\sigma_H \vec{E} \cdot (\nabla \times \hat{b}) = \hat{b} \cdot \nabla \times (\sigma_H \vec{E}) \tag{4.6}$$

In the steady state, $\nabla \times \vec{B}_o = \mu_o \vec{J} = \mu_o \sigma_H \vec{E} \times \hat{b}$, and therefore, we have following dynamo equation:

$$0 = \hat{b} \cdot \nabla \times (\sigma_H \vec{E}) \tag{4.7}$$

Since density or σ_H variation is mainly in vertical (p) direction, this dynamo equation

can be written as follows:

$$\vec{E}_\varphi = 0 \Rightarrow \vec{E}_d = -(\vec{W} \times \vec{B}_o)_\varphi \qquad (4.8)$$

Therefore, a steady state E region dynamo generates the zonal electric field arising from the vertical tidal wind component.

This zonal electric field is global in nature owing to the global nature of tidal wind and is responsible for transport of ionospheric plasma. In the vicinity of the equatorial E region, it gives rise to a robust dynamics referred to as electrojet. The mechanism for the eletrojet formation is as follows (KELLEY, 1989): In the slab geometry in Figure 4.1, the E region is considered as a conducting thin plate with the non-conducting vertical boundaries.
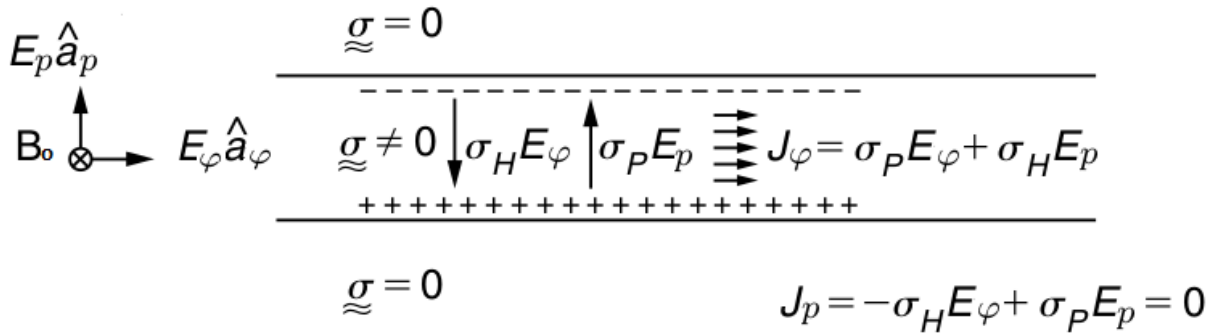
Figure 4.1 - The enhancement of equatorial current in a slab geometry.
Source: Adapted from Kelley (1989)

At the equatorial region, where the horizontal electric field $(\vec{E}_\varphi)$ is predominantly in the east-west direction and the geomagnetic field in the north-south, the electrons drift vertically with respect to ions. Since the E region dynamo is bound by relatively non-conducting regions, a vertical polarization field $(\vec{E}_p)$ is set up. This polarization field in turn sets up a Pedersen current of ions, so that at equilibrium, the vertical Hall current due to electrons is cancelled by the Pedersen current due to ions. This

gives:

$$\sigma_H E_\varphi = \sigma_P E_p \quad or, E_p = (\sigma_H/\sigma_P)E_\varphi \qquad (4.9)$$

The vertical polarization field E_p, is greater than E_φ by a factor of (σ_H/σ_P). This E_p, drives a Hall current $(\sigma_H E_p)$ in the east-west direction. The total horizontal current in the east-west direction is given by

$$
\begin{aligned}
J_\varphi &= \sigma_P E_\varphi + \sigma_H E_p, \\
&= [\sigma_P E_\varphi + \sigma_H (\sigma_H/\sigma_P)E_\varphi], \\
&= \left[\left(\frac{\sigma_H^2}{\sigma_P^2}\right) + 1\right]\sigma_P E_\varphi = \sigma_c E_\varphi
\end{aligned}
\qquad (4.10)
$$

Here σ_P is Pedersen conductivity (along the electric field), σ_H is Hall conductivity (perpendicular to both electric and magnetic fields) and E_φ is zonal electric field. The conductivity term appearing on the right hand side of Equation 4.10 is called Cowling conductivity. In the ionospheric E-region , Hall conductivity (σ_H) is about 3-4 times greater than the Pedersen conductivity. Thus, the direct conductivity in the east-west direction is intensified by σ_P to σ_c and the current is enhanced by $[(\frac{\sigma_H^2}{\sigma_P^2}) + 1]$. This enhanced current that flows in the altitude region of 100–110 km at around $\pm 3°$ of the dip equator is known as the Equatorial ElectroJet (EEJ) and is shown by the Figure 4.1. This intense current flowing in the east-west direction at the dip equator is responsible for the strong enhancement in the horizontal component of Earth's magnetic field (H) observed by the magnetometers over the equator. Effect of EEJ is clearly observed at in H component of dip equatorial stations as an increase of about 3-4 than those observed at off equatorial stations.

In the presence of intense current, the E region hosts varieties of ionospheric disturbances or field aligned irregularities (FAI) which are often observed from the coherent scatter radars. These disturbances are referred as Type I and Type II (KELLEY, 1989) which are caused by the modified two-stream (FARLEY, 1963; BUNEMAN, 1963) and gradient drift (ROGISTER; D'ANGELO, 1970) instabilities, respectively. Type I spectra have mean Doppler velocities close to the speed of ion acoustic waves $(\sim 360\ ms^{-1})$ and spectral widths much narrower than their mean Doppler velocities with higher amplitude. Type II spectra are characterized by a broader spectrum in relation to the Type I irregularities. They have low mean Doppler velocities (much smaller than ion acoustic speed).

Similar to the descending QP atmospheric disturbances as discussed in Chapter 3, night-time descending QP ionospheric disturbances are reported, mainly from

the radar observation over tropical latitudes covering equatorial to mid-latitude ionosphere (WOODMAN et al., 1991; PAN; TSUNODA, 1998; WOODMAN et al., 1999; CHOUDHARY; MAHAJAN, 1999; CHAU; WOODMAN, 1999; PATRA et al., 2002; RAO et al., 2008). In Figures 4.2– 4.4, radar observations of field-aligned ionospheric (FAI) disturbances are shown from these studies.

Figure 4.2 shows the altitude-time plots of SNR QP echoes observed between 2230 LT of October 31 and 0130 LT of November 1, 1998 at Piura low latitude radar. Presence of QP disturbances with descending nature in the upper E region is noted. These QP disturbances have periods between 5-15 minutes. They are confined to the 105-120 km region and the striation spacings short (between 3 and 10 km). In Figure 4.3 we can see the height-time SNR map of radar echoes observed on 6-7 October 2004 at low-latitude Gadanki radar during 2136-0500 LT. Note that data gap between 0000 and 0100 LT. This figure clearly shows three distinct echoing regions, occuring in the height ranges of 91-93 km, 96-100 km, and 101-116 km. The strongest echoing is in the middle region at around 96-100 km. The topmost echoing region shows the descending trend ($\sim 1\ ms^{-1}$). The QP structures can be clearly noticed above 96 km.

Figure 4.4 is the percentage of occurrence of the nighttime E-region FAI echoes during the 18:00 to 06:00 LT period. We can see that there are two regions with significant occurrence percentage. They are: one below the 105 km range and other between 105 to 120 km ranges. It shows that more than 90% of the upper region echoes are continuous type echoes without periodical features while less than 10% echoes present QP features. The observed QP echoes having spectral characteristics are similar to those observed by other radars (YAMAMOTO et al., 1991; PAN; TSUNODA, 1999). The lower region (below about 105 km range) echoes consist of QP. It has shown that 45 % of the observed echoes are characterized by QP features that correspond to the nighttime QP echoes (PAN; RAO, 2002).

Figure 4.5 shows the range time intensity (RTI) graph of coherent scatter echoes from electrojet irregularities received by the São Luís radar on 9 January 2002. This graph shows the signal-to-noise ratio (S/N in dB) of the radar echoes as a function of range (km) and UT. We can see that the radar echoes revealing QP oscillations of the electrojet echoing layer ($\sim$ 12:00 to 16:00 UT). The formation mechanism of this QP oscillations is yet to be known.
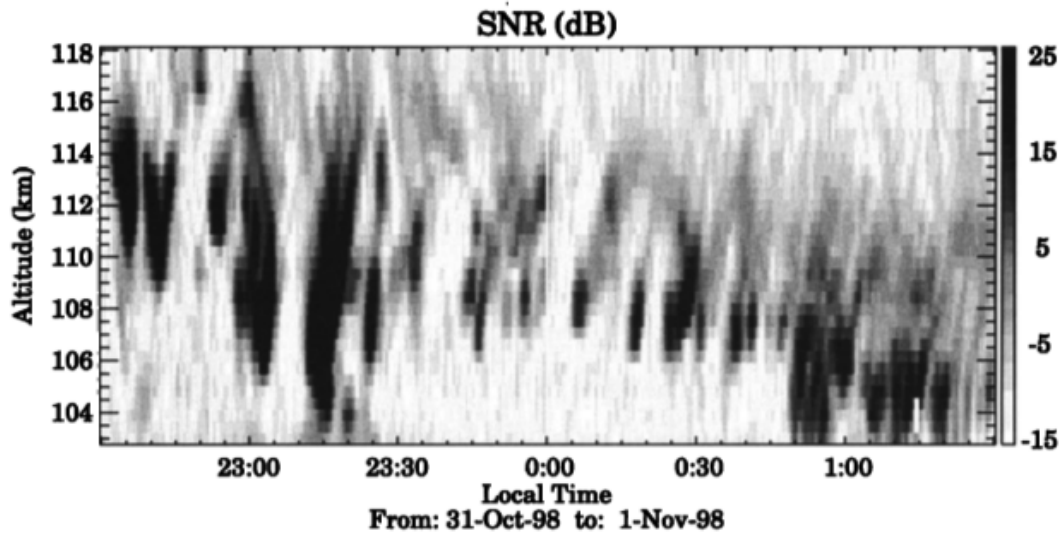
Figure 4.2 - FAI observed from Piura low latitude radar. Presence of QP disturbances with descending nature in the upper E region is noted. These QP disturbances have periods between 5-15 minutes.

Source: Adapted from Chau and Woodman (1999)
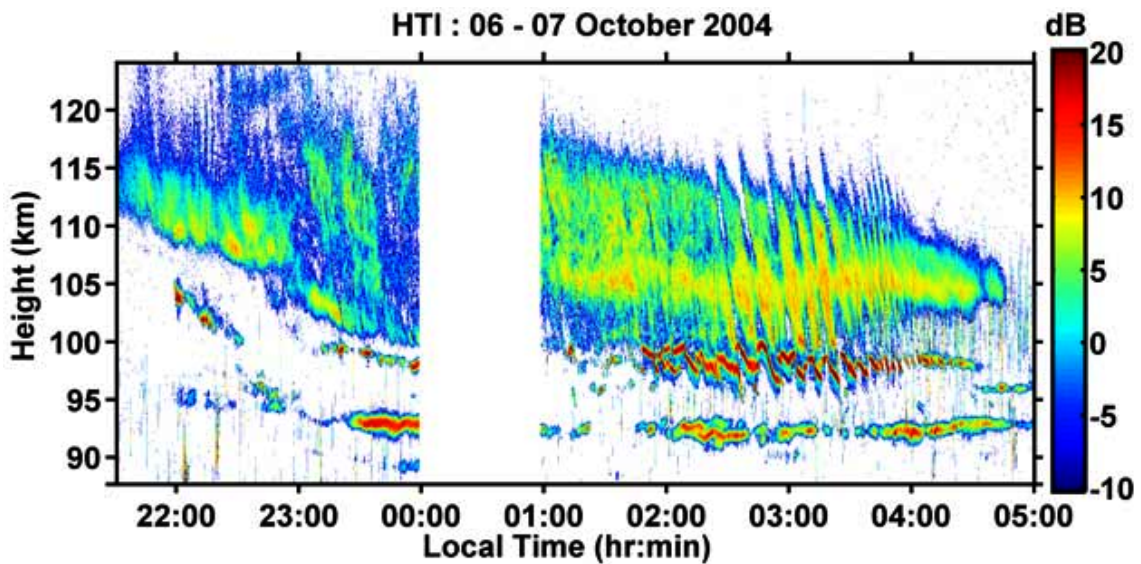
Figure 4.3 - FAI observed from Gadanki low latitude radar. Presence of QP disturbances with descending nature in the upper and low E regions are noted. These QP disturbances have periods between 2-15 minutes.

Source: Adapted from Rao et al. (2008)
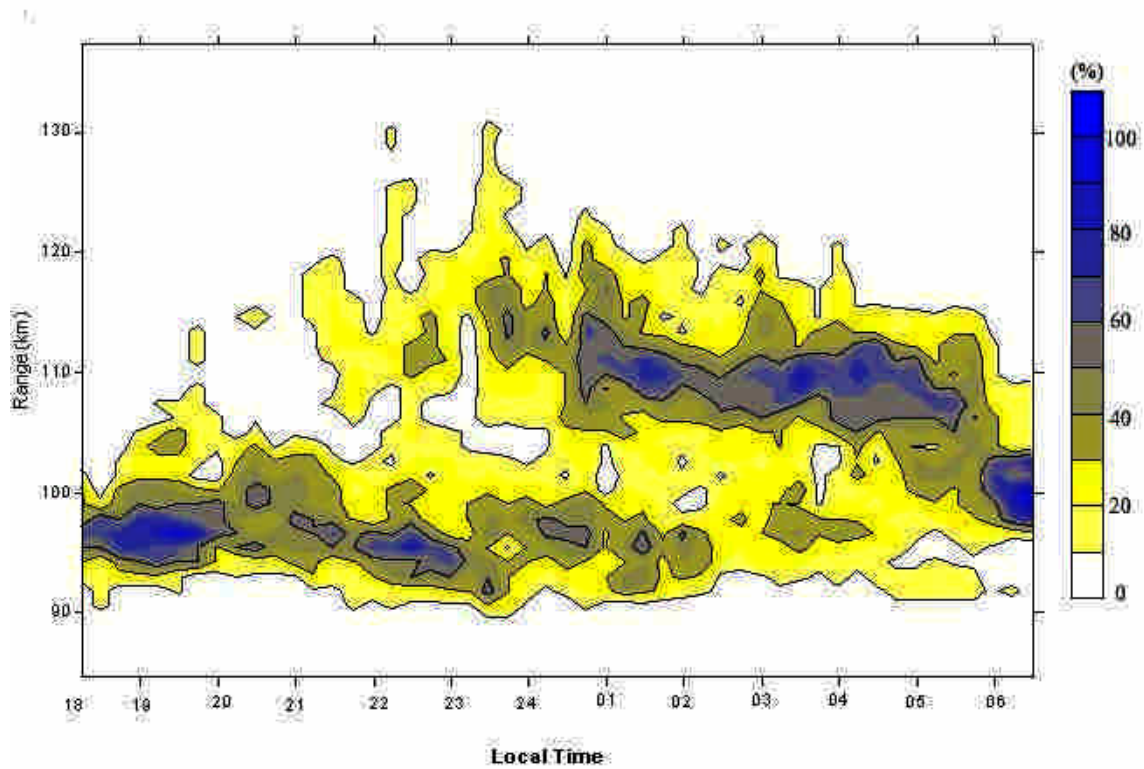
Figure 4.4 - QP FAI statistics from Gadanki low-latitude radar. Presence of descending layers with QP echoes within it are noted in both upper and lower E region. Source: Adapted from Pan and Rao (2004)
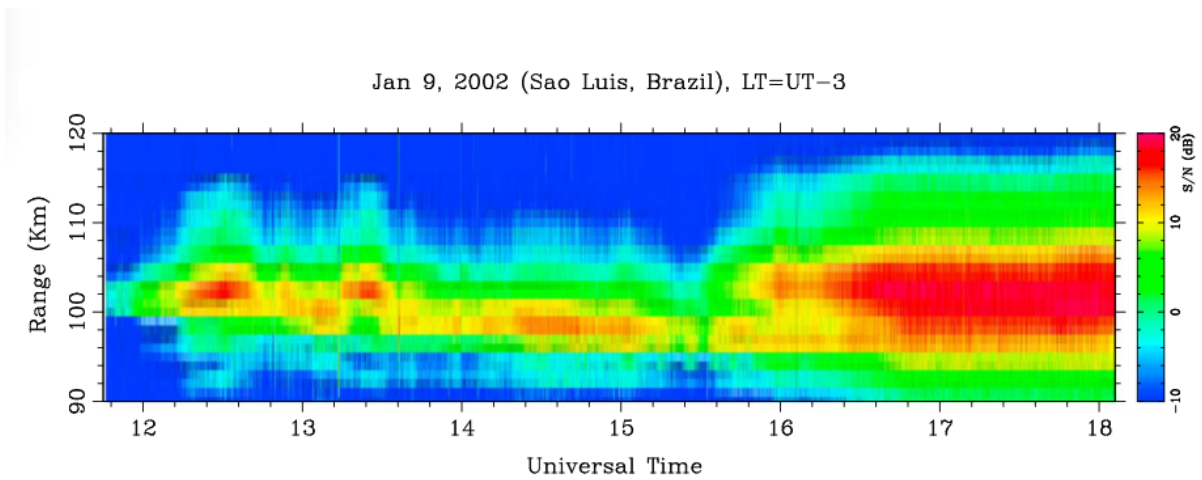
Figure 4.5 - Range time intensity (RTI) representation of coherent scatter from the equatorial electrojet irregularities received by the 30 MHz radar in São Luís on 9 January 2002.
Source: Adapted from Shume et al. (2014)

From these figures, we note the presence of descending layers of ionospheric disturbances in the upper and lower E regions. Moreover, within these layers, QP disturbances reside having periods in between 2–15 minutes and having their own descending characteristics which are different from the long term descending nature of the entire layer. Though the descending nature of these layers is owing to the tidal forcing as explained for the atmospheric disturbances, origin of these layer itself remains unresolved. Moreover, origin of QP disturbances and associated periods and descending nature remain unresolved. Also, the day-time QP disturbances in the presence of electrojet are reported (SHUME et al., 2014) as shown in Figure 4.5 and their formation mechanism is not well understood.

In this Chapter, we focus on a simulation study of day and night time QP ionospheric disturbances that will shed light on the underlying mechanism for the origin of these layers and QP disturbances. We note from Chapter 3 that the atmospheric disturbances caused by AGWs forcing in the MLT region, have characteristics similar to the aforementioned characteristics of the observed ionospheric disturbances. Therefore, a plausible mechanism for their origin can stem from the coupling between AGWs and ionosphere. In the next Section, we present a coupled simulation model of CI+AGWs and ionosphere, referred as AID model.

4.2   Coupled CI+AGWs+ionosphere simulation model or AID model

The coupled nonlinear 3D AID model includes the simulation of AGWs in the atmosphere using Navier-Stokes equations and the simulation of the hydromagnetic fluctuations in the ionosphere using a set of hydromagnetic equations (KHERANI et al., 2011; KHERANI et al., 2012).

The governing hydrodynamic equations for the AGWs in the atmosphere are presented in Chapter 3 and are written as follows:

$$\frac{\partial^2 \vec{W'}}{\partial t^2} = -\omega_{BCI}^2 \vec{W'} + \frac{1}{\rho}\nabla(\gamma p \nabla \cdot \vec{W'}) - \frac{\nabla p}{\rho^2}\nabla \cdot (\rho \vec{W'}) + \frac{1}{\rho}\nabla(\vec{W'} \cdot \nabla)p + \vec{E}_{visc} + \vec{E}_{nl} \quad (4.11)$$

$$\vec{W'} = \vec{W} + \vec{W}_o$$

$$\frac{\partial \rho}{\partial t} + \nabla \cdot (\rho \vec{W'}) = 0; \quad (4.12)$$

$$\frac{\partial p}{\partial t} + (\vec{W'} \cdot \nabla)p + \gamma p \nabla \cdot \vec{W'} = 0 \quad (4.13)$$

$$\omega_{BCI}^2 = \frac{\eta}{\rho}\nabla p \cdot \left[(\eta - 1)\frac{\nabla p}{p} + \frac{1}{T}\nabla T\right] \quad (4.14)$$

67

$$\vec{E}_{visc} = \frac{\partial}{\partial t}\left(\nu\nabla^2\vec{W}' + (\xi' + \frac{\nu}{3})\nabla(\nabla \cdot \vec{W}')\right) \tag{4.15}$$

$$\vec{E}_{nl} = -\frac{\partial}{\partial t}(\vec{W}' \cdot \nabla\vec{W}') \tag{4.16}$$

where $\vec{W}$ is the perturbation wind, $\vec{W}_o$ is the background wind. $p = R\rho T$ is the pressure, (ρ, T) are the atmospheric mass density and temperature, while (μ, ξ) are the dynamic first and second viscosities respectively. Here $(\nu = \mu/\rho, \xi' = \xi/\rho)$ are the first and second kinematic viscosities respectively. The term with ω_{BCI}^2 represents the non-adiabatic convective instability. $\vec{E}_{visc}$ and $\vec{E}_{nl}$ represent the viscous term and non linear saturation term, respectively.

A set of hydromagnetic equations in the ionosphere are written as follows (KHERANI et al., 2011; KHERANI et al., 2012):

$$\frac{\partial\vec{u_s}}{\partial t} = \frac{q_s}{m_s}(\vec{E} + \vec{u}_s \times \vec{B}) - \nu_s\vec{u}_s + \nu_s\vec{W}', \tag{4.17}$$

$$\frac{\partial n_s}{\partial t} + \nabla \cdot (n_s\vec{u_s}) = P - L, \tag{4.18}$$

$$\nabla^2\vec{E} - \nabla(\nabla \cdot \vec{E}) - \frac{1}{c^2}\frac{\partial^2\vec{E}}{\partial t^2} + \mu_o\frac{\partial\vec{J}}{\partial t} = 0, \tag{4.19}$$

$$\vec{J} = \underline{\sigma} \cdot \vec{E} + \vec{J}^W; \quad \vec{J}^W = e(n_i\vec{u}_i - n_e\vec{u}_e), \tag{4.20}$$

$$\nabla^2\vec{B} - \frac{1}{c^2}\frac{\partial^2\vec{B}}{\partial t^2} = -\mu_o\nabla \times \vec{J} \tag{4.21}$$

Here $(n_s, \vec{u_s})$ are the number density, velocity of plasma fluid 's' (s=ions(i)/electrons(e)), $(q_{i,e} = +Z_ie, -e)$, $(\vec{W}')$ is the velocity of AGWs from Equation 4.11, ν_s is the frequency of collision between ion/electron to neutral, $\vec{B}_o$ is the Earth's magnetic field and $\vec{J}^W$ is the ionospheric current density caused by the AGWs, $(\vec{E}, \vec{J}, \vec{B})$ in above equations are the electric field, net current and magnetic field perturbations in the ionosphere, $\underline{\sigma}$ is the ionospheric conductivity tensor and $(c = \frac{1}{\sqrt{\mu_o\epsilon_o}})$ is the speed of light in vacuum. P, L are the production and loss of ions and electrons by photoionization and chemical reactions. The production term 'P' in (4.18) is set to be zero for the night time condition. The chemical loss term, 'L', in (4.18) is retained through effective recombination rate as taken by Kherani et al. (2011). In addition to the wave Equation 4.19, $\vec{E}$ also satisfies the charge neutrality condition given by the following equation (KHERANI et al., 2012):

$$\nabla \cdot \vec{J} = 0 \text{ or } \nabla \cdot (\sigma \cdot \vec{E} + \vec{J}^W) = 0 \Rightarrow \nabla \cdot \vec{E} = -\sigma^{-1}(\vec{E} \cdot \nabla\sigma + \nabla \cdot \vec{J}^W) \tag{4.22}$$

Equations (4.17-4.22) form a closed set of equations to study the temporal and spatial variations of AGWs wind $\vec{W}'$, atmospheric density/pressure (ρ, p), ionospheric number density (n), electric field $\vec{E}$ and magnetic field $\vec{B}$ disturbances.

The simulation domain, boundary condition, numerical methods and ambient atmospheric conditions for AGWs are same as those described for the numerical experiment NE1 in Chapter 3. For the ionosphere, the simulation domain is same as for the atmosphere except that the altitude coverage is 70-300 km. Equations (4.17-4.22) are solved numerically employing the implicit Crank-Nicholson and SOR methods, as employed for the simulation of AGWs in Chapter 3. In Figure 4.6, the altitude variation of ambient ionospheric number density is shown.
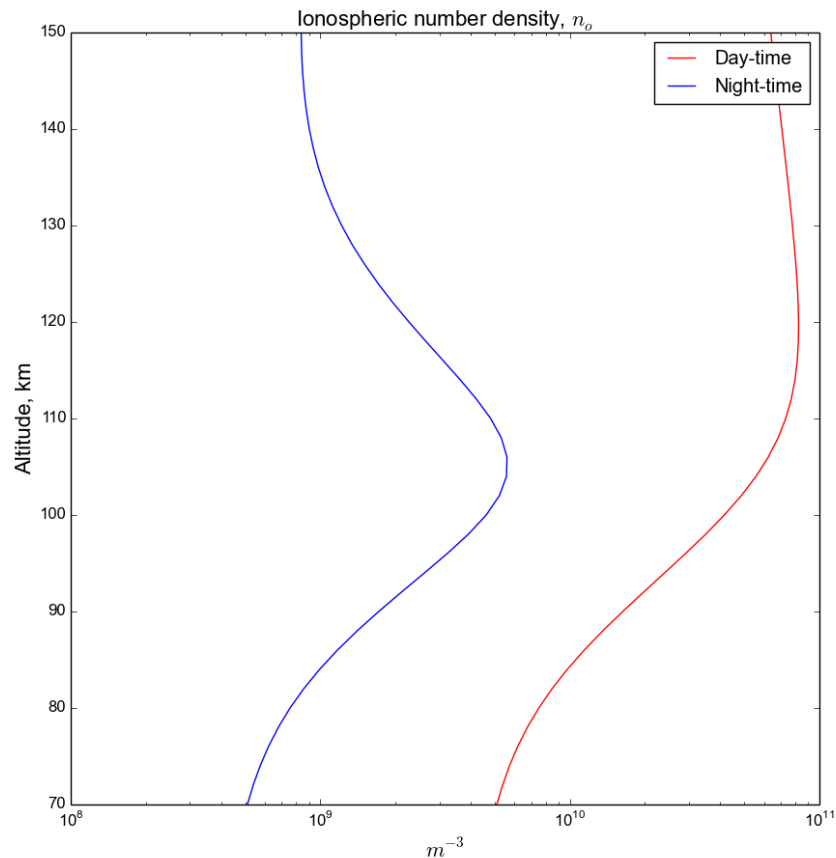
Figure 4.6 - Ionospheric electron density profile of day and night time during high solar flux in December.

4.3 Results and Discussion

In Figures 4.7-4.9, simulation results are shown wherein respectively the wind components (W_p, W_φ) of AGWs, degree of density change $\delta n = (n - n_o)/n_{\max}$ and the wind-driven ionospheric current components (J_p^W, J_φ^W) are plotted. Here wind and current components perpendicular to B_o are plotted since they are responsible for the ionospheric disturbances.
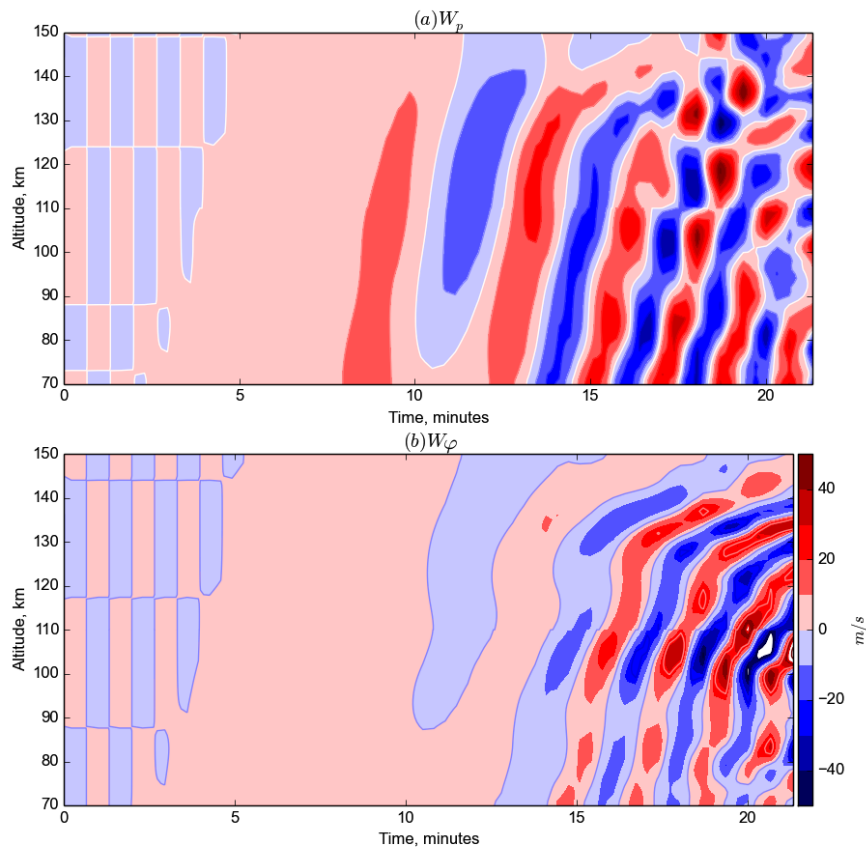
Figure 4.7 - Temporal-altitude variations of the simulated atmospheric disturbances (a) vertical wind component (W_p) of AGWs, (b) azimuth wind component (W_φ) of AGWs.
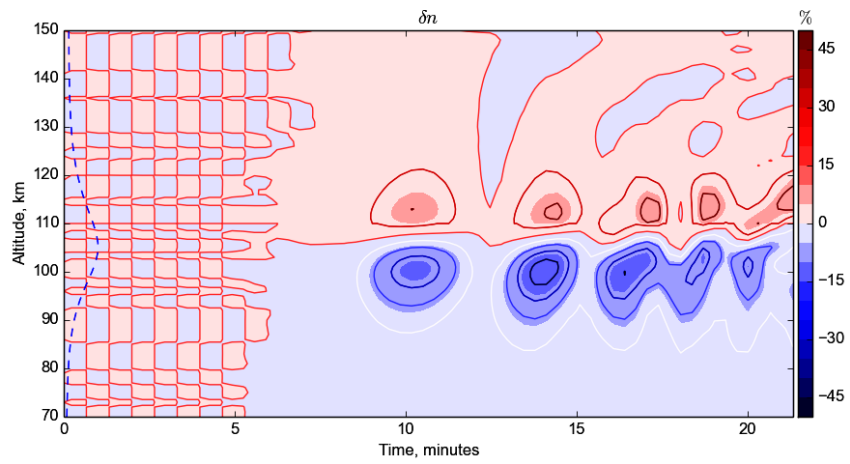
Figure 4.8 - Simulation results showing temporal-altitude distribution of the density fluctuations δn. The dashed-blue profile represents the initial density, normalized to the maximum density.
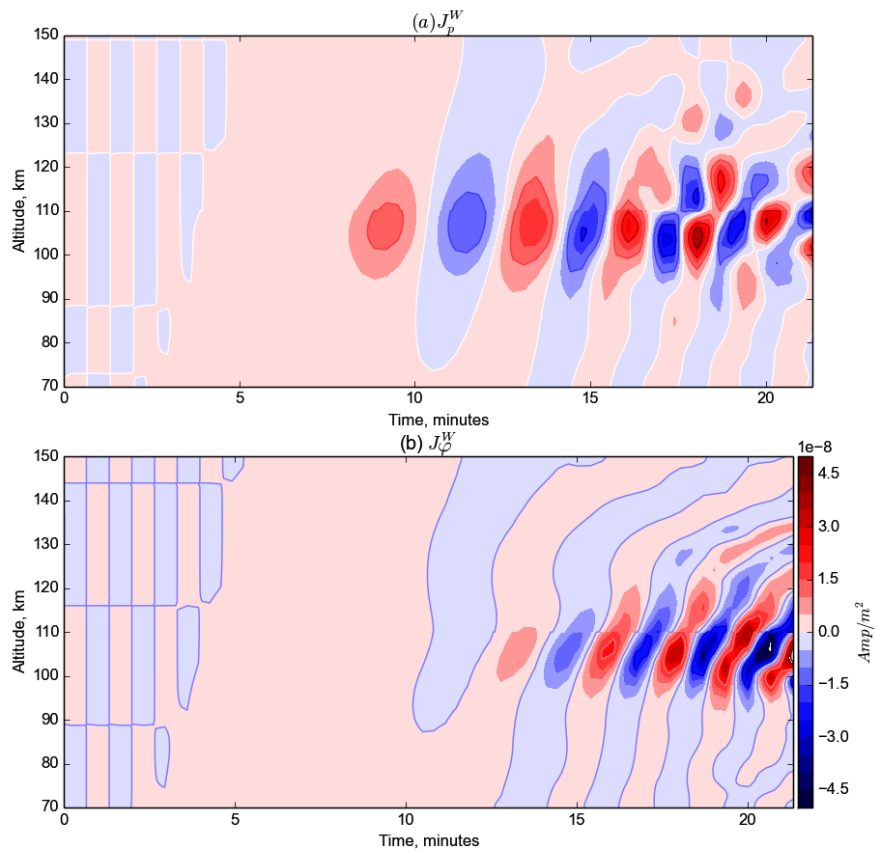
Figure 4.9 - Temporal-altitude variations of the current density (a) vertical current density component (J_p^W), (b) azimuth current density component (J_φ^W).

From these figures, we note the presence of descending layers of δn and J^W such that these layers host periodic disturbances within it. These periodic disturbances are present in both upper and lower E regions. Moreover, they have periods varying between 2-5 minutes. In δn disturbance, these periodic disturbances appear as QP disturbances. The irregular structures appear in the Earth's ionosphere are believed to be generated by collisional interchange instability (CII) which is the general terminology for gradient-drift, $E \times B$, and Rayleigh-Taylor instability mechanisms (KHERANI et al., 2005). In order to interpret observations of ionospheric irregularities as shown in Figures 4.2-4.4, simulation of CII is required. However, in the present work, we do not simulate CII but rather we simulate the linear growth rate (γ) of CII which is given by the following expression (KHERANI et al., 2005):

$$\gamma = \frac{1}{en}\left(J_p^W \frac{\partial \log n}{\partial \varphi} + J_\varphi^W \frac{\partial \log n}{\partial p} \right) \tag{4.23}$$

In the upper panel of Figure 4.10, we present the simulated growth rate (γ). In the lower panel, we plot γ-$2\alpha n$ where $2\alpha n$ is the recombination rate representing the decay or damping rate of CII.
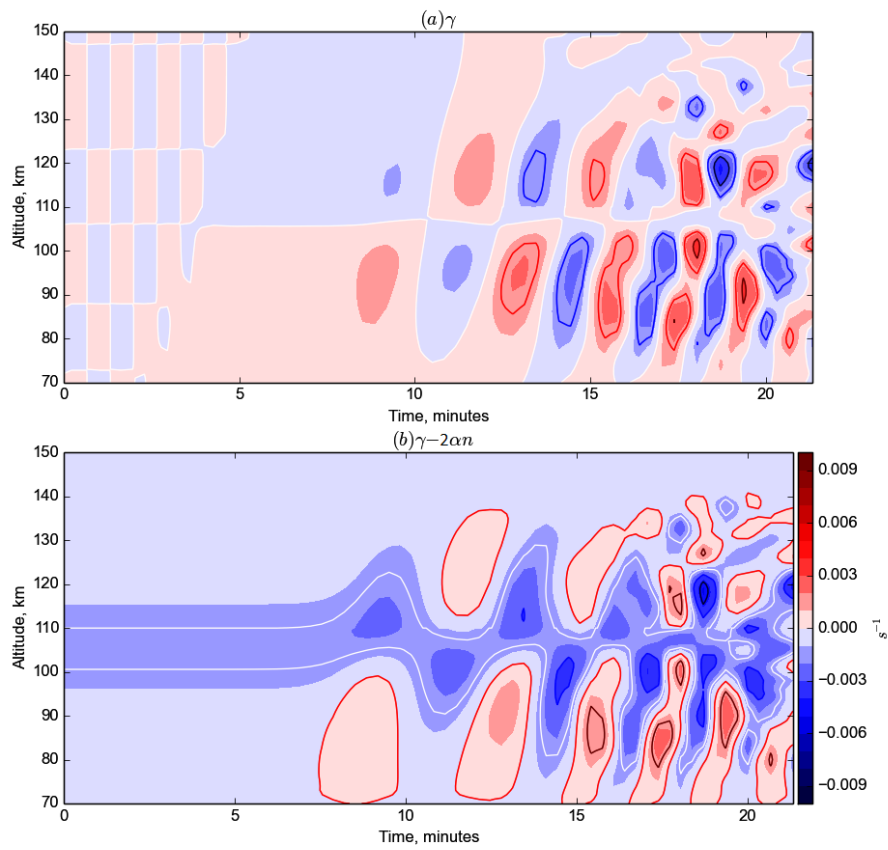
Figure 4.10 - (a) Simulated growth rate given by Equation 4.23 is plotted. (b) Plot showing the γ-$2\alpha n$ where $2\alpha n$ is the recombination rate representing the decay or damping rate of CII.

From this figure, we note the presence of periodic disturbance in γ-$2\alpha n$ both in the lower and upper E region. Regions of large positive values of γ-$2\alpha n$ represent the regions of positive growth of CII and therefore they are the regions that host ionospheric irregularities. It is evident that owing to the presence of a negative γ-$2\alpha n$ region in between two positive γ-$2\alpha n$ regions, the irregularities acquire QP nature. Moreover, this QP trend is embedded in the descending layers occupying both upper and lower E regions. Therefore, on the basis of γ-$2\alpha n$ in Figure 4.10, observations of QP and descending disturbances in Figures 4.2-4.4 can be interpreted.

4.4 QP disturbances in the electrojet

Using Brazilian São Luís radar, Shume et al. (2014) have reported the presence of QP disturbances in the electrojet, as shown in Figure 4.5.

They proposed it to be owing to the AGWs of tropospheric origin though no theoretical analysis or simulation was presented. With simulation tools developed in this Chapter, we can study such disturbances in the present work. To do so, we perform simulation under daytime ionospheric conditions. The normal electrojet current, which is in the φ direction, is assumed to be of following form:

$$J_o = 10^{-6} e^{(-(r-105)^2/5^2)} A/m^2$$

In Figure 4.11, we present simulation results wherein electrojet current (J_o), AGWs driven ionospheric current (J_φ^W) and total current ($J_o + J_\varphi^W$) are shown. We note the periodic disturbances in J_φ^W having amplitude sufficient enough to alter the background J_o, leading to the periodic disturbances in the resultant current. Therefore, the resultant current acquires regions electrojet and counter electrojet current structure such that regions of electrojet current host electrojet or Type I instability while regions of counter electrojet damp this instability. As a result, QP disturbances in the electrojet arise, explaining the observation in Figure 4.5.
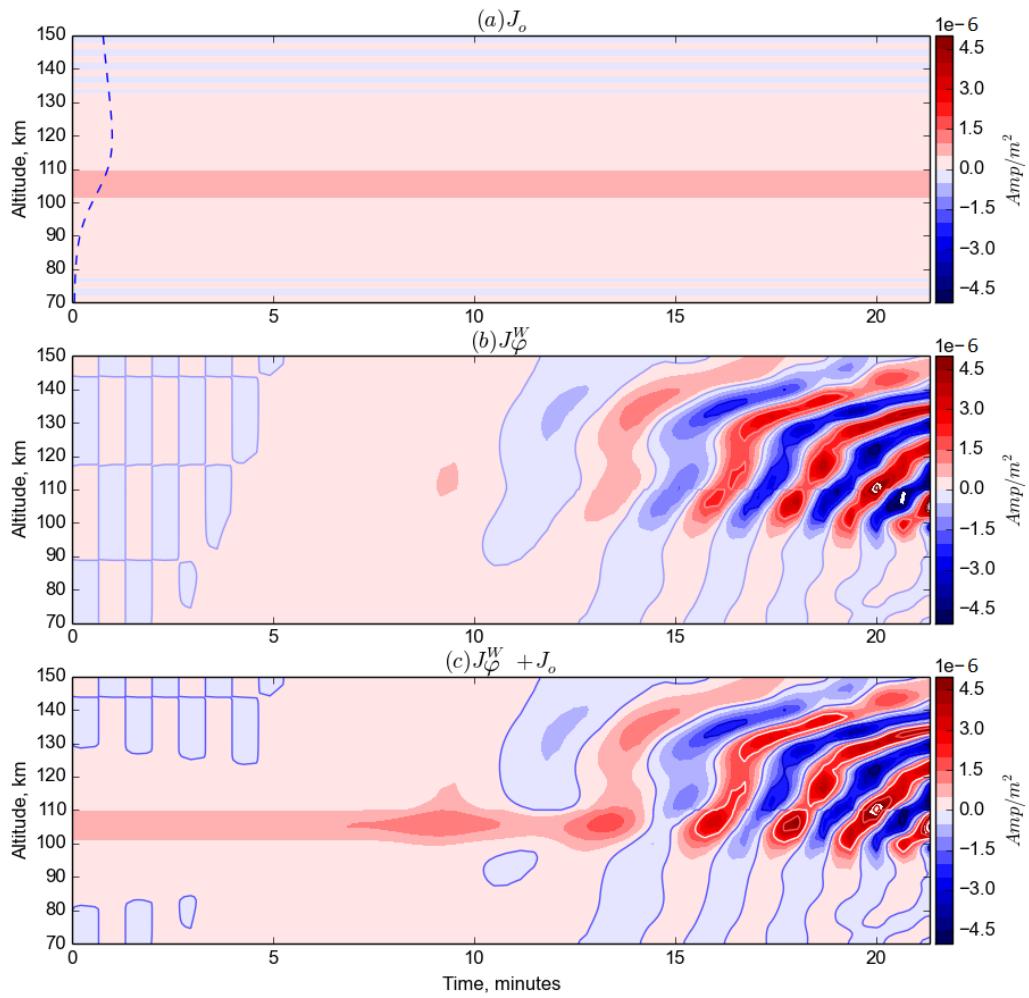
Figure 4.11 - Simulated temporal-altitude results (a) electrojet current (J_o), the dashed-blue profile represents the initial density, normalized to the maximum density, (b) AGWs driven ionospheric current (J_φ^W), and (c) sum of electrojet current and AGWs driven ionospheric current i.e., $(J_o + J_\varphi^W)$.

4.5 Summary

In this Chapter, we have presented the 3D simulation study of ionospheric disturbances which is excited due to AGWs. The novel results are presented and compared with the observations. We have shown that the wind components (W_p, W_φ) of AGWs, degree of density change $\delta n = (n - n_o)/n_{\max}$ and the wind-driven ionospheric current components (J_p^W, J_φ^W) descending QP disturbances. We note the presence of descending layers of δn and J^W such that these layers host periodic disturbances within it. These periodic disturbances are present in both upper and lower E regions. Moreover, they have periods varying between 2–5 minutes. In δn disturbance, these periodic disturbances appear as QP disturbances. We note the presence of periodic disturbance in γ-$2\alpha n$ in both lower and upper E region. Regions of large positive values of γ-$2\alpha n$ are the regions of positive growth of CII and therefore they are the regions that host ionospheric irregularities. It is evident that owing to the presence of a negative γ-$2\alpha n$ region in between two positive γ-$2\alpha n$ regions, the irregularities acquire QP nature. Moreover, these QP trend is embedded in the descending layers occupying both upper and lower E regions.

We also showed the numerical experiments about electrojet current, AGWs driven ionospheric current and total current under daytime ionospheric conditions. We note the periodic disturbances in J_φ^W having amplitude sufficient to change the background current J_o, leading to the periodic disturbances in the resultant current. This resultant current shows the regions of electrojet and counter elctrojet current structure. These simulated results were compared with the range time intensity (RTI) representation of coherent scatter from the equatorial electrojet irregularities received by the 30 MHz radar in São Luís, Brazil.

5 SUMMARY AND FUTURE DIRECTIONS

5.1 Summary

The Mesosphere-Lower-Thermosphere (MLT) region hosts different types of atmospheric-ionospheric disturbances during convective climate, high and low solar flux, seasons, etc. In this thesis we have studied the atmospheric-ionospheric disturbances in the MLT region during convective climate. The developed integrated model showed the self-consistent dynamical coupling mechanism between the troposphere to the MLT region. In this Chapter we summarize the results that constitute the main part of this thesis.

In Chapter 2, the developed theoretical model of non-adiabatic convective instability (CI) in the dry atmosphere to understand the lapse rate variation in the lower troposphere. The simulated lapse rate variation with altitude is compared with the previously observed variation in the lower troposphere and fairly good agreement is found between them. In particular, the observed depression in the lapse rate between 2–5 km altitude is noted in the simulated variation which was not explained previously. Therefore, the non-adiabatic contributions to the CI in the lower dry troposphere offer an alternative interpretation to the observations.

In Chapter 3, the developed simulation model of CI+ AGWs is described and several numerical experiments are performed to simulate the OH airglow ripples oblique and parallel to the bands and QP descending disturbances in the Na density. By considering the wave-like-Gaussian forcing at the ground, two numerical experiments, NE1 and NE2 were presented in which the wind divergence is, respectively, retained and omitted. From NE1, the formation of ripples oblique to the bands are noted. A novel outcome is the formation of strong highly localized ripples of scale size ~ 5 km in the regions of large horizontal wind divergence. Another novel outcome is that the ripples ceased to exist in NE2, indicating the important role of wind divergence to generate them. In another numerical experiment NE3 smilar to the NE1 but with the Gaussian forcing, the presence of ripples parallel to the bands are noted. These bands and parallel ripples are arising from the interaction between Gaussian forcing and drifting background in which circular wavefronts generated by AGWs in the amosphere acquires both band and ripple structures. The Na density disturbances in the MLT region corresponding to NE1 is presented and it reveals the presence of descending QP disturbances with periods between $\sim 3 - 5$ minutes.

In Chapter 4, the ionospheric disturbances arising from the CI+AGW forcing were

studied using for the numerical experiment NE1, to understand the night-time and day-time QP ionospheric disturbances. The growth rate of CII is found to have QP nature suggesting the growth of QP ionospheric disturbances in the MLT region during night-time. These QP trend is embedded in the descending layers occupying both upper and lower E regions. Also, the day-time eletrojet is found to acquire QP nature owing to the strong CI+AGW forcing revealing alternative electrojet-counterelectrojet disturbances.

5.2   Future Directions

Earth's atmosphere sustains neutral waves arising from various kind of forcing such as tropospheric convection, topographic wind convergence and mechanical ground forcing from earthquakes/tsunamis. These waves, generally in the form of Acoustic-Gravity waves (AGWs), are amplified by 3–4 orders in magnitude as they propagate across the Mesosphere-Lower-Thermosphere (MLT) region and towards the thermosphere. In the MLT and thermosphere, they couple with the ionosphere and excite the Atmospheric-Ionospheric Disturbances (AIDs). We refer this phenomena (i) as convective weather when the forcing is of convective origin, and (ii) seismic weather when the forcing is of seismic origin. During the covective and seismic weathers, varieties of AIDs in the MLT and upper thermosphere regions are observed. Among them, airglow disturbances in the MLT and thermosphere, electrojet disturbances in the E region, TIDs in the ionosphere are important kinds of AIDs. While these TIDs are studied extensively unfolding their diverse nature and associated dynamics, many aspects remain unexplored. In particular, these aspects remain to be understood theoretically. Moreover, their diverse nature demands development of an integrated framework where observations can be complemented with the simulation. The results reported in this thesis have underlined some promising areas and raised the numerous issues for future research. The following are some proposals in the future works:

1) In the ongoing development of simulation model for the AIDs which will be subsequently employed to interpret observed AIDs. The developed simulation model of AGWs in this thesis arising from the covective and topographic wind forcing incorporates the Non-Boussinesq convective instability (CI). Moreover, the model is also coupled with the ionospheric model to study the AIDs in the MLT region. This coupled CI+AGWs ionospheric model will be further upgraded and employed to simulate the electrojet disturbances and TIDs in the ionosphere, during convective weathers. The

convective forcing for numerical observations will be specified from the meteorological observations.

2) We aim to focus on dynamical aspects, such as the counter electrojet disturbances, magnetic disturbances in the F region, airglow disturbances, MSTIDs and SSTIDs in the F region. Moreover, we aim to analise the data from the all-sky observations, magnetic field and satellite observations.

3) We also aim to study AIDs during seismic weathers, mainly during tsunamis, such as Sumatra, Chile and Japan tsunamis. Aforementioned CI+AGWs ionospheric model can be employed for this study by changing the nature of forcing. We aim to focus on aspects such as the simulation of AIDs and magnetic field or current in the E region during tsunamis, which remained unexplored till date.

REFERENCES

ANGSTROM, A. J. Recherches sur le spectre solaire. **W. Schultz, Upsalla**, p. 41–42, 1868. 10

APPLETON, E. V.; BARNETT, M. A. F. Local reflection of wireless waves from the upper atmosphere. **Nature**, v. 15, p. 333–334, 1925. 14

_____. On some direct evidence for downward atmospheric reflection of electric rays. **Proceedings of the Royal Society of London**, A109, p. 621–641, 1925. 14

BAKER, W.; MARTYN, D. F. Electric currents in the ionosphere. i. conductivity. **Philosophical Transactions of the Royal Society of London**, v. 246, n. 913, p. 281–294, 1953. 61

BARTH, C. A. Three body reactions. **Annales Geophysicae**, v. 20, p. 182–190, 1964. 12, 13

BATES, D. R.; MOISEIWITSCH, B. L. Origin of the Meinel hydroxyl system in the night airglow. **Journal of Atmospheric and Solar-Terrestrial Physics**, v. 8, p. 305–308, 1956. 11, 12

BATES, D. R.; NICOLET, M. Atmospheric hydrogen. **Planetary and Space Science**, v. 13, p. 905–909, 1950. 11

BRASSEUR, G. P.; SOLOMON, S. **Aeronomy of the middle atmosphere chemistry and physics of the stratosphere and mesosphere**. [S.l.]: Dordrecht: Springer, 2005. 651 p. 1, 14, 17

BREIT, G.; TUVE, M. A. A radio method of estimating the height of the conducting layer. **Nature**, v. 116, p. 357, 1925. 14

BROADFOOT, A. L.; KENDALL, K. R. The airglow spectrum 3100-10000 Å. **Journal of Geophysical Research**, v. 73(1), p. 426–428, 1968. 11

BUNEMAN, O. Excitation of field aligned sound waves by electron streams. **Physical Review Letters**, v. 10, n. 7, p. 285–287, 1963. 63

CHAMBERLAIN, J. W. **Physics of the aurora and airglow**. New York: Academic Press, 1961. 704 p. (International Geophysics Series, v. 2). 9

CHAPMAN, S. Bakerian lecture. some phenomena of the upper atmosphere. **Proceedings of Royal Society of London**, A132, p. 353–374, 1931. 12

_____. Notes on atmospheric sodium. **Astrophysical Journal**, v. 90, p. 309–316, 1939. 12, 13

_____. The electrical conductivity of the ionosphere: A review. **Nuovo Cimento**, v. 4(10), (Suppl.4), p. 1385–1412, 1956. 61

CHAU, J. L.; WOODMAN, R. F. Low-latitude quasiperiodic echoes observed with the Piura VHF radar in the E region. **Geophysical Research Letters**, v. 26, n. 14, p. 2167–2170, 1999. 64, 65

CHOUDHARY, R. K.; MAHAJAN, K. K. Tropical E region field aligned irregularities: Simultaneous observations of continuous and quasiperiodic echoes. **Journal of Geophysical Research**, v. 104, n. A2, p. 2613–2619, 1999. 64

CLEMESHA, B.; SIMONICH, D.; BATISTA, P. Mesopause region temperature structure observed by sodium resonance lidar. **Journal of Atmospheric and Solar-Terrestrial Physics**, v. 72, p. 740–744, 2010. 53, 56

_____. Sodium lidar measurements of mesopause region temperature at 23 °S. **Advance in Space Research**, v. 47, p. 1165–1171, 2011. 33, 37, 53

CLEMESHA, B. R. Sporadic neutral metal layers in the mesosphere and lower thermosphere. **Journal of Atmospheric and Solar-Terrestrial Physics**, v. 57, p. 725–736, 1995. 13

CLEMESHA, B. R.; BATISTA, P. P.; SIMONICH, D. M.; BATISTA, I. S. Sporadic structures in the atmospheric sodium layer. **Journal of Geophysical Research**, v. 109, p. D11306, 2004. 33, 35, 53

FAGUNDES, P. R.; SAHAI, Y.; TAKAHASHI, H. Investigation of OI 557.7 nm and OI 630.0 nm nightglow intensity ratios during the occurrences of equatorial F-region plasma bubbles. **Journal of Atmospheric and Solar-Terrestrial Physics**, v. 16, n. 5, p. (5)27–(5)30, 1995. 10

FARLEY, D. T. A plasma instability resulting in field aligned irregularities in the ionosphere. **Journal of Geophysical Research**, v. 68, n. A22, p. 6083–6097, 1963. 63

FOLKINS, I. Convective damping of buoyancy anomalies and its effect on lapse rates in the tropical lower troposphere. **Atmospheric Chemistry and Physics**, v. 6, p. 1–12, 2006. 24, 25, 29

FOLKINS, I.; MARTIN, R. V. The vertical structure of tropical convection, and its impact on the budgets of water vapor and ozone. **Journal of Atmospheric Sciences**, v. 62, p. 1560–1573, 2005. 25

FRITTS, D. C.; ALEXANDER, M. J. Gravity wave dynamics and effects in the middle atmosphere. **Review of Geophysics**, v. 41(1), p. 1003, 2003. 1, 5

FRITTS, D. C.; ISLER, J. R.; HECHT, J. H.; WALTERSCHEID, R. L.; ANDREASSEN, O. Wave breaking signatures in sodium densities and OH nightglow: 2. simulation of wave and instability structures. **Journal of Geophysical Research**, 1997. 33, 50

FRITTS, D. C.; RASTOGI, P. K. Convective and dynamical instabilities due to gravity wave motions in the lower and middle atmosphere: Theory and observations. **Radio Science**, 1985. 33

FRITTS, D. C.; YUAN, L. Stability analysis of inertio-gravity wave structure in the middle atmosphere. **Journal of Atmospheric Sciences**, 1989. 50

HALDOUPIS. A tutorial review on sporadic E layers. In: ABDU, M. A.; PANCHEVA, D. (Ed.). **Aeronomy of the Earth's Atmosphere and Ionosphere**. [S.l.: s.n.], 2011. cap. 29, p. 381–394. 48

HARGREAVES, J. K. **The solar-terrestrial environment: An introduction to geospace - the science of the terrestrial upper atmosphere, ionosphere, and magnetosphere**. Cambridge, UK: Cambridge University Press, 1992. 8

HECHT, J. H. Instability layers and airglow imaging. **Review of Geophysics**, v. 42 RG1001, 2004. 10, 33, 34, 35, 48, 51

HECHT, J. H.; LIU, A. Z.; WALTERSCHEID, R. L.; FRITTS, D. C.; ISLER, J. R.; SNEFT, D. C.; GARDNER, C. S.; FRANKE, S. J. Wave breaking signatures in OH airglow and sodium densities and temperature: 1. airglow imaging, Na lidar, and MF radar observations. **Journal of Geophysical Research**, 1997. 33

HECHT, J. H.; LIU, A. Z.; WALTERSCHEID, R. L.; FRANKE, S. J.; RUDY, R. J.; J.TAYLOR, M.; PAUTET, P. Characteristics of short-period wavelike

features near 87 km altitude from airglow and lidar observations over Maui.
Journal of Geophysical Research, 2007. 33, 34

HEELIS, R. A. Electrodynamics in the low and middle latitude ionosphere: a
tutorial. **Journal of Atmospheric and Solar-Terrestrial Physics**, v. 66, p.
825–838, 2004. 20

HEELIS, R. A.; KENDALL, P. C.; MOFFELT, R. J.; WINDLE, D. W.;
RISHBETH, H. Electrical coupling of the E and F-regions and its effects on
F-region drifts and winds. **Planetary and Space Science**, v. 22, p. 743–756,
1974. 61

HICKEY, M. P.; TAYLOR, M. J.; GARDNER, C. S.; GIBBONS, C. R. Full-wave
modeling of small-scale gravity waves using airborne lidar and observations of the
Hawaiian airglow (ALOHA-93) (O^S) images and coincident Na wind/temperature
lidar measurements. **Journal of Geophysical Research**, v. 103, n. D6, p.
6439–6453, March 1998. 8

HINES, C. O. Internal atmospheric gravity waves at ionospheric heights.
Canadian Journal of Physics, v. 38, p. 1441–1481, 1960. 5, 8

HORINOUCHI, T.; NAKAMURA, T.; KOSAKA, J. Convectively generated
mesoscale gravity waves simulated throughout the middle atmosphere.
Geophysical Research Letters, v. 29, n. 21, 2002. 33, 34, 48

HUBA, J. D.; JOYCE, G.; FEDDER, J. A. SAMI2 is another model of the
ionosphmodel (SAMI2): A new low-latitude ionosphere model. **Journal of
Geophysical Research**, v. 105, n. A10, p. 23,035–23,05, 2000. 39, 107, 109

HUNSUCKER, R. D.; HARGREAVES, J. K. **The high-latitude ionosphere
and its effects on radio propagation**. Cambridge: Cambridge University Press,
2003. 5, 7

KANE, T.; GRIME, G.; KUDEKI, S. F. F.; URBINA, J.; KELLEY, M.;
COLLINS, S. Joint observations of sodium enhancements and field-aligned
ionospheric irregularities. **Geophysical Research Letters**, v. 28, n. 7, p.
1375–1378, 2001. 33, 35, 53

KELLEY, M. C. **The Earth's Ionosphere: plasma physics and
electrodynamics**. San Diego, California: Academic Press, 1989. 4, 19, 62, 63

KENDALL, P. Geomagnetic control of diffusion in the F2-region of the ionosphere –i the form of the diffusion operator. **Journal of Atmospheric and Terrestrial Physics**, v. 24, n. 9, p. 805–811, 1962. 107

KHERANI, A. E.; MASCARENHAS, M.; PAULA, E. R. de; SOBRAL, J. H. A.; BERTONI, F. A three-dimensional simulation of collisional-interchage-instability in the equatorial-low-latitude ionosphere. **Space Science Reviews**, v. 121, p. 253–269, 2005. 39, 72

KHERANI, E. A.; ABDU, M. A.; FRITTS, D. C.; PAULA, E. R. de. The acoustic gravity wave induced disturbances in the equatorial ionosphere. In: ABDU, M. A.; PANCHEVA, D. (Ed.). **Aeronomy of the Earth's Atmosphere and Ionosphere**. [S.l.: s.n.], 2011. cap. 10, p. 141–162. 8, 26, 39, 56, 67, 68, 93

KHERANI, E. A.; LOGNONNE, P.; HEBERT, H.; ROLLAND, L.; ASTAFYEVA, E.; OCCHIPINTI, G.; COISSON, P.; WALWER, D.; PAULA, E. R. de. Modelling of the total electronic content and magnetic field anomalies generated by the 2011 Tohoku-oki tsunami and associtated acoustic-gravity waves. **Geophysical Journal International**, v. 191, p. 1049–1066, 2012. ix, xi, 5, 6, 26, 39, 67, 68, 93

KIRCHHOFF, V. W. J. H. **Introdução á geofísica espacial**. São Paulo: FAPESP, 1991. 106

KRASSOVSKY, V. I. The nature of emissions of the upper atmosphere. **Annales Geophysicae**, v. 27, p. 211, 1971. 12

LANDAU, L. D.; LIFCHITZ, E. M. **Fluid Mechanics: volume 6 of course of theoretical physics**. Oxford: Butterworth-Heinemann, 1987. 5

LANGHOFF, S. R.; WERNER, H. J.; ROSMUS, P. Theorical transitions probabilities for the OH Meinel system. **Journal of Molecular Spectroscopy**, v. 188(2), p. 507–529, 1986. 38

LI, F.; LIU, A. Z.; SWENSON, G. R.; HECHT, J. H.; ROBINSON, W. A. Observations of gravity wave breakdown into ripples associated with dynamical instabilities. **Journal of Geophysical Research**, 2005. 33

LILLY, D. K. A comparison of incompressible, anelastic and Boussinesq dynamics. **Atmospheric Research**, v. 40, p. 143–151, 1996. 25

LUCAS, C.; ZIPSER, E. J.; LEMONE, M. A. Vertical velocity in oceanic convection off tropical Australia. **Journal of Atmospheric Sciences**, v. 51, p. 3183–3193, 1994. 30

MAHRT, L. On the shallow motion approximations. **Journal of Atmospheric Sciences**, v. 43, p. 1036–1044, 1986. 4, 94

MAKHLOUF, U. B.; PICARD, R. H.; WINICK, J. R. Photochemical-dynamical modeling of the measured response of airglow to gravity waves 1. basic model for OH airglow. **Journal of Geophysical Research**, v. 100(D6), p. 11,289–11,311, 1995. 39

MAPES, B. E. Waterâs two scale heights: The moist adiabat and the radiative troposphere. **Quarterly Journal of Meteorological Society**, v. 127, p. 2353–2366, 2001. 25

MARKOWSKI, P. An overview of atmospheric convection. In: GIAIOTTI, D. B.; STEINACKER, R.; STEL, K. F. (Ed.). **Atmospheric convection:**. Udine: CISM International Centre for Mechanical Sciencesk, 2007. v. 475, p. 1–6. 4, 23, 25

MCDADE, I. C.; LLEWELLYN, E. J.; MURTAGH, D. P.; GREER, R. G. H. Eton 5: Simultaneous rocket measurements of the oh meinel $\delta V = 2$ sequence and (8,3) band emission profiles in the nightglow. **Planetary and Space Science**, v. 35, n. 9, p. 1137–1147, 1987. 39

MCLENNAN, J. C.; SHRUM, G. M. On the origin of the auroral green line 5577 Å, and other spectra associated with the aurora borealis. **Proceedings of the Royal Society of London. Series A, Containing Papers of a Mathematical and Physical Character**, v. 108, n. 747, p. 501–512, 1925. 12

MEDEIROS, A. F.; TAKAHASHI, H.; BURITI, R. A.; FECHINE, J.; WRASSE, C. M.; GOBBI, D. MLT gravity wave climatology in the South America equatorial region observed by airglow imager. **Annales Geophysicae**, 2007. 33

MEINEL, A. B. *OH* emission bands in the spectrum of the night sky. **Astrophysical Journal**, v. 111, p. 555–564, 1950. 11

MERIWETHER, J. H.; GARDNER, G. A review of the mesospheric inversion layer phenomenon. **Journal of Geophysical Research**, v. 12, p. 405–416, 2000. 3

MIES, F. H. Calculated vibrational transitions probabilities of oh ($X^2\pi$). **Journal of Molecular Spectroscopy**, v. 53, p. 150–188, 1974. 38

MOHANAKUMAR, K. **Stratosphere troposphere interaction**. [S.l.]: Springer, 2008. 3

MUKHERJEE, G. K. The signature of short-period gravity waves imaged in the OI 557.7 nm and near infrared OH nightglow emissions over Panhala. **Journal of Atmospheric and Solar-Terrestrial Physics**, v. 65, p. 1329–1335, 2003. 10, 33

NAKAMURA, T.; AONO, T.; TSUDA, T.; ADMIRANTO, A. G.; ACHMAD, E.; SURANTO. Mesospheric gravity waves over a tropical convective region observed by OH airglow imaging in Indonesia. **Geophysical Research Letters**, v. 30, n. 17, p. 1862, 2003. 33

NARAYANAN, V. L.; GURUBARAN, S.; EMPERUMAL, K. Airglow imaging observations of smallâscale structures driven by convective instability in the upper mesosphere over tirunelveli (8.7°N). **Journal of Geophysical Research**, v. 115, n. D19119, 2010. 33

NELSON, D. D.; SHIFFMAN, A.; NESBIT, D. J.; ORLANDO, J. J.; BURKHOLDER., J. B. $H+O_3$ fourier-transform infrared emission and laser absorption studies of oh ($X^2 \Pi$) radical: An experimental dipole moment function and state-to-state Einstein a coefficients. **Journal of Chemical Physics**, v. 93(10), p. 7003–7019, 1990. 38

NORMAND, C. Y.; POMEAU, Y.; VELARDE, M. G. Convective instability: A physicist's approach. **Reviews of Modern Physics**, v. 49, p. 581–622, 1977. 4, 23, 25, 26, 93, 95, 96

OGURA, Y.; PHILLIPS, N. A. Scale analysis of deep and shallow convection in the atmosphere. **Journal of Atmospheric Sciences**, v. 19, p. 173–179, 1962. 4, 23

PAN, C. J.; RAO, P. B. Low altitude quasi-periodic radar echoes observed by the Gadanki VHF radar. **Geophysical Research Letters**, v. 29, n. 11,1530, p. 25(1–4), 2002. 64

_____. Morphological study of the field-aligned E-layer irregularities observed by the Gadanki VHF radar. **Annales Geophysicae**, n. 22, p. 3799â3804, 2004. 66

PAN, C. J.; TSUNODA, R. Quasi-periodic echoes observed with the Chung-Li VHF radar during the SEEK campaign. **Geophysical Research Letters**, v. 25, n. 11, p. 1809–1812, 1998. 64

PAN, C. J.; TSUNODA, R. T. Semidiurnal behavior of quasi-periodic echoes in the mid-latitude Es region observed with the Chung-Li VHF radar. **Geophysical Research Letters**, v. 26, p. 2621–2624, 1999. 64

PATRA, A. K.; SRIPATHI, S.; SIVAKUMAR, V.; RAO, P. B. Evidence of kilometer-scale waves in the lower E region from high resolution VHF radar observations over Gadanki. **Geophysical Research Letters**, v. 29, n. 10, p. 1499, 2002. 64

PAULA, E. R. de. **Resposta da regão F ionosfeŕica ás tempestades magnéticas em baixas latitudes no Brasil**. Tese (Doutorado) — Instituto Nacional de Pesquisas Espaciais (INPE), São Jose dos Campos, 1986. Disponível em: <http://urlib.net/6qtX3pFwXQZ3r59YCT/GT4oS>. 105

PIANI, C.; DURRAN, D.; ALEXANDER, M. J.; HOLTON, J. R. A numerical study of three-dimensional gravity waves triggered by deep tropical convection and their role in the dynamics of the QBO. **Journal of the Atmospheric Sciences**, v. 57, n. 22, p. 3689–3702, November 2000. 8

PICONE, J. M.; HEDIN, A. E.; DROB, D. P.; AIKIN, A. C. NRLMSISE-00 empirical model of the atmosphere: Statistical comparisons and scientific issues. **Journal of Geophysical Research**, v. 107, n. A12, p. 1468, 10.1029/2002JA009430 2002. 40

RAO, N. V.; PATRA, A. K.; RAO, S. V. B. Some new aspects of low-latitude E-region QP echoes revealed by Gadanki radar: Are they due to Kelvin-Helmholtz instability or gravity waves? **Journal of Geophysical Research**, v. 113, n. A03309, 2008. 64, 65

REISIN, E. R.; SCHEER, J. Gravity wave activity in the mesopause region from airglow measurements at EL Leoncito. **Journal of Atmospheric and Solar-Terrestrial Physics**, v. 66, p. 655–661, 2004. 10

RICHMOND, A. D. Gravity wave generation, propagation, and dissipation in the thermosphere. **Journal of Geophysical Research**, v. 83, p. 4131–4145, 1978. 5

_____. Modeling the ionospheric wind dynamo: a review. **Pure and Applied Geophysics**, v. 131, n. 3, p. 413–435, 1989. 21

RISHBETH, H. The ionospheric E-layer and F-layer dynamos - a tutorial review. **Journal of Atmospheric and Solar-Terrestrial Physics**, v. 59, p. 1873–1880, 1997. 21

RISHBETH, H.; GARRIOTT, O. K. **Introduction to ionospheric physics**. New York: Academic Press, 1969. 2

ROGISTER, A.; D'ANGELO, N. Type II irregularities in the equatorial electrojet. **Journal of Geophysical Research**, v. 75, p. 3879–3887, 1970. 63

SARKHEL, S.; MATHEWS, J. D.; RAIZADA, S.; SEKAR, R.; CHAKRABARTY, D.; GUHARAY, A.; JEE, G.; KIM, J.; KERR, R. B.; RAMKUMAR, G.; SRIDHARAN, S.; WU, Q.; MLYNCZAK, M. G.; III, J. M. R. A case study on occurrence of an unusual structure in the sodium layer over Gadanki, India. **Earth, Planets and Space**, v. 67:19, 2015. 33, 35, 36, 53

SARKHEL, S.; SEKAR, R.; CHAKRABARTY, D.; SRIDHARAN, S. A case study on the possible altitude-dependent effects of collisions on sodium airglow emission. **Journal of Geophysical Research**, v. 115, n. A10306, 2010. 12

SCHUNK, R. W.; NAGY, A. F. **Ionospheric physics, plasma physics, and chemistry**. [S.l.]: Cambridge University Press, New York, 2000. 4

SHIMKHADA, D. B. **Investigating Small-Scale Dynamical Features in the Mesopause Region**. All Graduate Theses and Dissertations. Paper 731. Tese (Doutorado) — Utah State University, 2010. Disponível em: <http://digitalcommons.usu.edu/etd/731>. 11, 14

SHUME, E. B.; RODRIGUES, F. S.; MANNUCCI, A. J.; PAULA, E. R. de. Modulation of equatorial electrojet irregularities by atmospheric gravity waves. **Journal of Geophysical Research**, v. 119, p. 366–374, 2014. 66, 67, 74

SNIVELY, J. B. Mesospheric hydroxyl airglow signatures of acoustic and gravity waves generated by transient tropospheric forcing. **Geophysical Research Letters**, v. 40, p. 4533–4537, 2013. 50

SNIVELY, J. B.; PASKO, V. P. Antiphase OH and OI airglow emissions induced by a short-period ducted gravity wave. **Geophysical Research Letters**, v. 32, n. L08808, 2005. 38, 39

_____. Excitation of ducted gravity waves in the lower thermosphere by tropospheric sources. **Journal of Geophysical Research**, v. 113, p. A06303, 2008. 33, 34, 56

SOBRAL, J. H. A.; ABDU, M.; BATISTA, I.; ZAMLUTTI, C. Wave disturbances in the low latitude ionosphere and equatorial ionospheric plasma depletions. **Journal of Geophysical Research**, v. 86, p. A3, 1981. 10, 12

SPIEGEL, E. A.; VERONIS, G. On the Boussinesq approximation for a compressible fluid. **Astrophysical Journal**, v. 131, p. 442–447, 1960. 4, 23

SWENSON, G. R.; GARDNER, C. S. Analytical models for the response of mesospheric Na and OH layers to atmospheric gravity waves. **Journal of Geophysical Research**, v. 103, p. 6271–6294, 1998. 33, 39

TAKAHASHI, H.; BATISTA, P. P.; CLEMESHA, B. R.; SIMONICH, D. M.; SAHAI, Y. Correlations between OH, NaD, and OI 5577Å emissions in the airglow. **Planetary and Space Science**, v. 27, p. 801–807, 1979. 33

TAKAHASHI, H.; BATISTA, P. P.; SAHAI, Y.; CLEMESHA, B. R. Atmospheric wave propagation in the mesopause region observed by the OH (8,3) band, NaD, O_2Å(8645Å) band and OI 5577Å nightglow emissions. **Planetary and Space Science**, v. 33, p. 381–384, 1985. 33

TAKAHASHI, H.; GOBBI, D.; BATISTA, P. P.; MELO, S. M. L.; TEIXEIRA, N. R.; BURITI, R. A. Dynamical influence on the equatorial airglow observed from the South American sector. **Advance in Space Research**, v. 21, n. 6, p. 817–825, 1998. 10

TAKAHASHI, H.; TAYLOR, M. J.; PAUTET, P. D. Simultaneous observation of ionospheric plasma bubbles and mesospheric gravity waves during the SpreadFex campaign. **Annales Geophysicae**, v. 27, p. 1477–1487, 2009. 10, 12

TAORI, A.; TAYLOR, M. J.; FRANKE, S. Terdiurnal wave signatures in the upper mesospheric temperature and their association with the wind fields at low latitudes (20°N). **Journal of Geophysical Research**, v. 110, n. D09S06, 2005. 10

TAYLOR, M. J.; EDWARDS, R. Observations of short period mesospheric wave patterns: In situ or tropospheric wave generation? **Geophysical Research Letters**, v. 18, n. 7, p. 1337–1340, 1991. 33

TAYLOR, M. J.; HAPGOOD, M. A. On the origin of ripple-type wave structure in the OH nightglow emission. **Planetary and Space Science**, v. 38, n. 11, p. 1421–1430, 1990. 33

TURNBULL, D. N.; LOWE, R. P. New hydroxyl transitions probabilities and this importance in airglow studies. **Planetary and Space Science**, v. 37(6), p. 723–738, 1989. 38

VARGAS, F.; SWENSON, G.; LIU, A.; GOBBI, D. $O(^1s)$, OH, and O_2(b) airglow layer perturbations due to AGWs and their implied effects on the atmosphere. **Journal of Geophysical Research**, v. 112, p. D14102, 2007. 33

WALTERSCHEID, L. G.; SCHUBERT, G.; BRINKMAN, D. G. Small-scale gravity waves in the upper mesosphere and lower thermosphere generated by deep tropical convection. **Journal of Geophysical Research**, v. 106, n. D23, p. 31,825–31,832, 2001. 33

WEI, D.; BLYTH, A. M.; ; RAYMOND, D. J. Buoyancy of convective clouds in Toga Coare. **Journal of Atmospheric Sciences**, v. 55, p. 3381–3391, 1998. 30

WHITEWAY, J. H.; CARSWELL, A. I. Lidar observations of gravity wave activity in the upper stratosphere over Toronto. **Journal of Geophysical Research**, v. 14, p. 113–124, doi:10.1029/2001GL014514., 1995. 3

WOODMAN, R.; YAMAMOTO, M.; FUKAO, S. Gravity waves modulation of gradient drift instabilities in mid-latitude sporadic E irregularities. **Geophysical Research Letters**, v. 18, n. 7, p. 1197–1200, 1991. 64

WOODMAN, R. F.; CHAU, J. L.; AQUINO, F. Low-latitude field-aligned irregularities observed in the E region with the Piura VHF radar: First results. **Radio Science**, v. 34, n. 4, p. 983–990, 1999. 64

YAMADA, Y. H.; FUKUNISHI, H.; NAKAMURA, T.; TSUDA, T. Breaking of small-scale gravity wave and transition to turbulence observed in OH airglow. **Geophysical Research Letters**, v. 28, p. 2153–2156, 2001. 33

YAMAMOTO, M.; FUKAO, S.; WOODMAN, R. F.; OGAWA, T.; TSUDA, T.; KATO, S. Midlatitude E region field-aligned irregularities observed with the MU radar. **Journal of Geophysical Research**, v. 96, p. 15,943–15,949, 1991. 64

YEH, K.; LIU, C. **Theory of ionospheric waves**. New York: Academic press, 1972. (International geophysical series, v. 17). 18

_____. Acoustic-gravity waves in the upper atmosphere. **Reviews of Geophysics**, v. 1 (2), p. 193–216, 1974. 5

YU, Y.; HICKEY, M. P. Numerical modeling of a gravity wave packet ducted by the thermal structure of the atmosphere. **Journal of Geophysical Research**, v. 112, n. A06308, 2007. 8

ZHANG, S. D.; YI, F. A numerical study of propagation characteristics of gravity wave packets propagating in a dissipative atmosphere. **Journal of Geophysical Research**, v. 107, n. D14, p. 4222, 2002. 8

APPENDIX A - GOVERNING GROWTH EQUATION OF THE CON-VECTIVE INSTABILITY

We consider the atmospheric density (ρ) and pressure (p) to have small variation in the horizontal direction ($\hat{x}$), in comparison to the large variation in the vertical direction ($\hat{y}$) so that we may neglect the horizontal fluid advection in comparison to the vertical fluid convection. On the other hand, the vertical ($\hat{y}$) and horizontal ($\hat{x}$) variations of the wind ($\vec{w}$) is governed by the incompressible flow condition. Under such horizontally-stratified-incompressible conditions, the hydrodynamic equations may be written in the following form:

$$\frac{\partial \rho}{\partial t} = -w_y \frac{\partial \rho}{\partial y}; \qquad \frac{\partial p}{\partial t} = -w_y \frac{\partial p}{\partial y}; \qquad p = \rho R T \qquad (A.1)$$

$$\frac{\partial w_y}{\partial t} = -\frac{1}{\rho} \frac{\partial p}{\partial y} - g; \qquad \frac{\partial w_y}{\partial y} + \frac{\partial w_x}{\partial x} = 0 \qquad (A.2)$$

Taking a time derivative of the momentum equation (A.2) and substituting expressions from (A.1), leads to the following equation for the vertical wind w_y:

$$\frac{\partial^2 w_y}{\partial t^2} = \frac{1}{\rho} \left[w_y \frac{\partial^2 p}{\partial y^2} + \frac{\partial p}{\partial y} \frac{\partial w_y}{\partial y} \right] - \frac{1}{\rho^2} \frac{\partial p}{\partial y} \left[\frac{\partial \rho}{\partial y} \right] w_y$$

or

$$\frac{\partial^2 w_y}{\partial t^2} = -\omega_b^2 w_y + \frac{1}{\rho} \frac{\partial p}{\partial y} \frac{\partial w_y}{\partial y} \qquad (A.3)$$

where ω_b is the Brunt-Vaisala frequency defined by following expression:

$$\omega_b^2 = \frac{1}{\rho^2} \frac{\partial p}{\partial y} \frac{\partial \rho}{\partial y} - \frac{1}{\rho} \frac{\partial^2 p}{\partial y^2} \qquad (A.4)$$

Depending on whether w_b is negative (positive), w_y may grow (oscillate) in time, leading to the instability (gravity wave). Kherani et al. (2011) and Kherani et al. (2012) have used compressible form of (A.3) to study the acoustic-gravity wave dynamics. The second term in (A.3) is a non-local term that determines the preferred wavelength of the growing instability or the gravity wave. The growth equation (A.3) is completely nonlinear as no linear assumptions are made so far.

The ω_b^2 expression (A.4) is different from the following known expression (NORMAND et al., 1977):

$$\omega_b^2 = \frac{1}{\rho_h^2} \frac{\partial p_h}{\partial y} \frac{\partial \rho}{\partial y}$$

93

A.1 Non-Boussinesq (NB) and Boussinesq (OB) expressions of ω_b

A.1.1 Diabatic Non-Boussinesq (DNB) expression

We consider ρ to be composed of the hydrostatic equlibrium density ρ_h and a non-hydrostatic density ρ_t i.e.

$$\rho = \rho_h + \rho_t; \quad p = p_h + p_t; \quad \rho_h = -\frac{1}{g}\frac{\partial p_h}{\partial y}; \quad \rho_h + \rho_t = \frac{p_h + p_t}{RT} \tag{A.5}$$

In general, using the state of gas equation, the density gradient may be written as follows:

$$\frac{1}{\rho}\frac{\partial \rho}{\partial y} = \frac{1}{p}\frac{\partial p}{\partial y} - \frac{1}{T}\frac{\partial T}{\partial y} \tag{A.6}$$

or

$$\frac{1}{\rho}\frac{\partial \rho}{\partial y} = -\frac{\rho_h}{\rho}\frac{g}{RT} + \frac{1}{p}\frac{\partial p_t}{\partial y} - \frac{1}{T}\frac{\partial T}{\partial y} = -\eta\gamma_{ac} - \gamma_e + \frac{1}{p}\frac{\partial p_t}{\partial y} \tag{A.7}$$

where γ_{ac} and γ_e are the auto-convection and environment lapse rates respectively. The last term is the contribution from the isothermal compressibility and is set to be zero for the isothermal-incompressible flow considered in the present study, i.e.,

$$\frac{1}{p}\frac{\partial p_t}{\partial y} = 0 \tag{A.8}$$

This leads to the following expression for the density gradient:

$$\frac{1}{\rho}\frac{\partial \rho}{\partial y} = -(\eta\gamma_{ac} + \gamma_e) \tag{A.9}$$

Assuming the hydrostatic density scale height equals to the equilibrium pressure scale height -1/γ_{ac} (shallow atmosphere assumption i.e. $\gamma_{ac} > \gamma_e$),

$$\frac{1}{\rho_h}\frac{\partial \rho_h}{\partial y} = -\gamma_{ac} - \gamma_e \approx -\gamma_{ac}$$

(A.9) reduces to the following expression

$$\frac{1}{\rho}\frac{\partial \rho_t}{\partial y} = -\gamma_e \tag{A.10}$$

which states that the density change is owing to the thermal expansion. The shallow atmosphere condition together with the iso-thermal incompressible condition (A.8) ensures the incompressibility in the troposphere (MAHRT, 1986).

Using shallow atmosphere condition, we may also obtain following expressions:

$$\frac{1}{\rho}\frac{\partial^2 p}{\partial y^2} = -\eta g \frac{1}{\rho_h}\frac{\partial \rho_h}{\partial y} + \frac{1}{\rho}\frac{\partial^2 p_t}{\partial y^2} \approx \eta g \gamma_{ac}; \quad \frac{1}{\rho}\frac{\partial p}{\partial y} = -\eta g + \frac{1}{\rho}\frac{\partial p_t}{\partial y} \approx -\eta g \qquad \text{(A.11)}$$

Substitution of (A.9, A.11) into (A.4) leads to the non-Boussinesq non-linear expression for the Brunt-Vaisala frequency:

$$\omega_b^2 = \eta g[(\eta - 1)\gamma_{ac} + \gamma_e] \qquad \text{(A.12)}$$

where $\eta = \frac{\rho_h}{\rho}$. This is a general DNB expression for the Brunt-Vaisala frequency, obtained in the present study.

A.1.2 Adiabatic Non-Boussinesq (ANB) expression

In order to obtain an expression for η, we consider the nature of expansion to be compressible adiabatically while incompressible isothermally. The adiabatic compressible condition is described by the following law of thermodynamics:

$$\frac{1}{\rho}\frac{\partial \rho}{\partial y} = \frac{c_p}{\gamma R}\gamma_e \qquad \text{(A.13)}$$

The isothermal-incompressible condition (A.8) led to (A.10). Equations (A.10,A.13) lead to the following relation:

$$\frac{\rho_t}{\rho} = -\frac{\gamma R}{c_p} \Rightarrow \eta = \frac{\rho_h}{\rho} = \gamma \qquad \text{(A.14)}$$

Thus, with the adiabatic compressible-isothermal incompressible condition, we obtain the following expression for the Brunt-Vaisala frequency:

$$\omega_b^2 = \gamma g(\gamma \gamma_{ad} + \gamma_e) \qquad \text{(A.15)}$$

where γ_{ad} is the adiabatic lapse rate.

A.1.3 Oberbeck-Boussinesq (OB) expression

A remaining OB assumption is the linearization of $\frac{1}{\rho}$ in (A.4). Thus, the OB expression for ω_b may be obtained by linearizing the η in (A.12) in a following way (NORMAND et al., 1977):

$$\eta = \frac{\rho_h}{\rho} = \frac{\rho_h}{\rho_h(1 + \frac{\rho_t}{\rho_h})} \approx 1 - \frac{\rho_t}{\rho_h}$$

This linearization is done only for η appearing with γ_{ac} where gravity is coming with γ_{ac} i.e. with the hydrostatic pressure gradient force. For η appearing only with gravity can be taken as unity. With these linearization scheme, (A.12) reduces to the following form:

$$\omega_b^2 = -g\left(\frac{\rho_t}{\rho_h}\gamma_{ac} - \gamma_e\right)$$

Using adiabatic-incompressible condition (A.14), above expression reduces to the known OB expression of the Brunt-Vaisala frequency (NORMAND et al., 1977):

$$\omega_{bB}^2 = g(\gamma_{ad} + \gamma_e) \tag{A.16}$$

APPENDIX B - NUMERICAL METHODS

Numerical simulation helps to understand the different physical phenomena that occur in our environment, which are modeled using mathematical tools that result in analytical differential equation whose solution in most cases can not be solved. The finite difference methods for derivatives are one of the simplest and of the premier methods to solve differential equations. The advent of finite difference techniques in numerical applications began in the early 1950s and their development was stimulated by the emergence of computers that offered a convenient framework for dealing with complex problems of science and technology.

B.1 Finite Difference Methods

The principle of finite difference methods is close to the numerical schemes used to solve ordinary differential equations. The derivatives are approximated by linear combinations. It uses the Taylor expansion to approximate the derivatives.

Taylor series is defined in the real domain D, if $u \in C^\infty(D)$, then for every $x_i \in D$ have:

$$u(x) = \sum_{n=0}^{\infty} \frac{(x - x_i)^n}{n!} \left(\frac{\partial^n u}{\partial x^n} \right)_i \tag{B.1}$$

using the mesh of Figure B.1, we have: $x_i = i\,\Delta x$ and therefore:
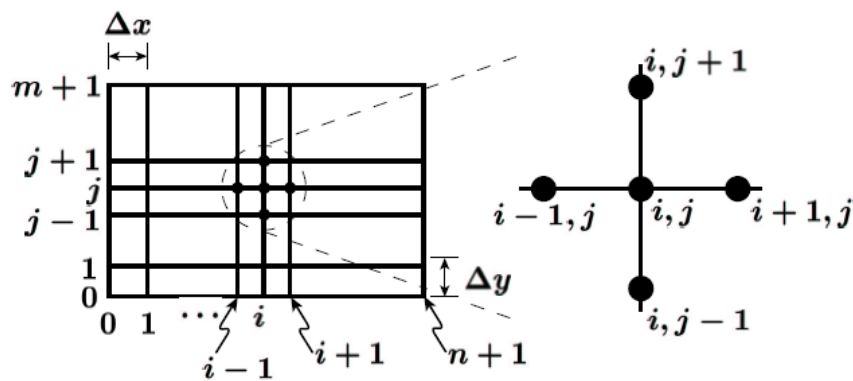
Figure B.1 - Mesh points

$$u_{i+1} = u_i + \Delta x \left(\frac{\partial u}{\partial x}\right)_i + \frac{(\Delta x)^2}{2!} \left(\frac{\partial^2 u}{\partial x^2}\right)_i + \frac{(\Delta x)^3}{3!} \left(\frac{\partial^3 u}{\partial x^3}\right)_i + \frac{(\Delta x)^4}{4!} \left(\frac{\partial^4 u}{\partial x^4}\right)_i \ldots \quad \text{(B.2)}$$

it follows that the forward difference

$$\left(\frac{\partial u}{\partial x}\right)_i = \frac{u_{i+1} - u_i}{\Delta x} + \mathcal{O}(\Delta x) \quad \text{(B.3)}$$

$$u_{i-1} = u_i - \Delta x \left(\frac{\partial u}{\partial x}\right)_i + \frac{(\Delta x)^2}{2!} \left(\frac{\partial^2 u}{\partial x^2}\right)_i - \frac{(\Delta x)^3}{3!} \left(\frac{\partial^3 u}{\partial x^3}\right)_i + \frac{(\Delta x)^4}{4!} \left(\frac{\partial^4 u}{\partial x^4}\right)_i \ldots \quad \text{(B.4)}$$

it follows that the backward difference

$$\left(\frac{\partial u}{\partial x}\right)_i = \frac{u_i - u_{i-1}}{\Delta x} + \mathcal{O}(\Delta x) \quad \text{(B.5)}$$

Subtracting equation (B.4) from equation (B.2), we can be obtained as,

$$\left(\frac{\partial u}{\partial x}\right)_i = \underbrace{\frac{u_{i+1} - u_{i-1}}{2\Delta x}}_{\text{central difference}} \underbrace{-\frac{(\Delta x)^2}{3!} \left(\frac{\partial^3 u}{\partial x^3}\right)_i - \frac{(\Delta x)^4}{5!} \left(\frac{\partial^5 u}{\partial x^5}\right)_i - \ldots}_{\text{truncation error } \mathcal{O}(\Delta x)^2} \quad \text{(B.6)}$$

Adding equation (B.2) and equation (B.4), we can be obtained as,

$$\left(\frac{\partial^2 u}{\partial x^2}\right)_i = \underbrace{\frac{u_{i+1} - 2u_i + u_{i-1}}{(\Delta x)^2}}_{\text{second derivative}} \underbrace{+\frac{(\Delta x)^2}{4!} \left(\frac{\partial^4 u}{\partial x^4}\right)_i + \frac{(\Delta x)^4}{6!} \left(\frac{\partial^6 u}{\partial x^6}\right)_i + \ldots}_{\text{truncation error } \mathcal{O}(\Delta x)^2} \quad \text{(B.7)}$$

The finite difference scheme in space and time for a given dependent variable, say, $\zeta(x)$,

$$\frac{d(\zeta)}{dx} \equiv \frac{\Delta \zeta}{\Delta x} \quad \text{(B.8)}$$

$$\frac{d(\zeta)}{dx} \equiv \left[\overbrace{\frac{(\zeta_{x+1} - \zeta_x)}{\Delta x}}^{\text{Forward Difference}} \right] \quad \text{(B.9)}$$

$$\frac{d(\zeta)}{dx} \equiv \left[\overbrace{\frac{(\zeta_x - \zeta_{x-1})}{\Delta x}}^{\text{Backward Difference}} \right] \quad \text{(B.10)}$$

$$\overbrace{\frac{d(\zeta)}{dx} \equiv \left[\frac{(\zeta_{x+1} - \zeta_{x-1})}{2\Delta x} \right]}^{\text{Central Difference}} \tag{B.11}$$

And being $\zeta(x)$ differentiable more than once ($\in$ class $C^n \mid n > 1$)) will also:

$$\frac{d^2(\zeta)}{dx^2} \equiv \frac{\Delta^2 \zeta}{\Delta x^2}; \frac{d^3(\zeta)}{dx^3} \equiv \frac{\Delta^3 \zeta}{\Delta x^3}; \cdots, \frac{d^n(\zeta)}{dx^n} \equiv \frac{\Delta^n \zeta}{\Delta x^n} \tag{B.12}$$

Differential equations of atmosphere and ionosphere are written, in a general form as follows:

$$a\frac{\partial \zeta}{\partial t} + u\frac{\partial \zeta}{\partial x} = b\frac{\partial^2 \zeta}{\partial x^2} + c\frac{\partial \zeta}{\partial x} + d\zeta + e$$

where (a, b, c, d, e) are coefficients depending on (x, t, ζ), u is the velocity field depending on (x, t, ζ). ζ represents density, velocity and pressure.

To solve this non-linear PDE, the Forward-Time-Centered-Space finite difference method is commonly employed, which reduces the PDE to an algebraic equation. Under FTCS method, derivatives are approximated using Taylor expansion of function $\zeta(x + \Delta x, t + \Delta t)$, which are described above, can be written as follows:

$$\frac{\partial \zeta}{\partial t} \approx \frac{\zeta(t + \Delta t) - \zeta(t)}{\Delta t} + O(\Delta t) \quad ; \quad \frac{\partial \zeta}{\partial x} \approx \frac{\zeta(x + \Delta x) - \zeta(x - \Delta x)}{2\Delta x} + O(\Delta x^2)$$

With these approximations, the PDE may be written in two forms, corresponding to the explicit and implicit integration schemes respectively:

$$\zeta(x, t + \Delta t) = \zeta(x, t) + \Delta t[\alpha\zeta(x + \Delta x, t) + \beta\zeta(x, t) + \eta\zeta(x - \Delta x, t)]$$

$or, \zeta(x, t + \Delta t) = \zeta(x, t) + \Delta t[\alpha\zeta(x + \Delta x, t + \Delta t) + \beta\zeta(x, t + \Delta t) + \eta\zeta(x - \Delta x, t + \Delta t)]$

Here coefficients α, β, η are the functions of $\rho(t + \Delta t)$, $p(t + \Delta t)$ etc. In the explicit scheme, the R.H.S. is evaluated at the current time (t) while in the implicit scheme, the R.H.S. is evaluated at the forward time $(t + \Delta t)$. Using Taylor expansion of R.H.S. of PDE, it may be shown that the explicit scheme is first-order accurate in time while the implicit scheme is unconditionally stable. Moreover, for the PDE having the first order space derivative, $\zeta(x, t + \Delta t)$ is not connected with the $\zeta(x, t)$ under explicit scheme leading to an artificial diffusion term that effectively slows down the evolution of PDE. To avoid these problems, the implicit integration scheme may be adopted. The final equation leads to the set of algebraic equations for $\zeta(x, t + \Delta t)$.

It represents the matrix equation with the large coefficients matrix. This matrix equation is solved by using the Successive Over-relaxation (SOR) method. Figure B.2 shows the space-time diagram of Crank-Nicholson scheme.
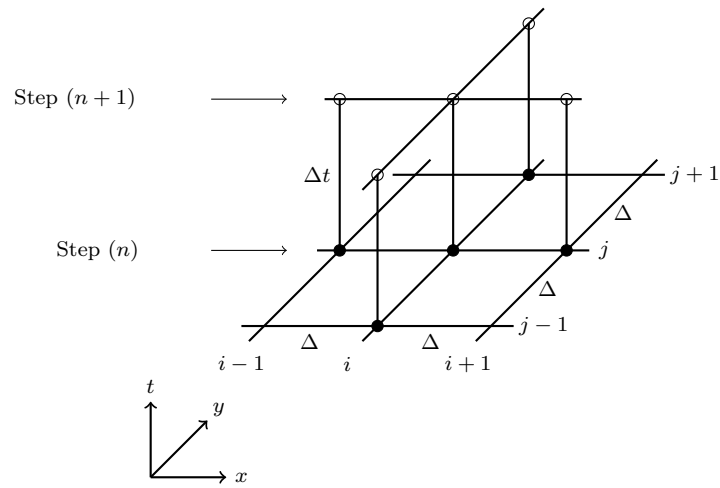
Figure B.2 - Diagram represents the space-time implicit Crank-Nicholson method.

B.2 Successive Over-relaxation (SOR) Method

By solving PDE using the finite difference method, the equation is transformed into a matrix equation. The matrix elements are tridiagonal and quindiagonal. The schemes of quindiagonal and tridiagonal matrices are presented in Figure B.3.
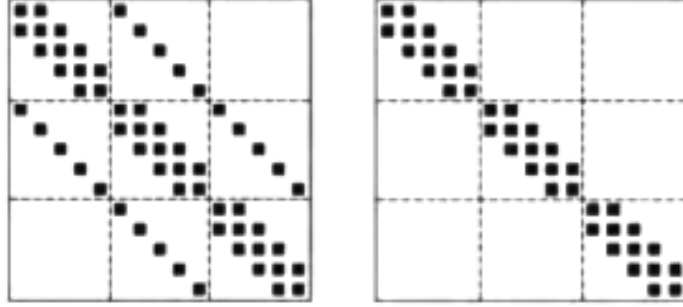
Figure B.3 - Quindiagonal and tridiagonal matrices scheme.

The characteristic of these sparse arrays allow the use of iterative methods, such as Sucessive Over-relaxation (SOR). Given a matrix equation:

$$\mathbf{Au} = \mathbf{w} \tag{B.13}$$

where $\mathbf{A}$ is a matrix (tridiagonal in our case), $\mathbf{w}$ is the known vector and $\mathbf{u}$ is the vector being determined, we can assume a solution to some initial value of $\mathbf{u}$, say $\mathbf{u}^{(o)}$, and proceed in successive steps p to attempt to improve *inexact* solution $\mathbf{u}^{(p)}$. This procedure is represented by the following matrix equation:

$$\mathbf{u}^{(p+1)} = \mathbf{Pu}^{(p)} + \mathbf{c} \tag{B.14}$$

where $\mathbf{P}$ is the iteration matrix, and an improved solution $\mathbf{u}^{(p+1)}$ is derived explicitly from the previous solution $\mathbf{u}^{(p)}$. The matrix $\mathbf{P}$ is related to the given matrix $\mathbf{A}$ and the constant vector $\mathbf{c}$ is related to the known vector $\mathbf{w}$. For sufficiently larger value of p, convergence is obtained, so that,

$$\lim_{p \to \infty} \mathbf{u}^{(p)} = \mathbf{Pu}^{(p)} + \mathbf{c} \tag{B.15}$$

then the vector $\mathbf{u}^{(\infty)}$ satisfies the matrix equation,

$$(\mathbf{I} - \mathbf{P})\mathbf{u}^{(\infty)} = \mathbf{c} \tag{B.16}$$

101

where $\mathbf{I}$ is the identity matrix. Thus, $\mathbf{u}^{(\infty)}$ will be the solution we require if this matrix equation B.16 is consistent with the equation of interest B.13. It follows that if the vector $\mathbf{c}$ is related to the known vector $\mathbf{w}$ by the non-singular matrix $\mathbf{T}$,

$$\mathbf{c} = \mathbf{Tw} \tag{B.17}$$

then the iteration matrix must satisfy,

$$\mathbf{T}^{-1}(\mathbf{I} - \mathbf{P}) = \mathbf{A} \implies \mathbf{P} = \mathbf{I} - \mathbf{TA} \tag{B.18}$$

The benefit of this procedure is that each improved value $\mathbf{u}^{(p+1)}$ is obtained explicitly. It is informative to associate a physical significance with the step-by-step improvement of the 'solution'. In this section we discuss the matrix iterative approach, which uses matrix techniques. It is conventional to decompose a given matrix $\mathbf{A}$ into submatrices i.e., $\mathbf{A} = \mathbf{D} + \mathbf{U} + \mathbf{L}$. We assume that all the diagonal elements are finite, we can write the matrix equation B.13 as,

$$\mathbf{A}'\mathbf{u} = \mathbf{w}' \tag{B.19}$$

where

$$\mathbf{A}' = \mathbf{D}^{-1}\mathbf{A}; \mathbf{A}' = \mathbf{I} + \mathbf{U}' + \mathbf{L}'$$

In the given matrix $\mathbf{A}$, $\mathbf{D}$ is a diagonal matrix, $\mathbf{I}$ is the identity matrix, $\mathbf{L}$ is a lower triangular matrix with elements only below the diagonal, and $\mathbf{U}$ is an upper triangular matrix with elements only above the main diagonal. Figure B.4 shows the representation of the matrix.
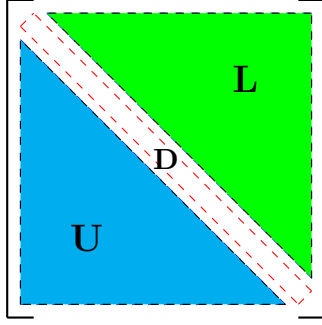
Figure B.4 - Diagram of divided parts ($\mathbf{U}$, $\mathbf{L}$ and $\mathbf{D}$) of a matrix $\mathbf{A}$.

The method of Successive Over-relaxation uses the Gauss-Seidel formulation, but with an optimized constant value of the relaxation parameter ω,

$$(\mathbf{I} + \omega\mathbf{L}')\mathbf{u}^{(p+1)} = (1 - \omega)\mathbf{I}\mathbf{u}^{(p)} - \omega\mathbf{U}'\mathbf{u}^{(p)} + \omega\mathbf{w}' \tag{B.20}$$

or,

$$\mathbf{u}^{(p+1)} = (\mathbf{I} + \omega\mathbf{L}')^{-1}\big[(1 - \omega)\mathbf{I} - \omega\mathbf{U}'\big]\mathbf{u}^{(p)} + (\mathbf{I} + \omega\mathbf{L}')^{-1}\omega\mathbf{w}' \tag{B.21}$$

In the Gauss-Seidel method, ω is taken as unity (i.e., ω=1) though in practice the fastest rate of convergence is not necessary achieved with ω equal to unity and is frequently increased by taking ω greater than unity, is called Successive Over-relaxation method. If $\omega < 1$, is called the Successive under-relaxation method. It can be shown that this method will not converge for the over-relaxation factor, ω, outside the range $0 < \omega < 2$. As stated previously, in solving matrix equations from finite difference equations that were treated in the work presented in this thesis was employed SOR method.

APPENDIX C - GEOMETRY OF MAGNETIC DIPOLE COORDINATE SYSTEM

In the terrestrial ionosphere the magnetic field can impose a strong anisotropy by restricting transport processes perpendicular to the lines of force. If the field is approximately dipolar it can be useful to work in an aligned coordinate system even though the vector operations are somewhat more complicated than in a Cartesian or Spherical polar representation. Here we present the spherical polar coordinates system that frequently occur.

The dipole geometry is done by choosing a line of a dipolar magnetic field centered and aligned to the rotation axis of the Earth with radial and meridional component as shown in Figure C.1.
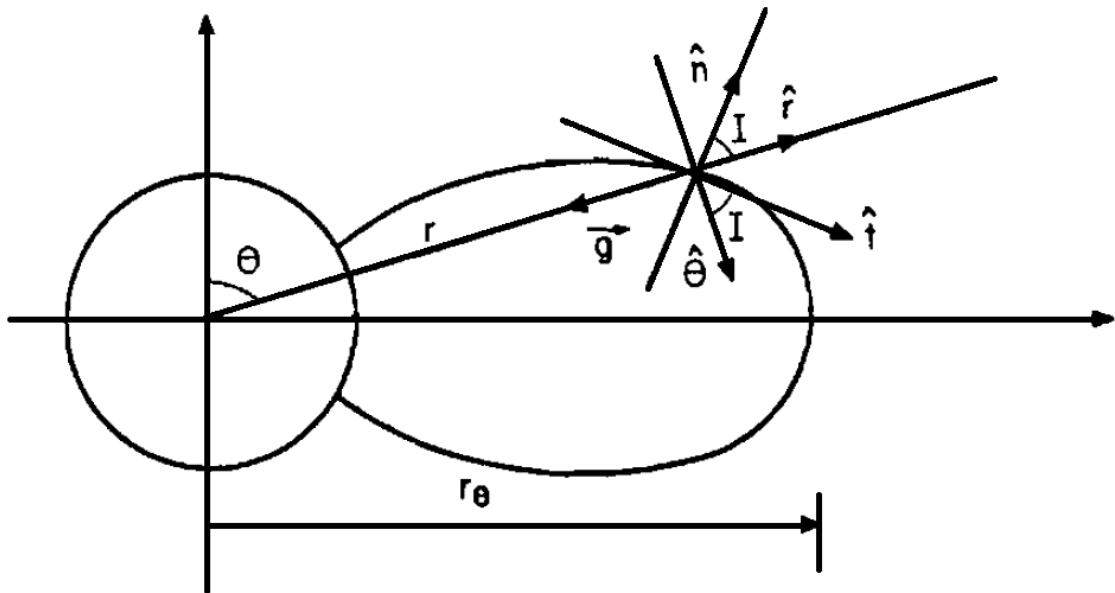
Figure C.1 - Geometry of a magnetic field line for determining the unit vector $\hat{n}$ parallel to the magnetic field.
Source: Adapted from Paula (1986)

According to the graph, we have:

$$r = r_e \sin^2 \theta \tag{C.1}$$

where θ is a colatitude, r is a radial distance to any point on the field line, r_e is the radial distance of the field line from the equator, $\hat{r}$ is a unit vector in $\vec{r}$ direction, $\hat{\theta}$

is the unit vector in θ, $\hat{n}$ is the unit vector normal to the plane of magnetic field line $r\theta$. I is a magnetic inclination, g is gravitational acceleration, and $\hat{t}$ is unit vector tangent to the field line and in the following form:

$$\hat{t} = sin(I\hat{r}) + cos(I\hat{\theta}) \tag{C.2}$$

Using the definition from the Kirchhoff (KIRCHHOFF, 1991), with $\lambda=\theta$, $r = r_e$ and $r = h + r_e$, we have:

$$B = B_o(1 + 3cos^2\theta)^{1/2}\left(\frac{r_e}{r}\right)^3 \tag{C.3}$$

$$B_r = -2B_o cos\theta\left(\frac{r_e}{r}\right)^3 \tag{C.4}$$

$$B_\theta = -B_o sin\theta\left(\frac{r_e}{r}\right)^3 \tag{C.5}$$

$$B_\phi = 0 \tag{C.6}$$

where B_r is the magnetic field component in the direction of $\vec{r}$ and B_θ is the magnetic field component in the direction of $\hat{\theta}$.

From the configuration of the graph and using the above equations, we can be written as:

$$sinI = \frac{B_r}{B} = \frac{2cos\theta}{\sigma} \tag{C.7}$$

$$cosI = \frac{B_\theta}{B} = \frac{sin\theta}{\sigma} \tag{C.8}$$

$$\vec{g}_{||} = \left(\vec{g} \cdot \hat{t}\right)\hat{t} \longrightarrow \vec{g}_{||} = -gsinI(\hat{t}) \tag{C.9}$$

$$\vec{\nabla}_{||} = \left(\hat{t} \cdot \vec{\nabla}\right)\hat{t} = \hat{t}\frac{\partial}{\partial s} = \left(sinI\frac{\partial}{\partial r} + \frac{cosI}{r}\frac{\partial}{\partial\theta}\right)\hat{t} \tag{C.10}$$

where $\sigma = (1 + 3cos^2\theta)^{1/2}$ and s is arc length of $\vec{B}$.

C.1 Coordinates Transformation

Transformation of the spherical polar coordinates (r,θ,φ) system to a system whose coordinates define parallel and perpendicular directions of magnetic field lines is

defined as (p,q,φ) (KENDALL, 1962):

$$p = \frac{r}{r_e sin^2\theta}; q = \frac{r_e^2 cos\theta}{r^2}; \varphi = \varphi \qquad (C.11)$$

where r_e is a constant with the dimension of length.

$p \longrightarrow$ family of curves representing the magnetic field lines;

$q \longrightarrow$ the family of magnetic equipotential surfaces.

From Equation C.10 with Equations C.7 and C.8 and along the field line $p =$ constant, then

$$\frac{\partial}{\partial r} = \frac{\partial q}{\partial r}\frac{\partial}{\partial q}; \qquad \frac{\partial}{\partial \theta} = \frac{\partial q}{\partial \theta}\frac{\partial}{\partial q}; \frac{\partial q}{\partial r} = -\frac{2r_e^2}{r^3}cos\theta; \qquad \frac{\partial q}{\partial \theta} = -\frac{r_e^2}{r^2}sin\theta.$$

Therefore, in spherical coordinates the operator $\vec{\nabla}$:

$$\vec{\nabla} = \frac{\partial}{\partial r}\hat{r} + \frac{1}{r\partial\theta} + \frac{cosI}{r}\frac{\partial}{\partial\theta}\hat{\theta} + \frac{1}{rsin\theta}\frac{\partial}{\partial\varphi}\hat{\varphi} \qquad (C.12)$$

$$\vec{\nabla}_{||} = \left[\frac{2cos\theta}{\sigma^{1/2}}\left(-\frac{2r_e^2}{r^3}cos\theta\right) + \frac{sin\theta}{r\sigma^{1/2}}\left(-\frac{r_e^2}{r^2}sin\theta\right)\right]\frac{\partial}{\partial q}\hat{t}$$

or,

$$\vec{\nabla}_{||} = \left[-\frac{(1+3cos^2\theta)r_e^2}{r^3\sigma^{1/2}}\frac{\partial}{\partial q}\right]\hat{t}$$

or,

$$\vec{\nabla}_{||} = \left[-\frac{\sigma^{1/2}r_e^2}{r^3}\frac{\partial}{\partial q}\right]\hat{t} \qquad (C.13)$$

C.2   Dipole Curvilinear Coefficients

The curvilinear factors h are given by (HUBA et al., 2000):

$$h_p = \frac{r_e sin^3\theta}{\sigma}, \qquad (C.14)$$

$$h_q = \frac{r^3}{r_e^2}\frac{1}{\sigma}, \qquad (C.15)$$

$$h_\varphi = rsin\theta \qquad (C.16)$$

The divergence is defined as

$$\nabla \cdot \vec{A} = \frac{1}{h_p h_q h_\varphi} \left[\frac{\partial}{\partial p} A_p h_q h_\varphi + \frac{\partial}{\partial q} A_q h_p h_\varphi + \frac{\partial}{\partial \varphi} A_\varphi h_p h_q \right], \tag{C.17}$$

and the gradient is defined as

$$\nabla f = \frac{1}{h_p} \frac{\partial f}{\partial p} \hat{e}_p + \frac{1}{h_q} \frac{\partial f}{\partial q} \hat{e}_q + \frac{1}{h_\varphi} \frac{\partial f}{\partial \varphi} \hat{e}_\varphi. \tag{C.18}$$

where $(\hat{e}_p, \hat{e}_q, \hat{e}_\varphi)$ are the unit vectors along (p, q, φ) directions respectively.

APPENDIX D - SAMI2 IONOSPHERIC MODEL

SAMI2 (Sami2 is Another Model of the Ionosphere) is a physics-based model of the ionosphere which solves hydromagnetic equations describing ionospheric plasma. It is a 2-D (latitude and altitude) ionospheric model developed by the Naval Research Laboratory (NRL)(HUBA et al., 2000). It models the mid and low-latitude ionosphere, including the geomagnetic equator, along a hemispheric grid from 90 to 20,000 km. It is freely available for modification from NRL, and the 2-D nature of the model allows more realistic evolution of the plasma than a 1-D model. It models the plasma and chemical evolution of seven ion species (H^+,H_e^+,N^+,O^+,N_2^+,NO_2^+ and O_2^+) in the altitude range mentioned above.The ion continuity and momentum equations are solved for all seven ion species. The ion temperature equation is solved for three ion species (H^+,H_e^+, and O^+) as well as the electron temperature equation. The neutral composition and temperature are specified using the empirical NRLMSISE00 model and the neutral winds using the HWM07 model. The dynamics of the SAMI2 model enable us to incorporate many parameters to obtain various desired results.

APPENDIX E - NUMERICAL CODES

```
program spr_flux
implicit real*4(a-h,o-z)
parameter (pi=3.14,np=151,nf=61,nq_ex=0,nq=61)
parameter (gamma=1.44,b_c=1.38d-23,da=3.62d-10,r_go=283)


c////////////COORDINATES\\\\\\\\\\\\\\\\\\\\\\\\\\\\\\\\\\\\\\/


dimension rl(np),delta(nq),q(np,nq),p(np,nq),hq(np,nq)
dimension hphi(np,nq),hp(np,nq)
dimension dp(np),dq(np),theta(nq),phi(nf),r(np),rk(np)
dimension p_hp(np,nq),q_hq(np,nq),emf_ik(np,nq)


c////////////ATMOSPHERE\\\\\\\\\\\\\\\\\\\\\\\\\\\\\\\\\\\\\\\\\\/


dimension den_neu(np,nf,nq),temp_o(np,nf,nq),temp_s(np,nf,nq)
dimension press(np,nf,nq),rhoat_o(np,nf,nq),c_sno(np)
dimension delta_t(np,nf,nq),disp(nf,nq),wp_s(nf,nq)
dimension wpo(np,nf,nq),wfo(np,nf,nq),wqo(np,nf,nq)
dimension wpm(np,nf,nq),wfm(np,nf,nq),wqm(np,nf,nq)
dimension wp(np,nf,nq),wf(np,nf,nq),wq(np,nf,nq)
dimension wps(np,nf,nq),wfs(np,nf,nq),wqs(np,nf,nq)
dimension wp_ex(np,nf,nq),wf_ex(np,nf,nq),wq_ex(np,nf,nq)
dimension visc_coef(np),wp_i_max(np),wf_i_max(np),bm_p(np)
dimension div_w(np,nf,nq), alph_4(np,nf,nq)
dimension curl_w_p(np,nf,nq),curl_w_f(np,nf,nq)
dimension curl_w_q(np,nf,nq),div_w_f(np,nf,nq)
dimension d2rho(np,nf,nq),div_w_q(np,nf,nq),div_w_p(np,nf,nq)
dimension dlrho_p(np,nf,nq),dlrho_f(np,nf,nq),dlrho_q(np,nf,nq)
dimension den_neu_o2(np,nf,nq),den_neu_n2(np,nf,nq)
dimension disp_in(nf,nq),disp_fn(nf,nq),c_sn(np)
dimension wf_m(np),wq_m(np),visc_nu(np,nf,nq)
dimension tec_2d_II(nf,nq),w_br_2(np,nf,nq)
dimension rhoat_g(np,nf,nq),rhoat_t(np,nf,nq)
dimension temp_g(np,nf,nq),temp_t(np,nf,nq)
dimension rhoat_oo(np,nf,nq),wp_go(nf,nq)
dimension c_s(np,nf,nq)
```

```
c//////////IONOSPHERE\\\\\\\\\\\\\\\\\\\\\\\\\\\\\\\\\\\\\\\\

      dimension den_i(np,nf,nq),den_o(np,nf,nq),den_io(np,nf,nq)
      dimension den_f(np,nf,nq),den_s(np,nf,nq), den_t(np,nf,nq)
      dimension pot_g(np,nf,nq),pot(np,nf,nq),pot_in(np,nf,nq)
      dimension ug_p(np,nf,nq),ug_f(np,nf,nq),ug_q(np,nf,nq)
      dimension ug_nl_p(np,nf,nq),ug_nl_f(np,nf,nq),ug_nl_q(np,nf,nq)
      dimension up(np,nf,nq),uf(np,nf,nq),uq(np,nf,nq)
      dimension flux_p(np,nf,nq),flux_f(np,nf,nq),flux_q(np,nf,nq)
      dimension cur_p(np,nf,nq),cur_f(np,nf,nq),cur_q(np,nf,nq)
      real*4 mag_f(np,nf,nq),mag_p(np,nf,nq),mag_q(np,nf,nq)
      real*4 mag_fo(np,nf,nq),mag_po(np,nf,nq),mag_qo(np,nf,nq)
      real*4 mag_fm(np,nf,nq),mag_pm(np,nf,nq),mag_qm(np,nf,nq)
      real*4 mag_ft(np,nf,nq),mag_pt(np,nf,nq),mag_qt(np,nf,nq)
      real*4 mag_total(np,nf,nq),mag_max,s(np,nf,nq)
      dimension rnu_in(np),rnu_en(np),tec_2d(nf,nq)
      dimension rk_i(np),rk_e(np),rk_i1(np),rk_e1(np),si(np)
      dimension uam_p(np,nf,nq),uam_f(np,nf,nq),uam_q(np,nf,nq)
    dimension rho_o3o(np,nf,nq),rho_o3(np,nf,nq)
    dimension rhoat_oh(np,nf,nq),oh_ag(np,nf,nq)
     dimension den_na(np,nf,nq),den_o_na(np,nf,nq)
     character s_m*35

101    continue

      f_gw=1.;f_gw1=1.


      do i=1,np
      wf_m(i)=0
      wq_m(i)=0
c      wf_m(121)=wf_m(120)
c      wq_m(121)=wq_m(120)
      enddo
```

```fortran
103              format(201(1x,e12.4))
104              format(91(1x,e14.5))


c.............Simulation volume............

        r_ea=6.371d+03
        dr=2.d+00;dphi=atan(2.*dr/(r_ea+300.));dtheta=dphi;

        r_min=0;phi_min=120*pi/180.;theta_min=0*pi/180.
        r_max=300;

        a_pi=pi/180.
        phi_min=315.*a_pi-(nf+1)*dphi/2.
        theta_min=-11.*a_pi+22.7*a_pi-(nq+1)*dtheta/2.
        theta_min=-30*dtheta
        phi_min=-30*dphi

        nophi=nf;ntheta=nq;nor=(r_max-r_min)/dr+1
        !nophi=(nf+1)/2;ntheta=(nq+1)/2;

        print *, dphi,dtheta,nor,nophi,ntheta,nq

c......inputs   MAGNETIC FIELD COORDINATES ...............
c...........p=vertical perpendicular to Magnetic field
c...........q=parallel to the Magnetic field....
c...........phi=azimuthal angle................

        freq_max=0
        do k=1,ntheta
        theta(k)=theta_min+(k-1)*dtheta/1.
        do i=1,nor

                r(i)=r_min+(i-1)*dr
                rk(i)=r(i)*1.d+03
                drk=dr*1.d+03
```

```
c . . . . . . . . . . . . . . . . . . . . . . . . . . . . . . . . . . . . . . . . . . . . . . . . . . . . . . . . . .
          do j=1,nophi

          a1=310;b1=200;a=-1.;b=0.5
          a2=220;b2=250;c=-0.2;d=6.
          a3=220;b3=220;e=-0.45;f=2.5
          yp=10;yq=75;yr=130
          r_y1=r(i)/yp-1
          r_y2=r(i)/yq-1
          r_y3=r(i)/yr-1
          first=a1-b1/(exp(a*r_y1)+exp(b*r_y1))
          second=-a2+b2/(exp(c*r_y2)+exp(d*r_y2))
          third= a3-b3/(exp(e*r_y3)+exp(f*r_y3))
          temp_high=-220+0.55*(first+second)+5.*third
          temp_o(i,j,k)=0.75*temp_high

          a1=310;b1=200;a=-1.;b=0.5
          a2=220;b2=250;c=-0.2;d=10.
          a3=220;b3=220;e=-0.45;f=2.5
          yp=10;yq=65;yr=130;
          yq4=85.;a4=120;b4=150;c4=-5.;d4=18.
          r_y1=r(i)/yp-1
          r_y2=r(i)/yq-1
          r_y3=r(i)/yr-1
          r_y4=r(i)/yq4-1
          first=a1-b1/(exp(a*r_y1)+exp(b*r_y1))
          second=-a2+b2/(exp(c*r_y2)+exp(d*r_y2))
          third= a3-b3/(exp(e*r_y3)+exp(f*r_y3))
          fourth=-a4+b4/(exp(c4*r_y4)+exp(d4*r_y4))
          temp_high=-160+0.55*(first+second+fourth)+5.*third
          temp_o(i,j,k)=0.75*temp_high

!. . . . . . . . . . . . . . . . . . 2 0 0 8 . . . . . . . . . . . . . . . . . . . . . . . . . . . . . . . . . . . . . . . . . . . .
          a1=310;b1=200;a=-2.;b=0.5
          a2=220;b2=250;c=-0.2;d=10.
          a3=220;b3=220;e=-0.25;f=2.5+3.
          yp=10;yq=65;yr=130;
```

```fortran
      yq4=100.;a4=120;b4=250;c4=-1.5;d4=18.
      r_y1=r(i)/yp-1
      r_y2=r(i)/yq-1
      r_y3=r(i)/yr-1
      r_y4=r(i)/yq4-1
      first=a1-b1/(exp(a*r_y1)+exp(b*r_y1))
      second=-a2+b2/(exp(c*r_y2)+exp(d*r_y2))
      third= a3-b3/(exp(e*r_y3)+exp(f*r_y3))
      fourth=-a4+b4/(exp(c4*r_y4)+exp(d4*r_y4))
      a5=220;b5=220;c5=-0.25;d5=5.
      ys=230.;r_y5=r(i)/ys-1
      fifth=a5-b5/(exp(c5*r_y5)+exp(d5*r_y5))
      sixth=-130+1.*(first+second+fourth)+5.2*third++0.5*fifth  !2008 De
      sixth=-320+1.25*(first+second+fourth)+7.5*third+1.5*fifth  !2013 I
      temp_o(i,j,k)=0.75*sixth

!.........2008 december Density profile ................

      a=1.d+25*32*1.6d-27*1.d-08;
      c=-4.5;d=-19.5
      c=-3.5                                           !2013
      yr=130.;r_y=r(i)/yr-1
      rhoat_o(i,j,k)=a*(exp(c*r_y)+exp(d*r_y))

      rho_o3o(i,j,k)=0
      enddo
c.................................................................

            r(i)=(r_min+r_ea)+(i-1)*dr
            r_o=r(i)/cos(theta(k))**2.
            rk_o=r_o*1.d+03
            rk(i)=r(i)*1.d+03
            drk=dr*1.d+03

            delta(k)=sqrt(1.+3.*sin(theta(k))**2.)
            q(i,k)=rk_o**3.*sin(theta(k))/rk(i)**2
            p(i,k)=rk(i)/cos(theta(k))**2.
```

```fortran
                  hq(i,k)=(rk(i)/rk_o)**3./delta(k)
                  hphi(i,k)=rk(i)!*cos(theta(k))
                  hp(i,k)=cos(theta(k))**3./delta(k)

                  dp(i)=drk/cos(theta(k))**3.
                  dq(i)=rk(i)*dtheta*(rk_o/rk(i))**3

            p_hp(i,k)=1./(dp(i)*hp(i,k))
                  q_hq(i,k)=1./(dq(i)*hq(i,k))

         enddo
         enddo


c.......... Ionospheric  parameters ...............

         den_max=0;normn=31

         do k=1,ntheta
         do i=1,nor
!                  emf_ik(i,k)=(rl(i)/6300)**3.*delta(k)/cos(theta(k))**6.
         do j=1,nophi
          yp=4.d+02
          ro=0.85
                  r_n=(r(i)-r_ea)/(yp*cos(theta(k))**5.)
         den_n=3.1d+13*EXP(-(r(i)-80-r_ea)/12.)

!'''''''''''collision  frequencies '''''''''''''''''''''''''''''
         rnu_en(i)=5.4*10.**(-10.)*800.**(1./2.)*den_n !Collision  freq  of
         rnu_in(i)=1.*6.d-02/(r_n-0.2)**(3.5) !collision  freq  of  ions
          if(i.lt.normn)then
                  rnu_en(i)=50
                        rnu_in(i)=50
         endif
!.............................................................
         ome_i=100.   !Ion  Gyrofrequency
```

```fortran
      ome_e=16*1.8d+03*ome_i  ! Electron  Gyrofrequency

      rk_i(i)=ome_i/rnu_in(i)
      rk_e(i)=ome_e/rnu_en(i)
      al=1./(rk_i(i)*(rk_e(i)-rk_i(i)))
      si(i)=al*rk_e(i)/(1.-al)
      si(i)=1./rk_i(i)


!...............................................

         rk_i1(i)=1.+rk_i(i)**2.
         rk_e1(i)=1.+rk_e(i)**2.

         phi(j)=phi_min+(j-1)*dphi

      sigma=20.
      dist_gauss=exp(-(r(i)-r(40))**2./sigma**2)



      wf_m(i)=70.*dist_gauss;wq_m(i)=70.*dist_gauss
      wpm(i,j,k)=0;wfm(i,j,k)=0*wf_m(i);wqm(i,j,k)=0*wq_m(i)
      wp(i,j,k)=0;wf(i,j,k)=0*wf_m(i);wq(i,j,k)=0*wq_m(i)
      wpo(i,j,k)=0;wfo(i,j,k)=0*wf_m(i);wqo(i,j,k)=0*wq_m(i)

      rhoat_g(i,j,k)=rhoat_o(i,j,k);temp_g(i,j,k)=temp_o(i,j,k)

      den_o(i,j,k)=den_i(i,j,k);pot(i,j,k)=0.
      up(i,j,k)=0;uf(i,j,k)=0;uq(i,j,k)=0

      mag_pm(i,j,k)=0;mag_fm(i,j,k)=0;mag_qm(i,j,k)=0
      mag_po(i,j,k)=0;mag_fo(i,j,k)=0;mag_qo(i,j,k)=0
      mag_p(i,j,k)=0;mag_f(i,j,k)=0;mag_q(i,j,k)=0
      den_max=MAX(den_max,ABS(temp_o(i,j,k)))

      sigma=20.
      if (r(i).le.r(45))sigma=10.
      dist_gauss=exp(-(r(i)-r(45))**2./sigma**2)
```

```fortran
          den_o_na(i,j,k)=4.d+09*dist_gauss
        enddo
        enddo
        enddo



        gr_max=0;ig_max=1;phi_max=0.5d+00
        dt=0.1;i_t=1;t=0.
        up_max=0;temp_max=0

          do while(wp_max.le.1.5d+02.and.wf_max.le.1.5d+02)
          wp_max=0;wf_max=0;wq_max=0;wpo_max=0
```

c . . . .

```fortran
          if(t.eq.0)theta_o=theta(31)
          vel_th=0*0.02*dtheta
          theta_o=theta_o-vel_th*dt

          do k=1,ntheta
          do j=1,nophi

          wl=10.*dtheta;k1=2.*pi/wl;k2=k1
          w_o=2.*pi/(5.*60)
          s_o=cos(k1*phi(j)+0*k2*theta(k)-0*w_o*t)
          t_o=300.;sigma=150.
          s_t=cos(0*w_o*t)*exp(-((t-t_o)/sigma)**2.)
          sigma=5.*dtheta;theta_o=theta(31)
          s_theta=exp(-((theta(k)-theta_o)/sigma)**2.)
          sigma=5.*dphi;phi_o=phi(31)
          s_phi=exp(-((phi(j)-phi_o)/sigma)**2.)
          wpo(1,j,k)=1.d-03*s_o*s_theta*s_phi*s_t
          wpo_max=max(wpo_max,abs(wpo(1,j,k)))
          enddo
          enddo
```

118

```fortran
          print *, "Source amplitude= ",wpo_max,t

c......Estimation of pressure and viscosity at each time....

          do k=1,ntheta
          do i=1,nor
          do j=1,nophi
          if(i_t.eq.1)then
              !temp_o(i,j,k)=500;
              bm_p(i)=20*1.67d-27
              rhoat_oo(i,j,k)=rhoat_o(i,j,k)
          endif
              a=4.d+00
              visc_mu=a*3.563d-07*(temp_o(i,j,k))**(0.71)!Viscosity
              visc_nu(i,j,k)=visc_mu/rhoat_o(i,j,k)
              visc_max=max(visc_max,abs(visc_nu(i,j,k)*1.d-00))
              r_g=200.*(1.+sqrt(r(i)-r_ea+1000.)/50.)
              press(i,j,k)=r_g*rhoat_o(i,j,k)*temp_o(i,j,k)  !Atmospheric P:
              c_s(i,j,k)=sqrt(1.4*press(i,j,k)/rhoat_o(i,j,k))
          enddo
          enddo
          enddo

c          goto 200
c..........Simulation for AGWs begin......
                  w=1.0
          do ig=1,11
                  error_m=0
                  d2_wmax=0
          do k=1,ntheta
                  kp1=k+1
                  km1=k-1

            if(k.eq.1)km1=ntheta-1!1+ntheta/2-1!
                if(k.eq.ntheta)kp1=2!ntheta-ntheta/2+1!2
          a_q=1
```

```fortran
          ! if (k.eq.ntheta.or.k.eq.1)a_q=2
          do   j=1,nophi
                  jp1=j+1
                  jm1=j-1
              if (j.eq.nophi)jp1=2!nophi-int(wl/dphi)+1!2
                  if (j.eq.1)jm1=nophi-1!1+int(wl/dphi)-1!nophi-1
          a_f=1
          ! if (j.eq.nophi.or.j.eq.1)a_f=2
                  do   i=1,nor
                  ip1=i+1
                  im1=i-1
          if (i.eq.1)im1=i
          if (i.eq.nor)ip1=i

                  dr_k=1.*5.d-01*p_hp(i,k)
                  dphi_k=a_f*5.d-01/(dphi*hphi(i,k))
                  dq_k=a_q*5.d-01*q_hq(i,k)


c.......First and second order derivatives of density....

                  dlrho_p(i,j,k)=1.*dr_k*(rhoat_o(ip1,j,k)-rhoat_o(im1,j,k)
     &             /(rhoat_o(ip1,j,k)+rhoat_o(im1,j,k))
                  dlrho_f(i,j,k)=1.*dphi_k*(rhoat_o(i,jp1,k)-rhoat_o(i,jm1,
     &             /(rhoat_o(i,jp1,k)+rhoat_o(i,jm1,k))
                  dlrho_q(i,j,k)=1.*dq_k*(rhoat_o(i,j,kp1)-rhoat_o(i,j,km1)
     &             /(rhoat_o(i,j,kp1)+rhoat_o(i,j,km1))


c.........Derivative of wind and pressure force

                  d_wp=dr_k*(wp(ip1,j,k)-wp(im1,j,k))
                  d_wf=dphi_k*(wf(i,jp1,k)-wf(i,jm1,k))
                  d_wq=dq_k*(wq(i,j,kp1)-wq(i,j,km1))

                  div_w(i,j,k)=d_wp+d_wf+d_wq
                  div_w_p(i,j,k)=d_wp;div_w_f(i,j,k)=d_wf;div_w_q(i,j,k)=d_
```

```fortran
                  d_pr_p=dr_k*(press(ip1,j,k)-press(im1,j,k))
                  d_pr_f=f_gw*dphi_k*(press(i,jp1,k)-press(i,jm1,k))
                  d_pr_q=f_gw*dq_k*(press(i,j,kp1)-press(i,j,km1))

                  alph_4(i,j,k)=wp(i,j,k)*d_pr_p
     &                  +(wf(i,j,k)+wf_m(i))*d_pr_f
     &                  +(wq(i,j,k)+wq_m(i))*d_pr_q


         enddo
         enddo
         enddo

         do k=1,ntheta
                  kp1=k+1
                  km1=k-1
           if(k.eq.1)km1=ntheta-1!1+ntheta/2-1!
               if(k.eq.ntheta)kp1=2!ntheta-ntheta/2+1!
         a_q=1
         !if(k.eq.ntheta.or.k.eq.1)a_q=2
         do j=1,nophi
                  jp1=j+1
                  jm1=j-1
               if(j.eq.nophi)jp1=2!nophi-int(wl/dphi)+1
                  if(j.eq.1)jm1=nophi-1!1+int(wl/dphi)-1!nophi-1
         a_f=1
         !if(j.eq.nophi.or.j.eq.1)a_f=2

         do i=1,nor
                  ip1=i+1
                  im1=i-1
                  if(i.eq.1)im1=i
                  if(i.eq.nor)ip1=i


                  dr_k=5.d-01*p_hp(i,k)
                  dphi_k=a_f*5.d-01/(dphi*hphi(i,k))
```

```fortran
                    dq_k=a_q*5.d-01*q_hq(i,k)



                    gr_div_wp=dr_k*(div_w_p(ip1,j,k)-div_w_p(im1,j,k))
                    gr_div_wf=dphi_k*(div_w_f(i,jp1,k)-div_w_f(i,jm1,k))
                    gr_div_wq=dq_k*(div_w_q(i,j,kp1)-div_w_q(i,j,km1))

                    gr_div_wp=dr_k*(div_w(ip1,j,k)-div_w(im1,j,k))
                    gr_div_wf=dphi_k*(div_w(i,jp1,k)-div_w(i,jm1,k))
                    gr_div_wq=dq_k*(div_w(i,j,kp1)-div_w(i,j,km1))

              gr_al4p=dr_k*(alph_4(ip1,j,k)-alph_4(im1,j,k))
                    gr_al4f=dphi_k*(alph_4(i,jp1,k)-alph_4(i,jm1,k))
                    gr_al4q=dq_k*(alph_4(i,j,kp1)-alph_4(i,j,km1))

                    d_pr_p=dr_k*(press(ip1,j,k)-press(im1,j,k))
                    d_pr_f=f_gw*dphi_k*(press(i,jp1,k)-press(i,jm1,k))
                    d_pr_q=f_gw*dq_k*(press(i,j,kp1)-press(i,j,km1))

                    alph1_p=-d_pr_p/rhoat_o(i,j,k)
                    alph1_f=-d_pr_f/rhoat_o(i,j,k)
                    alph1_q=-d_pr_q/rhoat_o(i,j,k)

                    alph2=gamma/rhoat_o(i,j,k)
                    alph3=wp(i,j,k)*dlrho_p(i,j,k)
     &              +(wf(i,j,k)+wf_m(i))*dlrho_f(i,j,k)
     &              +(wq(i,j,k)+wq_m(i))*dlrho_q(i,j,k)

              dr_k2=2.*dr_k**2.
              d2pr_p=dr_k2*(press(ip1,j,k)-2.*press(i,j,k)+press(im1,j,k))
              w_br_2(i,j,k)=(d_pr_p*dlrho_p(i,j,k)-d2pr_p)/rhoat_o(i,j,k)


c..........First term of AGW wave equation related to the Acoustic wave..

                    wp1=(gamma*press(i,j,k)/rhoat_o(i,j,k))*gr_div_wp
                    wf1=(gamma*press(i,j,k)/rhoat_o(i,j,k))*gr_div_wf
                    wq1=(gamma*press(i,j,k)/rhoat_o(i,j,k))*gr_div_wq
```

c . . . . Second term of AGW wave equation related to the Acoustic wave.

```
wp2=(alph1_p+alph2*d_pr_p)*div_w_p(i,j,k)
wf2=(alph1_f+alph2*d_pr_f)*div_w_f(i,j,k)
wq2=(alph1_q+alph2*d_pr_q)*div_w_q(i,j,k)
```

c . . . . Third term of AGW wave equation related to the Gravity wave...

```
wp3=(1./rhoat_o(i,j,k))*gr_al4p
wf3=(1./rhoat_o(i,j,k))*gr_al4f
wq3=(1./rhoat_o(i,j,k))*gr_al4q
```

c . . . . Fourth term of AGW wave equation related to the Gravity wave...

```
wp4=alph1_p*alph3
wf4=alph1_f*alph3
wq4=alph1_q*alph3

wp0=2.*wpo(i,j,k)-wpm(i,j,k)
wf0=2.*wfo(i,j,k)-wfm(i,j,k)
wq0=2.*wqo(i,j,k)-wqm(i,j,k)
```

! . . . .

```
visc_ki=visc_nu(i,j,k)
alph3=dlrho_p(i,j,k)*wp_i_max(i)
d2w_p=dr_k**2.*(wp(ip1,j,k)+wp(im1,j,k))
d2w_f=dphi_k**2.*(wf(i,jp1,k)+wf(i,jm1,k))
d2w_q=dq_k**2.*(wq(i,j,kp1)+wq(i,j,km1))
d2w_f=dr_k**2.*(wf(ip1,j,k)+wf(im1,j,k))
d2w_q=dr_k**2.*(wq(ip1,j,k)+wq(im1,j,k))

visc_rt_p=(visc_ki*(0*div_w(i,j,k)+alph3))
visc_rt_f=(visc_ki*(0*div_w(i,j,k)+alph3))
visc_rt_q=(visc_ki*(0*div_w(i,j,k)+alph3))
```

123

```
visc_rt_max=(visc_max*alph3)
visc_rt_p=visc_rt_max;
visc_rt_f=visc_rt_max;
visc_rt_q=visc_rt_max;

wp8=visc_rt_p*d2w_p
wf8=visc_rt_f*d2w_f
wq8=visc_rt_q*d2w_q
```

!................................

```
d2wo_p=dr_k**2.*(wpo(ip1,j,k)-2*wpo(i,j,k)+wpo(im1,j,k))
d2wo_f=dphi_k**2.*(wfo(i,jp1,k)-2*wfo(i,j,k)+wfo(i,jm1,k))
d2wo_q=dq_k**2.*(wqo(i,j,kp1)-2*wqo(i,j,k)+wqo(i,j,km1))
d2w_p=dr_k**2.*(wp(ip1,j,k)+wp(im1,j,k))
d2w_f=dphi_k**2.*(wf(i,jp1,k)+wf(i,jm1,k))
d2w_q=dq_k**2.*(wq(i,j,kp1)+wq(i,j,km1))

d2wo_f=dr_k**2.*(wfo(ip1,j,k)-2*wfo(i,j,k)+wfo(im1,j,k))
d2wo_q=dr_k**2.*(wqo(ip1,j,k)-2*wqo(i,j,k)+wqo(im1,j,k))
d2w_f=dr_k**2.*(wf(ip1,j,k)+wf(im1,j,k))
d2w_q=dr_k**2.*(wq(ip1,j,k)+wq(im1,j,k))

dwp_t=(d2w_p-d2wo_p)/dt
dwf_t=(d2w_f-d2wo_f)/dt
dwq_t=(d2w_q-d2wo_q)/dt

visc_wt=visc_nu(i,j,k)/dt
wp9=visc_nu(i,j,k)*dwp_t
wf9=visc_nu(i,j,k)*dwf_t
wq9=visc_nu(i,j,k)*dwq_t
```

!.....................Nonlinear saturation..............

```
dwp_p=wp(i,j,k)*dr_k*(wp(ip1,j,k)-wp(im1,j,k))
dwop_p=wpo(i,j,k)*dr_k*(wpo(ip1,j,k)-wpo(im1,j,k))
wp_nl=(dwp_p-dwop_p)/dt
```

```
      dwf_f=wf(i,j,k)*dphi_k*(wf(i,jp1,k)-wf(i,jm1,k))
      dwof_f=wfo(i,j,k)*dphi_k*(wfo(i,jp1,k)-wfo(i,jm1,k))
      wf_nl=(dwf_f-dwof_f)/dt
      dwq_q=wq(i,j,k)*dq_k*(wq(i,j,kp1)-wq(i,j,km1))
      dwoq_q=wqo(i,j,k)*dq_k*(wqo(i,j,kp1)-wqo(i,j,km1))
      wq_nl=(dwq_q-dwoq_q)/dt


      dw_t_f=(wp(i,jp1,k)-wp(i,jm1,k)-
   &       wpo(i,jp1,k)+wpo(i,jm1,k))*dphi_k/dt
      dw_t_q=(wp(i,j,kp1)-wp(i,j,km1)-
   &       wpo(i,j,kp1)+wpo(i,j,km1))*dq_k/dt
      wp_nl=wf_m(i)*dw_t_f+wq_m(i)*dw_t_q+wp_nl


      dw_t_f=(wf(i,jp1,k)-wf(i,jm1,k)-
   &       wfo(i,jp1,k)+wfo(i,jm1,k))*dphi_k/dt
      dw_t_q=(wf(i,j,kp1)-wf(i,j,km1)-
   &       wfo(i,j,kp1)+wfo(i,j,km1))*dq_k/dt
      wf_nl=wf_m(i)*dw_t_f+wq_m(i)*dw_t_q+wf_nl


      dw_t_f=(wq(i,jp1,k)-wq(i,jm1,k)-
   &       wqo(i,jp1,k)+wqo(i,jm1,k))*dphi_k/dt
      dw_t_q=(wq(i,j,kp1)-wq(i,j,km1)-
   &       wqo(i,j,kp1)+wqo(i,j,km1))*dq_k/dt
      wq_nl=wf_m(i)*dw_t_f+wq_m(i)*dw_t_q+wq_nl

!..............TOTAL COEFFICIENT..................

      d_space=dr_k**2.+dphi_k**2.+dq_k**2.
      coef_total=abs(visc_rt_p)+abs(visc_wt)
      wa_p=exp(-dt**2*(dr_k**2.)*coef_total*2.)
      coef_total=abs(visc_rt_f)+abs(visc_wt)
      wa_f=exp(-dt**2*(dr_k**2.)*coef_total*2.)
      coef_total=abs(visc_rt_q)+abs(visc_wt)
      wa_q=exp(-dt**2*(dr_k**2.)*coef_total*2.)


!.....................CI.........................
```

```fortran
dtemp_y=(temp_o(ip1,j,k)−temp_o(im1,j,k))*dr_k
temp_av=1.*(temp_o(ip1,j,k)+temp_o(im1,j,k))/2.

eta=rhoat_oo(i,j,k)/rhoat_o(i,j,k)

ga_ac=9.8/(283.*temp_av)
ga_e=dtemp_y/temp_av  !a2
a1=(eta−1.)*ga_ac
a2=(1./temp_av)*dtemp_y


f_br2=eta*9.8*(a1+a2)
wp3_ci=−f_br2*wp(i,j,k)

!................CI in horizontal....................
dtemp_f=(temp_o(i,jp1,k)−temp_o(i,jm1,k))*dphi_k
temp_av=1.*(temp_o(i,jp1,k)+temp_o(i,jm1,k))/2.

ga_ac=alph1_f/(283.*temp_av)
ga_e=dtemp_f/temp_av  !a2
a1=(eta−1.)*ga_ac
a2=(1./temp_av)*dtemp_f

f_br2=eta*alph1_f*(a1+a2)
wf3_ci=−f_br2*wf(i,j,k)

dtemp_q=(temp_o(i,j,kp1)−temp_o(i,j,km1))*dq_k
temp_av=1.*(temp_o(i,j,kp1)+temp_o(i,j,km1))/2.

ga_ac=alph1_q/(283.*temp_av)
ga_e=dtemp_q/temp_av  !a2
a1=(eta−1.)*ga_ac
a2=(1./temp_av)*dtemp_q

f_br2=eta*alph1_q*(a1+a2)
wq3_ci=−f_br2*wq(i,j,k)
```

```fortran
      w_ci_max=max(w_ci_max,max(wf3_ci,wq3_ci))
      wp_ci_max=max(wp_ci_max,wp3_ci)
!.................................................
      wp_tot=(wp1+wp2+wp3+0*wp3_ci+wp4+wp8+wp9-wp_nl/1.)
      wf_tot=(wf1+wf2+wf3+0*wf3_ci+wf4+wf8+wf9-wf_nl/1.)
      wq_tot=(wq1+wq2+wq3+0*wq3_ci+wq4+wq8+wq9-wq_nl/1.)


!...................................................

      if(ig.eq.1)then
      wp_ex(i,j,k)=wp_tot;wf_ex(i,j,k)=wf_tot;wq_ex(i,j,k)=wq_tot;
      endif

c............Solving the wave equation................

         wp_g=wa_p*(wp0+dt**2.*(wp_tot+0*wp_ex(i,j,k))/1.)
         wf_g=wa_f*(wf0+dt**2.*(wf_tot+0*wf_ex(i,j,k))/1.)
         wq_g=wa_q*(wq0+dt**2.*(wq_tot+0*wq_ex(i,j,k))/1.)


         error=abs(wp_g-wp(i,j,k))
       error_m=max(error_m,error)


         wps(i,j,k)=(1.-w)*wp(i,j,k)+w*wp_g
         wfs(i,j,k)=(1.-w)*wf(i,j,k)+w*wf_g
         wqs(i,j,k)=(1.-w)*wq(i,j,k)+w*wq_g


      enddo
      enddo
      enddo

         do k=1,ntheta
         do i=1,nor
         do j=1,nophi
         wp(i,j,k)=wps(i,j,k)
```

```fortran
                    wf(i,j,k)=wfs(i,j,k)
                    wq(i,j,k)=wqs(i,j,k)

c                    if(i_t.gt.1)then
c                   wp(1,j,k)=wpo(1,j,k)
c                   wf(1,j,k)=wfo(1,j,k)
c                   wq(1,j,k)=wqo(1,j,k)
c                    endif
                      if(abs(wp(i,j,k)).ge.wp_max)then
                  ig_max=i;jg_max=j;kg_max=k
                  endif
                  wp_max=max(wp_max,abs(wp(i,j,k)))
                     wf_max=max(wf_max,abs(wf(i,j,k)))
                       wq_max=max(wq_max,abs(wq(i,j,k)))

                  enddo
                  enddo
                  enddo

                          if(error_m.ge.1.d-11)then
                       w=w-0.1
                          if(w.le.1)w=1.
                       else
                          goto 35
                       endif
            enddo
35               continue

                  do i=1,nor
                  wp_i_max(i)=0;wf_i_max(i)=0
                  do k=1,ntheta
                  do j=1,nophi
                  wp_i_max(i)=max(wp_i_max(i),abs(wp(i,j,k)))
                  wf_i_max(i)=max(wf_i_max(i),abs(wf(i,j,k)))
                  wpm(i,j,k)=wpo(i,j,k)
                  wpo(i,j,k)=wp(i,j,k)
                  wfm(i,j,k)=wfo(i,j,k)
```

128

```fortran
      wfo(i,j,k)=wf(i,j,k)
      wqm(i,j,k)=wqo(i,j,k)
      wqo(i,j,k)=wq(i,j,k)

      rhoat_g(i,j,k)=rhoat_o(i,j,k)
      enddo
      enddo
      enddo
```

! . . . . NEUTRAL_DENSITY/TEMPERATURE . . . .

```fortran
      do ig=1,11

      do k=1,ntheta
      do j=1,nophi
      do i=1,nor
      flux_p(i,j,k)=rhoat_g(i,j,k)*wp(i,j,k)
      flux_f(i,j,k)=rhoat_g(i,j,k)*(wf(i,j,k)+wf_m(i))
      flux_q(i,j,k)=rhoat_g(i,j,k)*(wq(i,j,k)+wq_m(i))
      enddo
      enddo
      enddo

      do k=1,ntheta
      kp1=k+1
      km1=k-1
      if(k.eq.1)km1=ntheta-1!1+ntheta/2-1!
      if(k.eq.ntheta)kp1=2!ntheta-ntheta/2+1!2
      a_q=1.
      !if(k.eq.1.or.k.eq.ntheta)a_q=2.
      do j=1,nophi
      jm1=j-1
      jp1=j+1
      if(j.eq.nophi)jp1=2!nophi-int(wl/dphi)+1
            if(j.eq.1)jm1=nophi-1!1+int(wl/dphi)-1
      a_f=1
      !if(j.eq.nophi.or.j.eq.1)a_f=2
```

```fortran
      do i=1,nor
      ip1=i+1
      im1=i-1
      if(i.eq.nor)ip1=i
      if(i.eq.1)im1=i

      dr_k=5.d-01*p_hp(i,k)!/(dp(i)*hp(i,k))
      dphi_k=f_gw*a_f*5.d-01/(dphi*hphi(i,k))
      dq_k=f_gw*a_q*5.d-01*q_hq(i,k)!/(dq(i)*hq(i,k))

      dt_f=dphi_k*(temp_g(i,jp1,k)-temp_g(i,jm1,k))
      dt_p=dr_k*(temp_g(ip1,j,k)-temp_g(im1,j,k))
      dt_q=dq_k*(temp_g(i,j,kp1)-temp_g(i,j,km1))


      dfl_f=dphi_k*(flux_f(i,jp1,k)-flux_f(i,jm1,k))
      dfl_p=dr_k*(flux_p(ip1,j,k)-flux_p(im1,j,k))
      dfl_q=dq_k*(flux_q(i,j,kp1)-flux_q(i,j,km1))

      rhoat_t(i,j,k)=rhoat_o(i,j,k)-dt*(dfl_f+dfl_p+dfl_q)

      temp_t(i,j,k)=temp_o(i,j,k)-dt*(
     &                   wp(i,j,k)*dt_p
     &       +(wf_m(i)+wf(i,j,k))*dt_f
     &       +(wq_m(i)+wq(i,j,k))*dt_q
     &           +(gamma-1)*temp_g(i,j,k)*div_w(i,j,k))

      enddo
      enddo
      enddo


      do k=1,ntheta
      do i=1,nor
      do j=1,nophi
      rhoat_g(i,j,k)=rhoat_t(i,j,k)
```

```
            temp_g(i,j,k)=temp_t(i,j,k)
            temp_max=max(temp_max,abs(temp_o(i,j,k)))
            enddo
            enddo
            enddo


      enddo    !ITER LOOP


            do k=1,ntheta
            do j=1,nophi
            do i=1,nor
            rhoat_o(i,j,k)=rhoat_t(i,j,k)
            temp_o(i,j,k)=temp_t(i,j,k)
            enddo
            enddo
            enddo


! . . . . . . . . . . . . . . . . . . . . . . .OH AIRGLOW . . . . . . . . . . . . . . . . . . . . . . . . . . . . . . .
            oh_ag_max=0

            do k=1,ntheta
            do j=1,nophi
            do i=1,nor
            rhoat_g(i,j,k)=rho_o3o(i,j,k)
            enddo
            enddo
            enddo

            do ig=1,1

            do k=1,ntheta
            do j=1,nophi
            do i=1,nor

            flux_p(i,j,k)=rho_o3o(i,j,k)*wp(i,j,k)
            flux_f(i,j,k)=rho_o3o(i,j,k)*(wf(i,j,k)+0*wf_m(i))
            flux_q(i,j,k)=rho_o3o(i,j,k)*(wq(i,j,k)+0*wq_m(i))
```

131

```
enddo
enddo
enddo

do k=1,ntheta
kp1=k+1
km1=k-1
if(k.eq.1)km1=k
if(k.eq.ntheta)kp1=k
do j=1,nophi
jm1=j-1
jp1=j+1
if(j.eq.nophi)jp1=j!2
if(j.eq.1)jm1=j!nophi-1
do i=1,nor
ip1=i+1
im1=i-1
if(i.eq.nor)ip1=i
if(i.eq.1)im1=i

dr_k=5.d-01*p_hp(i,k)!/(dp(i)*hp(i,k))
dphi_k=f_gw*5.d-01/(dphi*hphi(i,k))
dq_k=f_gw*5.d-01*q_hq(i,k)!/(dq(i)*hq(i,k))



dfl_f=dphi_k*(flux_f(i,jp1,k)-flux_f(i,jm1,k))
dfl_p=dr_k*(flux_p(ip1,j,k)-flux_p(im1,j,k))
dfl_q=dq_k*(flux_q(i,j,kp1)-flux_q(i,j,km1))



den_o2=2.d+19;den_ox=5.d+16;den_h=1.d+14
den_ox=3.8d+17*exp(-(r(i)-r_ea-100.)**2./9.**2.)
den_h=1.d+14*exp(-(r(i)-r_ea-85.)**2./20.**2.)
den_o2=rhoat_o(i,j,k)*280/b_c
ch_1_o2=6.d-45*den_o2**2.*(200./300.)**(2.5)
ch_2_h=1.4d-16*exp(-470./300.)*den_h
ch_1_o2=24.d-07*(200./300.)**(2.5)
```

```
      ch_2_h=1.4d-02*exp(-470./300.)
      ch=-ch_2_h*rho_o3o(i,j,k)+ch_1_o2*den_ox
      dfl=dfl_f+dfl_p+dfl_q
      rho_o3(i,j,k)=rho_o3o(i,j,k)+dt*(ch-dfl)
      a_l=1./(260.+2.d-17*den_o2)
      a_l=1./(260.+4.d+02)
      f_8=0.27
      oh_ag(i,j,k)=a_l*f_8*ch_2_h*rho_o3(i,j,k)
      oh_ag_max=max(abs(oh_ag(i,j,k)),oh_ag_max)


      dfl_p=dr_k*(den_o_na(ip1,j,k)*wp(ip1,j,k)-
&                 den_o_na(im1,j,k)*wp(im1,j,k))
      dfl_f=dphi_k*(den_o_na(i,jp1,k)*wf(i,jp1,k)-
&                 den_o_na(i,jm1,k)*wf(i,jm1,k))
      dfl_q=dq_k*(den_o_na(i,j,kp1)*wq(i,j,kp1)-
&                 den_o_na(i,j,km1)*wq(i,j,km1))

      dfl=dfl_p+dfl_f+dfl_q
      den_na(i,j,k)=den_o_na(i,j,k)-dt*(dfl)
      enddo
      enddo
      enddo
      print *, ch_1_o2,ch_2_h,ch

      do k=1,ntheta
      do i=1,nor
      do j=1,nophi
      rhoat_g(i,j,k)=rho_o3(i,j,k)
      enddo
      enddo
      enddo

      enddo          !ITER LOOP

      do k=1,ntheta
      do j=1,nophi
```

```fortran
        do i=1,nor
        rho_o3o(i,j,k)=rho_o3(i,j,k)
        den_o_na(i,j,k)=den_na(i,j,k)
        enddo
        enddo
        enddo


!...........................................................................
        !goto 301
!...........................END............................................
!<<<<<<<<<<<<<<<<<<<<<<<<<<<<<<<<<<<<<<>>>>>>>>>>>>>>>>>>>>>>>>>>>>>>>>>>>>>>


301     continue

                r_t=mod(i_t+19,20)
                if (r_t.eq.0)then
                do k=1,ntheta
                do j=1,nophi
                write(75,91)(wp(i,j,k),i=1,81,2)
                write(76,91)(wf(i,j,k),i=1,81,2)
                write(77,91)(wq(i,j,k),i=1,81,2)
                write(78,91)(c_s(i,j,k),i=1,81,2)
                write(79,91)(temp_o(i,j,k),i=1,81,2)
                write(80,91)(w_br_2(i,j,k),i=1,81,2)
                write(81,91)(oh_ag(i,j,k),i=1,81,2)
                write(82,91)(den_na(i,j,k),i=1,81,2)
                enddo
                enddo

                endif

                print *, "Time",t,", Wp=",wp_max,", WF=",wf_max,
     &              ", WQ=",wq_max
            print *, "Altitude of Maximum amplitude=",r(ig_max)-r_ea
             print *, ig_max, jg_max, kg_max
```

134

```fortran
              print *, "OH AIRGLOW", oh_ag_max

         write(83,*)t,wp_max,wf_max,wq_max

              dt=2.
              t=t+dt
              i_t=i_t+1

         ENDDO

200      continue

              do k=1,ntheta
              do j=1,nophi
              write(75,91)(wp(i,j,k),i=1,81,2)
              write(76,91)(wf(i,j,k),i=1,81,2)
              write(77,91)(wq(i,j,k),i=1,81,2)
              write(78,91)(c_s(i,j,k),i=1,81,2)
              write(79,91)(temp_o(i,j,k),i=1,81,2)
              write(80,91)(w_br_2(i,j,k),i=1,81,2)
              write(81,91)(oh_ag(i,j,k),i=1,81,2)
              write(82,91)(den_na(i,j,k),i=1,81,2)
              enddo
              enddo

91       FORMAT (301(1x,e14.4))
          end
```

PUBLICAÇÕES TÉCNICO-CIENTÍFICAS EDITADAS PELO INPE

Teses e Dissertações (TDI)

Teses e Dissertações apresentadas nos Cursos de Pós-Graduação do INPE.

Notas Técnico-Científicas (NTC)

Incluem resultados preliminares de pesquisa, descrição de equipamentos, descrição e ou documentação de programas de computador, descrição de sistemas e experimentos, apresentação de testes, dados, atlas, e documentação de projetos de engenharia.

Propostas e Relatórios de Projetos (PRP)

São propostas de projetos técnico-científicos e relatórios de acompanhamento de projetos, atividades e convênios.

Publicações Seriadas

São os seriados técnico-científicos: boletins, periódicos, anuários e anais de eventos (simpósios e congressos). Constam destas publicações o Internacional Standard Serial Number (ISSN), que é um código único e definitivo para identificação de títulos de seriados.

Pré-publicações (PRE)

Todos os artigos publicados em periódicos, anais e como capítulos de livros.

Manuais Técnicos (MAN)

São publicações de caráter técnico que incluem normas, procedimentos, instruções e orientações.

Relatórios de Pesquisa (RPQ)

Reportam resultados ou progressos de pesquisas tanto de natureza técnica quanto científica, cujo nível seja compatível com o de uma publicação em periódico nacional ou internacional.

Publicações Didáticas (PUD)

Incluem apostilas, notas de aula e manuais didáticos.

Programas de Computador (PDC)

São a seqüência de instruções ou códigos, expressos em uma linguagem de programação compilada ou interpretada, a ser executada por um computador para alcançar um determinado objetivo. Aceitam-se tanto programas fonte quanto os executáveis.